Spring 2011

Application of raman spectroscopy in pharmaceuticals

Anna Zarow
New Jersey Institute of Technology

ABSTRACT

APPLICATION OF RAMAN SPECTROSCOPY IN PHARMACEUTICALS

by
Anna Żarów

Experimental research on the use of Raman spectroscopy as an in- and on-line sensing tool and a complementary characterization technique for pharmaceutical applications is presented in this thesis. In the first chapter following a broad overview, the use of Raman spectroscopy, together with x-ray powder diffraction, scanning electron microscopy (SEM) and differential scanning calorimetry, for multilevel characterization of cryomilled powders, and the melt-grown amorphous phase of griseofulvin, a model active pharmaceutical ingredient (API), is presented and discussed in detail. A key feature was the observation of a broad inelastic background superimposed on the Raman spectra of cryomilled powders, which is attributed to lattice disorder and Mie scattering generated by mechanical processing and sub-micron particle interfaces. In the following chapter, polymorphs of another model API, acetaminophen (APAP), were studied by Raman spectroscopy with supporting information obtained from x-ray diffraction, SEM images and intrinsic dissolution profiles. An important result was the stabilization and characterization of the metastable type II orthorhombic phase of APAP which is highly desired for its unique tabletting properties which are important for pharmaceutical manufacturing. Stabilization of metastable type II APAP was achieved by micronizing or nanocoating stable monoclinic crystallites of type I APAP. In addition, as an Appendix to the thesis, micro-Raman spectroscopy of single crystal APAP as a function of crystal orientation and of temperature was measured to provide an understanding of the lattice properties of APAP for input into models to predict its behavior under mechanical

milling conditions widely used in pharmaceutical processing. Molecular behavior obtained from the above studies guided simulated in-line and off-line characterization of griseofulvin as thin gel films made from micronized powders and nanosuspensions. By employing complementary near infrared and Raman imaging for newly developed films, it was possible to extract valuable information on the spatial distribution and crystallinity of the embedded particles in a polymeric matrix at different scales of scrutiny. Chemometrics processing of spectroscopic data for films and nanosuspensions allowed for qualitative and quantitative particle size determinations of the API's in the films and nanosuspensions. In the final chapter a photonic crystal substrate for surface enhanced Raman spectroscopic (SERS) sensing was employed to detect and study griseofulvin and APAP down to 10^{-8} M levels with enhancement factors approaching 10^{9}. Detection sensitivities of the aromatic griseofulvin and APAP molecules were also compared with those of less aromatic and non-aromatic energetic molecules in order to understand the Raman enhancement process.

APPLICATION OF RAMAN SPECTROSCOPY IN PHARMACEUTICALS

by
Anna Żarów

A Dissertation
Submitted to the Faculty of
New Jersey Institute of Technology
in Partial Fulfillment of the Requirements for the Degree of
Doctor of Philosophy in Chemistry

Department of Chemistry and Environmental Science

May 2011

.

APPROVAL PAGE

APPLICATION OF RAMAN SPECTROSCOPY IN PHARMACEUTICALS

Anna Żarów

Dr. Zafar Iqbal, Dissertation Co-Advisor — Date
Research Professor of Chemistry and Environmental Science, NJIT

Dr. Tamara Gund, Dissertation Co-Advisor — Date
Professor of Chemistry and Environmental Science, NJIT

Dr. Shirlynn Chen, Committee Member — Date
Senior Research Fellow, Boehringer Ingelheim Pharmaceuticals

Dr. Rajesh N. Dave, Committee Member — Date
Distinguished Professor of Chemical Engineering, NJIT

Dr. Somenath Mitra, Committee Member — Date
Chair of Chemistry and Environmental Science, NJIT

Dr. Carol A. Venanzi, Committee Member — Date
Distinguished Professor of Chemistry and Environmental Science, NJIT

BIOGRAPHICAL SKETCH

Author: Anna Żarów

Degree: Doctor of Philosophy

Date: May 2011

Undergraduate and Graduate Education:

- Doctor of Philosophy in Chemistry,
  New Jersey Institute of Technology, Newark, NJ, 2011

- Bachelor of Art in Chemistry,
  Kean University, Union, NJ, 2005

- Associate in Science in Chemistry,
  Middlesex Count College, Edison, NJ, 2003

Major: Chemistry and Environmental Science

Presentations and Publications:

J. Jerez, A. Zarow, B. Zhou, R. Pinal, Z. Iqbal, R. Romanach, "Complementary Near-Infrared and Raman chemical imaging of pharmaceutical gel strip films", Journal of Pharmaceutical Sciences, under review.

A. Żarow, B. Zhou, X. Wang, R. Pinal, Z. Iqbal, "Spectroscopic and X-ray diffraction study of structural disorder in cryomilled and amorphous Griseofulvin", Applied Spectroscopy 65, pp.135-143, 2011.

S. Wang, F. Yang, M. Silva, A. Zarow, Y. Wang, Z. Iqbal, "Membrane-less and mediator-free enzymatic biofuel cells using carbon nanotube/porous silicon electrodes", Electrochemistry Communications, 11, pp.34-37, 2009.

A. Zarow, Y. Shin, "Cyanine Dyes: Fine Structures in Their Absorption Spectra", American Journal of Undergraduate Research, 8, pp.7-13, 2009.

A. Zarow, W. Wagner, E. Lee, F. Adar, B. Zhou, R. Pinal, Z. Iqbal, "Raman Spectroscopy of Defected Griseofulvin in Powders and Films", Proceedings of

Material Research Society Conference, Boston, MA, 1140-HH05, pp.34-39, December 2009.

A. Zarow, W. Wagner, E. Lee, F. Adar, B. Zhou, R. Pinal and Z. Iqbal, “Raman Spectroscopy of Defected Griseofulvin in Powders and Films", Presented at Material Research Society Fall Meeting, Boston, MO, December 2008.

A. Zarow, Y. Shin, “Origin of Fine-structure in Absorption Spectra of Cyanine Dyes”, Presented at American Chemical Society Middle Atlantic Regional Meeting, New Brunswick, NJ, May 2005.

This Thesis Is Dedicated To My Beloved Husband:
You Are the Reason I Have Believed I Could Do This.
Now, I Believe That We Can Fly Together.
“To Wszystko Dzięki Tobie i Dla Ciebie”

Dla Moich Rodzicow:
Za Milosc, Otuchę i Nieustanną Motywację.

ACKNOWLEDGMENT

Foremost, I would like to express my sincere gratitude to my advisor, Prof. Zafar Iqbal for his continuous support of my Ph.D. study and research, for his patience, motivation, enthusiasm, and immense knowledge. His guidance helped me throughout the past five years I have spent working on this thesis. I could not have imagined having a better advisor and mentor for my Ph.D. study. My thanks also go to the members of my committee: Prof. Tamara Gund for agreeing to serve as a co-advisor, Dr. Shirlynn Chen, Prof. Rajesh N. Dave, Prof. Somenath Mitra, and Prof. Carol A. Venanzi for their insightful comments that improved the dissertation and content of this thesis.

I would like to thank to Prof. Frank J. Owens at Hunter College, City University of New York and Rajen Patel from ARDEC for free use of confocal Raman spectrometer.

Special thanks to Dr. Shirlynn Chen and group at Boehringer Ingelheim for providing and arranging intrinsic dissolution testing at their company's site.

I would like to thank to Jonathan Haulenbeek, Dr. John Wasylyk, Ming Huang, and Robert Wethman at Bristol-Myers Squibb for offering me the summer internship opportunity in their group and leading me working on exciting project.

I thank my fellow colleagues: Jinwen Liu, Anitha Patlolla, Dr. Thelma Manning, Dr. Amit Goyal, Jade Ye Ying, Richard Shao-chun Hsu, Ann Ma, Kunal Joshi for the good time I spent with them in the lab and the office and for their absolute help in many matters. My sincere thanks go to Dr. Chris Wang at CarboMet for her optimistic and upbeat personality and for enlightening me the first glance of research.

I would like to thank to Laila Jallo and Prof. Rajesh N. Dave at NJIT, Anagha Bhakay and Prof. Ecevit A. Bilgili at NJIT, Ezinwa Elele and Prof. Boris Khusid at NJIT,

Zhong He and Prof. Xianqin Wang at NJIT, Min Yang and Prof. Marino Xanthos at NJIT, Bo Zhou and Prof. Rodolfo Pinal at Purdue University, Yleana Colon, Jackeline Jerez, Jorge Ropero and Prof. Rodolfo Romanach at University of Puerto Rico, Dr. Rahul Haware and Prof. Ken Morris at University of Hawaii, for interesting and very productive collaborations on various research projects.

I would also like to thank to Dr. Fran Adar and Dr. Eunah Lee from Horiba Scientific Instruments for performing Raman imaging on multiple pharmaceutical samples and providing me with understanding of Raman instrumentation and chemometrics data analysis.

I would like to gratefully acknowledge the National Science Foundation Engineering Research Center for Structured Organic Particulate Systems (Grant no. EEC-0540855) for financial support throughout my Ph.D. study, US Army APDEC funding for acquisition of the fiber optic and grating Raman spectrometers , and New Jersey Institute of Technology for teaching assistantship. Without this financial support, I would not be able to achieve my goal.

Lastly, I would like to thank my husband, Rafał Łuczak for his understanding and unconditional love especially during the last few years. His support and encouragement was in the end what made this dissertation possible. To my parents, Teresa and Jarosław, for giving birth to me and motivating me throughout my study abroad.

TABLE OF CONTENTS

TABLE OF CONTENTS
(Continued)

TABLE OF CONTENTS
(Continued)

TABLE OF CONTENTS
(Continued)

LIST OF TABLES

LIST OF FIGURES

LIST OF FIGURES
(Continued)

Figure **Page**

LIST OF FIGURES
(Continued)

LIST OF FIGURES
(Continued)

Figure **Page**

LIST OF FIGURES
(Continued)

Figure **Page**

LIST OF FIGURES
(Continued)

Figure **Page**

CHAPTER 1

INTRODUCTION

1.1 General Background

The pharmaceutical industry, as one of the leading industries in the US, has experienced various challenges in the recent years. The number of drugs coming off patents and increase in generic drug availability is putting tremendous price pressure on domestic companies and their products. Quality issues are also at stake as the high number of recent recalls has severely damaged the reputation and reliability of the pharmaceutical industry. The need to increase the quality of the products due to numbers of recalls resulted in development of the Process Analytical Technology (PAT) initiative proposed by the US Food and Drug Administration (FDA). This initiative, which was first created in 2004 as an advisory for industry, will soon change into requirements to be adopted and followed.

Defined by the FDA, PAT is "a system for designing, analysis, and controlling manufacturing through timely measurements (i.e., during processing) of critical quality and performance attributes of raw and in-process materials and processes with the goal of ensuring final product quality" [1]. Real time process control is a critical aspect of the PAT initiative especially since nanotechnology becomes a part of novel and innovative pharmaceutical products. Process understanding and process control, robust design and built-in quality need to be integrated along the way at each stage of the manufacturing process to minimize widely used end-product or batch-to-batch testing. By implementing PAT, assessment of critical quality attributes of materials and products can be determined

early in the process development and allow for improvements and design of well-understood methodologies, ensuring high product quality throughout the continuous manufacturing process. Many analytical techniques are already used as in-process quality control tools, which includes a variety of physical techniques, such as diffraction, thermal, and spectroscopic methods applicable for macro-, micron- and sub-micron scale characterization. Used for solid state analysis, the analytical techniques provide understanding and knowledge on many complex phenomena at the molecular level (for example, polymorphism, disorder and defect-formation in molecular crystals, and chemical reactions), and at the batch-to-batch level during manufacturing (such as, granulation, drying and powder blending). To fully execute the FDA's PATs philosophy, these methodologies will require tools capable of operating at-line, on-line, and in-line stages and effectively utilize data processing management systems at all aspects of pharmaceutical development. Operating stages for the monitoring of manufacturing processes are presented in Figure 1.1 where the in-line analysis is shown to be performed at no physical contact between analytical system and the sample as the analyzer is located within the process. On-line analysis requires automated sampling and transfer to the automated analyzer. For at-line characterization, sampling is performed manually and transported to the analyzer located in the manufacturing area whereas in case of off-line analysis, the analyzer is located in the off-line laboratory.

Vibrational spectroscopy, for example near-infrared (NIR) and Raman spectroscopy, has gained wide acceptance as fast, highly informative and non-destructive complementary methods for this purpose. These technologies can be placed at many interfaces of pharmaceutical processes to provide rapid, non-invasive real-time data.

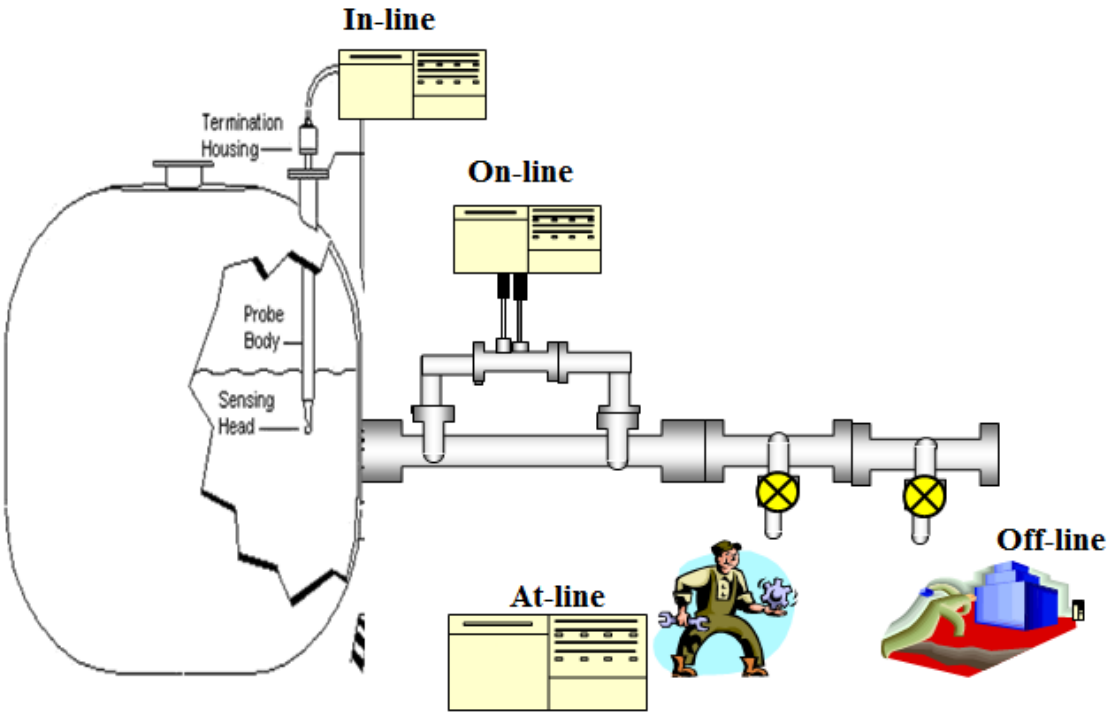

Figure 1.1 Pharmaceutical processes monitoring [2].

Raman spectroscopy plays a significant analytical role in molecular level process understanding in the pharmaceutical industry. Process and bench-top applications have been developed using Raman spectroscopy and can be applied for qualitative and quantitative process evaluation. Successful Raman spectroscopy applications in the pharmaceutical field include blend uniformity, reaction monitoring, solid quantification, coating monitoring and probably most significantly, crystallization monitoring and polymorph detection and analysis [3]. Significant technological development in the area of instrumentation has allowed the implementation of fiber optics, immersion and big spot size probes, and dispersive components into Raman systems, making them highly

robust and versatile tools for on-line and off-line characterization in the pharmaceutical industry [4].

This thesis, focused on the use of Raman spectroscopy as a characterization and sensing tool was part of a large effort supported by a National Science Foundation (NSF) funded Engineering Research Center (ERC) for Structured Organic Particulate Systems involving Rutgers University (lead), Purdue University, New Jersey Institute of Technology and the University of Puerto Rico at Mayaguez. The overall goal of the ERC was a national focal point for innovative science-based development of structured organic composite products and their manufacturing processes in the pharmaceutical industry. Work performed in this thesis was part of two projects within the ERC, one involving sensing for effective manufacturing and the other multilevel characterization of the composite products produced.

In this introductory chapter, the following sections will discuss the fundamentals of Raman spectroscopy in terms of its scientific background, instrumentation and techniques used in pharmaceutical research. Further, concepts of phase transitions in molecular crystals, the definition of the long- and short- range order in the solid state, and consequently the benefit of using the Raman technique to monitor crystallization/amorphization processes, will be discussed. The differences between Raman and fluorescence spectroscopy will also be illustrated. Other characterization techniques, such as Scanning Electron Microscopy (SEM), X-Ray Diffraction (XRD), and Differential Scanning Calorimetry (DCS) will be briefly introduced as they will be employed throughout this work to support the Raman spectroscopic data.

1.2 Raman Spectroscopy

1.2.1 The Raman Effect

In 1928, Sir Chandrasekhara Venkata Raman along with his colleague, Kariamanickam Srinivasa Krishnan, discovered "a new type of secondary radiation" [5] in sixty different common liquids. They observed a shift in the color of light scattered to some degree in most of the liquids simply by probing the samples with concentrated sun light. For this discovery, C. V. Raman was awarded the Nobel Prize in Physics in 1930 and the phenomenon that described the inelastic exchange of energy between light and matter was later named the Raman Effect.

When light interacts with matter, it can be either absorbed or scattered. During the scattering process, the majority of the light is scattered elastically at the same frequency and with no energy transfer between light and the molecule or solid. This is known as Rayleigh scattering. However, when the oscillating electric field of the incoming radiation interacts with molecules or the solid, there is also a small but finite possibility of the molecule or solid retaining the incoming photon's energy and generating vibrational excitations. This interaction is known as inelastic scattering of light or spontaneous Raman scattering when the interaction is non-resonant. The phenomenon is a low probability event and only 1 out of 10^7 photons will undergo inelastic scattering. During the interaction, the energy carried by incoming photons excites vibrational states within a molecule or a solid by distorting the electron clouds around molecular or intermolecular bonds in a solid. This shift in electron cloud distribution results in a change in bond polarizability (α) and induces a temporary dipole moment (P) and excites the molecule or solid into a virtual excited state when the interaction is non-resonant.

Since excited states do not have infinite lifetime, the scattering events occur in 10^{-12} seconds or less [6] after which the molecule or solid relaxes back to its ground state, emitting a photon at a specific frequency (ν_{vib}).

Depending on the energy difference between the original and the relaxed states, there is a change in the frequency of the emitted light from that of the incident light. Molecules or solids that relax back to the pre-excited state emit the same frequency (ν) light to give rise to elastic scattering. Molecules or solids that relax to a different vibrational state, however, emit a photon of different energy to give rise to inelastic scattering. This generated photon is shifted in frequency by an amount corresponding to the energy of a particular vibrational transition. If the final state is more energetic than the initial state, the emitted photon will be shifted to a lower energy $(\nu-\nu_{vib})$ which is designated as a Stokes shift. If the final state is less energetic, the emitted photon will be shifted to a higher frequency $(\nu+\nu_{vib})$ resulting in an anti-Stokes shift as shown in Figure 1.2. Such a change in energy gives rise to inelastic scattering of photons. The energy difference corresponds to a vibrational or rotational (librational in the case of solids) frequency of a molecule within gaseous, liquid and solid states, or of vibrations between molecules or ions in a solid, and is referred to as the Raman Effect.

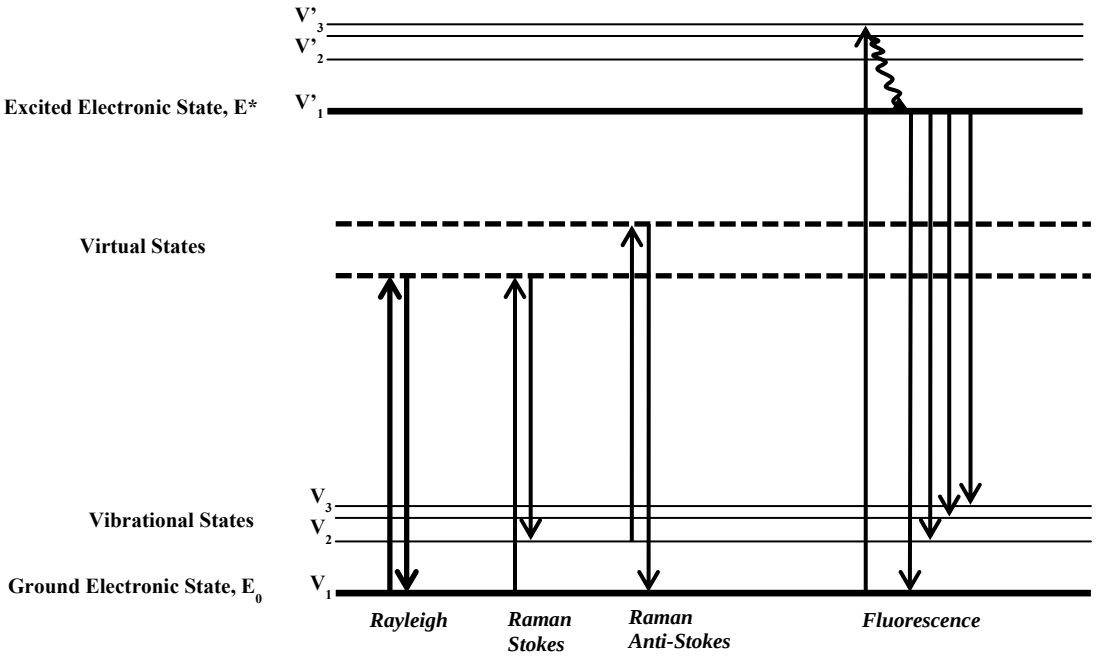

Figure 1.2 Rayleigh, Raman Stokes and anti-Stokes scattering, and fluorescence energy-level diagram.

The theory behind the Raman effect was derived by Austrian physicist, Adolf Smekal, five years prior to its discovery by C. V. Raman, who predicted the existence of stray lines with shifted frequencies [7]. Mathematical representation of Raman scattering can be expressed in terms of induced dipole moment in a diatomic molecule. The strength of the induced dipole moment (P) depends on the electrical field (E) of the incident electromagnetic radiation:

$$P = \alpha E \tag{1.1}$$

where α is the polarizability tensor of the molecule that measures the ease with which the electron charge cloud around the molecular bond is distorted. Considering the molecule

in the external electric field in terms of wave mechanics, one finds that the induced dipole moment is given by [6]:

$$P = \underbrace{\alpha_0 E_0 \cos(2\pi\nu t)}_{\text{Rayleigh}} + \underbrace{\frac{1}{2}\left(\frac{\partial\alpha}{\partial q}\right)_0 q_0 E_0 \cos(2\pi(\nu+\nu_{vib})t)}_{\text{anti-Stokes}} + \underbrace{\frac{1}{2}\left(\frac{\partial\alpha}{\partial q}\right)_0 q_0 E_0 \cos(2\pi(\nu-\nu_{vib})t)}_{\text{Stokes}} \qquad (1.2)$$

$\left(\frac{\partial\alpha}{\partial q}\right)_0$ - Rate of change of α with respect to the change in q at equilibrium position

The first term represents an oscillating dipole that elastically scatters the light of frequency *(ν)* corresponding to Rayleigh scattering. Induced dipole moments are created at distinct anti-Stokes $(\nu+\nu_{vib})$ and Stokes $(\nu-\nu_{vib})$ frequencies to give rise to inelastic scattered radiation at these frequencies. The necessary condition for Raman scattering to occur requires the bond polarizability to change as a function of bond length variation during the vibration. This is given by the polarizability derivative, $\left(\frac{\partial\alpha}{\partial q}\right)_0$ which is non-zero for a Raman-active vibration.

1.2.2 Raman Instrumentation and Techniques

Raman spectrometers can be either dispersive (for light sources in the visible and near-infrared range) or interferometer systems (for light sources in the infrared range). Most commonly used systems are dispersive and consist of a notch or edge filter for rejection of Rayleigh scattering, a monochromator for dispersion of the scattered radiation and a charge coupled device (CCD) array for photon detection as depicted in Figure 1.3 (a). The sample is excited with a laser source in the ultraviolet (UV), visible (Vis) or near

infrared (NIR) range, passed through a notch filter or monochromator to eliminate the intense Rayleigh scattering. The Raman resulting signal is then sent via a grating spectrometer to a CCD detector.

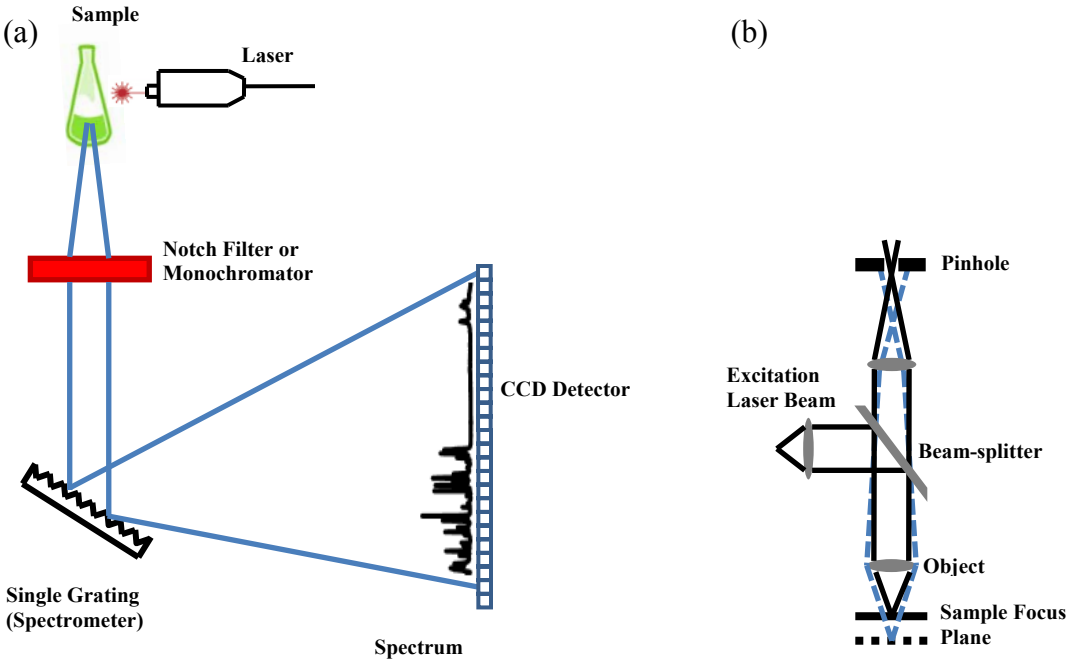

Figure 1.3 Raman spectrometers in: **(a)** Fiber optic and **(b)** Confocal geometries.

Raman sampling is a fast process and requires only a few seconds for a spectrum to be acquired to provide a wealth of information concerning the chemical composition and structure of the probed region. Optical fibers allow for remote or stand-off sample sensing since both the laser and scattered light travel through the same fiber optic probe. A micro-Raman spectrometer, although not designed for remote sampling, couples the spectrometer and incident light source to an optical microscope, thus allowing Raman analysis with a microscopic laser spot size which is ideal for probing micron to sub-micron scale sample features.

The sub-micron spatial resolution achieved by a Raman microscope allows for analysis of the solid state structure, and the spatial distribution of polymorphs and active particles in a composite. Combining the micro-Raman analysis with an automated stage allows the creation of a chemical map of a composite sample [8]. During mapping, a complete Raman spectrum is obtained for each pixel of the image and since each spectrum represents the fingerprint of a chemical species, the distribution of different materials and/or their local properties can be analyzed. By placing a small confocal pinhole in the focal plane of the microscope as indicated in Figure 1.3 (b), axial resolution can be further improved by allowing collection of spectra from a sample volume and creating depth profile of a sectioned specimen [9, 10].

In Fourier Transform (FT)-Raman spectroscopy an interferometer is used to produce an interferogram to encode the unique frequencies of the Raman spectrum into a single signal. The advantage of FT-Raman spectroscopy is mostly due to the use of an infrared laser (typically at 1064 nm) as the excitation source which minimizes the laser-induced fluorescence in the sample that can interfere with the weak Raman signal.

Several types of Raman spectroscopy have been developed to enhanced its sensitivity and improve spatial resolution. In this thesis, Surface Enhanced Raman Spectroscopy (SERS) will be discussed as a technique for improved detection limits through enhancement of the Raman signal from Raman-active analyte molecules adsorbed on gold coated photonic crystal-type arrays. The enhancement of the weak Raman signal by SERS relates primarily to two mechanisms: an electromagnetic enhancement induced by coupling to surface plasmons and a chemically-induced enhancement [11]. Chapter 5 will

discuss is some detail the basic principles behind SERS and illustrate its applications for rapid trace detection of pharmaceuticals and related organic molecules.

1.2.3 Raman Effect in Relation to Structural Disorder, Phase Transitions, and Particle Size

Modern Raman spectroscopy uses laser light sources to generate elastic and inelastic scattering to obtain vibrational spectroscopic information about molecules and solids. The so-called spectral fingerprint region in the 700 to 1900 cm^{-1} frequency range contains information about the frequencies or energies of key molecular vibrations. In addition, information about molecular rotations, and translations and hindered rotations (or librations) in a solid, is obtained from spectra below 200 cm^{-1}. The vibrational energies or frequencies depend on the mass of particular atoms in a molecule or an ion in an ionic solid, the nature of the chemical bonds connecting them, the symmetry of the molecular structure in a gas or liquid, and the local structure of the environment where they reside in a crystalline solid (Figure 1.4).

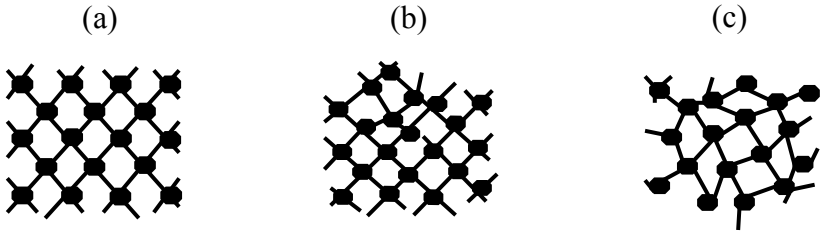

Figure 1.4 Schematic depictions of three types of order in a solid: **(a)** A periodic array with long-range order as in a crystalline solid; **(b)** A periodic array in a defected solid with short-range order, and **(c)** An amorphous solid.

Crystalline solids are composed of atoms/molecules or ions arranged in periodically repeating unit cells. This order, which is of long-range in bulk solids is linked to their optical, electrical, magnetic and mechanical properties. X-ray powder diffraction (XRPD) is routinely used to determine the crystallinity and average particle size in polycrystalline powders. However, many imperfections reside at short ranges which can be overlooked by XRPD. Among the most common imperfections in the crystalline lattice are point, linear, and planar defects that occur naturally in many materials [12] and can also be induced by mechanical processing via stress-induced perturbations. Induced disorder or defects at short range can propagate through the solid to give rise to longer range disorder or amorphization. Raman spectroscopy can provide information on structural variations at the molecular, short range scale and on crystallite sizes below the quantum localization limit through change of the intensities, frequencies, and linewidths of characteristic Raman lines. Moreover, decrease in line intensities can occur due to increased sizes of particles in a suspension because of decreased light throughput or increase diffuse reflectance [13]. This methodology can be used to determine the average particle size on-line in a suspension from calibration curves obtained on control samples using light scattering methods.

The Raman spectrum provides key structural information at various frequency ranges. It determines intra- and inter- molecular vibrations that correspond to different frequency ranges as depicted in Figure 1.5. In the crystalline state, it is involved with both molecular and inter-molecular translational and hindered molecular rotational or librational vibrations. In the solid state, the Raman-active vibrations are small wave

vector ($\boldsymbol{k}=2\pi/\lambda$, where λ is the wavelength) optical phonons, which are quantized collective vibrational excitations superimposed on each other as plane waves and propagating throughout an individual crystal. These vibrations are grouped into molecular vibrations that involve stretching (ν), bending (δ), and torsional (τ) oscillations, and lattice vibrations consisting of librational (hindered rotational) and translation motions. For compositional identification, molecular modes are typically

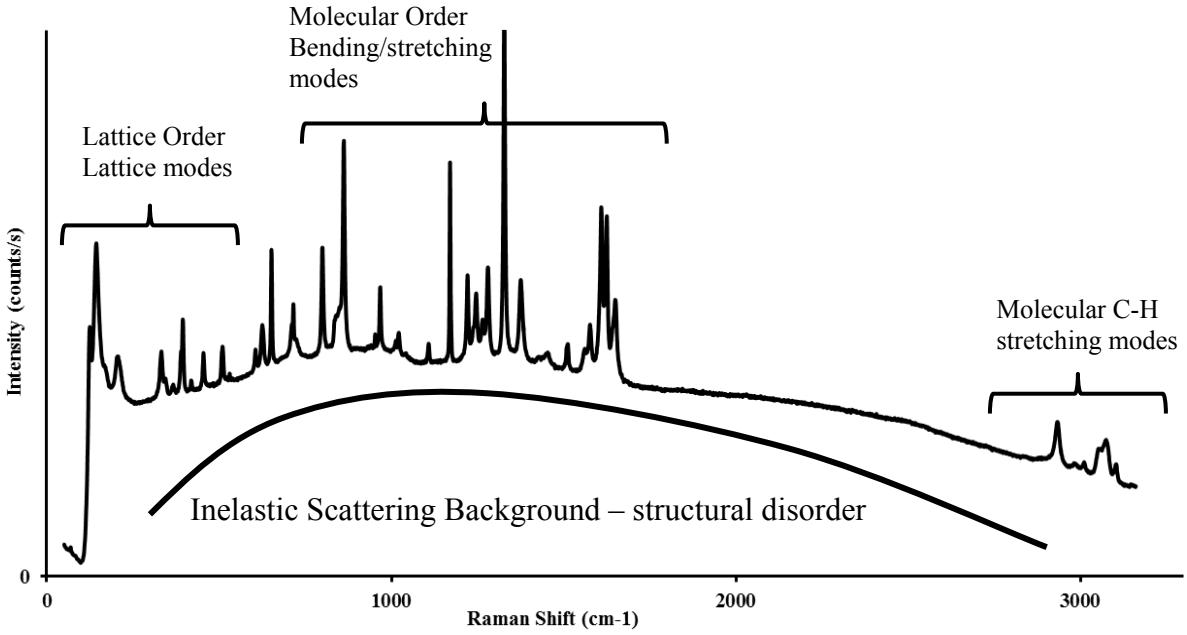

Figure 1.5 The Raman spectrum of a typical organic solid and the broad inelastic scattering background component associated with structural disorder. Information obtained from the data is also indicated.

studied since they are most sensitive to bond length and symmetry changes, and substitution of atoms, therefore giving information about the molecular structures involved [14].

Lattice modes are sensitive to the structural arrangement of the solid since they correspond to relative motions of the molecular units or ions in a unit cell of the lattice

[15]. These motions are categorized based on the direction in which the neighboring atoms oscillate. For Raman-active optical phonons, the vibrations correspond to transverse oscillations whereas acoustic phonons that are observed optically by Brillouin scattering at low $\boldsymbol{k}$ and at higher $\boldsymbol{k}$ by neutron scattering, oscillate longitudinally.

The total number of phonons propagating in a primitive crystal containing N unit cells each with p atoms is given by 3pN-6 (where the number of acoustic and optical modes is 3 and 3pN-3, respectively). The corresponding wave vectors ($\boldsymbol{k}$) belong to a volume of reciprocal space referred to as the Brillouin zone (BZ) [16]. Raman-active optical phonons in a crystalline solid occur at $\boldsymbol{k}$~0. However with decreasing crystallite size down to the amorphous level where long range order is lost, this rule is no longer valid and all phonons contribute to Raman scattering resulting in broad lines, frequency shifts and line asymmetry [17]. In the nanocrystalline phase, however, the situation is somewhat intermediate and the Raman spectrum displays broadened crystalline features which are shifted due to phonon confinement at the nanoscale [17, 18]. In addition, the symmetry of bulk crystalline materials can be broken in nano-crystals due to the high concentration of grain boundaries (coincident lattices), which also causes the appearance of specific surface modes as reported for silicon by Veprek et al [18]. In the case of nanocrystalline silicon it is found that below 3 nm a discontinuous transition to the amorphous phase occurs [16-18].

Raman spectroscopy is widely used for qualitative and quantitative characterization of polymorphs; it is also used to determine particle sizes in suspensions via changes in line intensity, crystal quality by monitoring linewidth and stress or strain by monitoring line frequencies (Figure 1.6). By definition, a polymorph is a crystal that can exist in two

or more crystalline phases, each having different crystal structures [19]. Phase identification is important because the material properties are highly dependent on structure. Raman spectra of polymorphs show changes in vibrational frequencies mainly because of different molecular and crystal symmetries in each polymorph due to changes in inter-molecular interactions influence the vibrational energies of each crystal structure. Amorphous forms loose long range order and give rise to broad lattice mode Raman

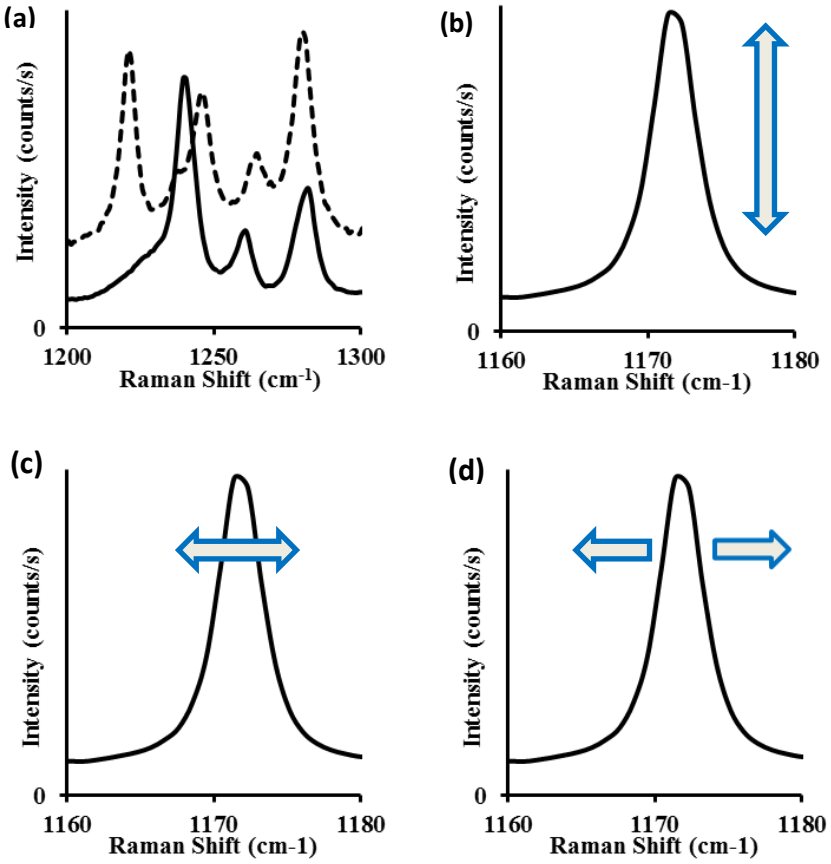

Figure 1.6 Changes in Raman lines due to: **(a)** Polymorphism – change in Raman peak frequencies, **(b)** Amount of material – change in intensity of Raman line, **(c)** Quality of crystal – change in Raman linewidth, **(d)** Application of stress or strain state – change in Raman line frequency.

spectra, although Raman lines due to molecular modes in the amorphous phase of organic crystals broaden but remain discrete since the molecules themselves are largely

unchanged. Intrinsically, spectral linewidths are inversely proportional to the lifetime of an excited state following the Heisenberg Uncertainty Principle [20]. Therefore, in bulk, highly crystalline solids, the excited states are long-lived and give rise to spectra with small linewidths. For example, by taking a Raman excited state lifetime of 10^{-12} seconds for single crystal silicon, the calculated peak width is 5 cm^{-1}, which is in agreement with the experimentally measured values for Raman scattering from single-crystal Si by Parker et al [20]. The phenomenon of phase transitions will be discussed further in Chapter 3.

Characterization at the Raman level as described above can provide better pharmaceutical products with innovative technologies involving drugs with nano-technological input. In order to build quality into these novel drugs, one therefore needs to have a thorough understanding of the material's behavior during manufacturing processes (including mechanical and chemical changes) and this is a critical aspect for building better quality products.

1.2.4 Distinguishing Raman Scattering from Fluorescence

The intensity of the Raman signal is proportional to the 4^{th} power of the excitation frequency. Short excitation laser wavelengths deliver highly intense Raman signals; for example, exciting a sample with blue light (400 nm) will give a Raman signal that is 16 times stronger than that obtained using red light at 800 nm. However, when using laser excitation wavelengths below 600 nm results in intense first order fluorescence from the samples.

Raman scattering, which is a weak effect, is often overshadowed by fluorescence emission from the sample arising from competing phenomena with similar origins but

higher cross-sections. In Raman spectroscopy, the laser photon interacts with a molecule in its ground electronic state with and without thermal excitation to gain (the anti-Stokes process) and lose (the Stokes process), respectively, a certain amount of energy corresponding to a vibrational frequency of the molecule via a virtual excited electronic state. The various frequency shifts associated with different atomic vibrations in the molecule give rise to a Raman spectrum that is unique for a specific molecule. The Stokes spectrum is typically more intense than the anti-Stokes spectrum because a smaller fraction of the molecules are thermally excited at room temperature.

In spontaneous, non-resonant Raman spectroscopy, the interaction of the photon and its re-emission occurs almost instantaneously (10^{-12} seconds or less) after excitation to a virtual excited state of the molecule followed by relaxation to vibrational states of the ground electronic level to generate a Raman spectrum on the higher (anti-Stokes) and lower (Stokes) energy side of the elastic Rayleigh scattering. The spectrum comprises of narrow emission lines associated with the vibrational modes of the molecule. The intense Rayleigh scattering is filtered out by a single or double monochromator, coupled to an optical notch filter. In contrast, fluorescence emission takes place by an absorption process to real electronic energy levels of the molecule followed by rapid relaxation from electronic and vibrational states down to the excited vibrational levels of the ground state as in Raman scattering. Therefore although the mechanism is different, the net result of both processes is essentially the same and in both cases a photon of energy with the frequency different from that of the incident photon is released by bringing the molecule to a higher or lower energy level. In fluorescence, the photon energy is absorbed by the molecular species from its ground electronic state to one of the various vibrational states

in the excited electronic state as shown in Figure 1.2. Following this, collisions with other molecules cause the excited molecule to lose vibrational energy until it reaches the lowest vibrational state of the excited electronic state. The molecule then drops down again to one of the various vibrational levels of the ground electronic state, emitting a photon in the process. Since the molecules can drop down into any of several vibrational levels in the ground state, the emitted photons will give rise to a broad envelope of different energies or frequencies. The lifetime of the excited state is much longer (ca. 10^{-8} to 10^{-5} seconds) [6] from which the molecule relaxes into various lower energy states, to produce the fluorescence spectrum. This results in high intensity, but lower chemical specificity because a broad envelope of energies is emitted. Moreover, fluorescence involves a resonant process between real electronic states and is therefore strongly dependent on the frequency or wavelength of the incident light [21]. The Raman effect on the other hand is typically spontaneous and excitation wavelength independent. It is a relatively weak process involving virtual states mediated by the molecular vibrations and associated with change in bond polarizability.

1.3 Other Characterization Techniques

Although the focus of this work is primarily on the use of Raman spectroscopy to characterize and study pharmaceutical powders, films and suspensions, other advanced analytical and imaging tools were also employed throughout this research. In the pharmaceutical industry these advanced methods are often used concomitantly in order to overcome the complex challenges of data interpretation and provide a more complete picture of the solid-state. This approach has also been employed in this research since

solid-state analysis requires more than one technique for effective analysis. In the following sub-sections, some of the techniques used will be briefly discussed while others will be considered in more detail in some of the following chapters.

1.3.1 Scanning Electron Microscopy (SEM)

Scanning Electron Microscopy (SEM) involves a high resolution microscope that uses a high-energy beam of electrons instead of light to form an image. This technique allows for physical characterization of the material surface as the signal results for the electron's interaction with the atoms at the sample surface. Since the magnetically focused beam of electrons is very narrow, SEM records microscale to nanoscale images with large depth of field, resulting in a three-dimensional appearance with spatial resolution on the order of 5 nm in the best microscopes. Physical characteristics, such as particle size, shape, and morphology of an active pharmaceutical ingredient (API) and associated excipients are important for pharmaceutical process understanding as they can influence the dissolution profile and drug bioavailability. Typical SEM images provide nanoscale visualization of the surface structure and morphology of pure and composite solids. Throughout this research SEM images were obtained with a VP-1530 Carl Zeiss LEO (Peabody, MA) field emission scanning electron microscope. The samples, which were all non-conducting, were mounted on aluminum stubs using double-sided carbon tape and sputter-coated with carbon to avoid charging.

1.3.2 X-Ray Powder Diffraction

X-Ray Powder Diffraction (XRPD) is a powerful technique that besides phase identification is largely used for determining the first order crystal structure, average crystallite size and stress in polycrystalline powders and composites. The small

wavelength of X-rays used to probe the sample, typically 1.54Å for CuK_α radiation in laboratory instruments, is comparable to inter-atomic distances and therefore gives structural arrangements of atoms and molecules when single crystal diffraction techniques are employed. To probe wider ranges in ***k*** space using XRPD, a small angle Synchrotron X-ray light source is used. In this thesis, laboratory scale wide angle XRPD and small-angle Synchrotron XRPD studies were performed to investigate the effect of mechanical milling on sample crystallinity and correlate the scale of structural changes with Raman results. For example, in Chapter 3, XRPD was used to confirm crystallinity and structure of the newly developed stable phase of acetaminophen.

All samples investigated in this study were analyzed using a wide-angle Philips X'pert PW3040 X-Ray Diffractiometer with CuK_α radiation (λ =1.5406 Å) operated at 40kV and 30mA, with 2θ ranging from 5° to 50°. Temperature-dependent small-angle Synchrotron X-ray powder diffraction measurements were conducted at the beam line X10A (λ=1.097Å) with a CCD detector at the National Synchrotron Light Source (NSLS), Brookhaven National Laboratory on a micronized griseofulvin sample as discussed in Chapter 2. The data were interpreted using parameters obtained from an Al_2O_3 reference.

1.3.3 Differential Scanning Calorimetry (DSC)

Thermal analysis techniques measure the physical stability and phase transitions of drug products and excipients during heat exposure. In particular, differential scanning calorimetry (DSC) measures the amount of heat required to increase the sample temperature in reference to the standard material. For polymorphs, the chemical entity remains the same but physical properties, such as density, melting point, or heat capacity

can vary due to different crystal packing from one polymorph to another. DSC is widely used for the initial detection and quantification of polymorphs since it measures the enthalpy term, ΔH, associated with the lattice energy difference [22]. In this study, DSC was performed with a FP900 Thermo System (Mettler-Toledo, Columbus, OH) comprising of a FP90 Central Processor and FP84HT TA Microscopy Cell. Sample weights were kept in a range between 6 to 8 mg and were heated at 5°C/minutes to a temperature exceeding the melting point of griseofulvin at 230°C.

1.4 Summary of Chapters to Follow

After this brief introduction to Raman spectroscopy in Chapter 1, Chapter 2 will discuss a multilevel characterization approach for processed pharmaceutical powders concentrating on structural disorder in cryomilled and amorphous griseofulvin. Cryogenic milling used to reduce particle size of soft crystals was observed also to induce structural disorder in griseofulvin indicated by broad inelastic Raman scattering and changes in intensities and splittings of some of the Raman lines with increasing levels of disorder [23]. Chapter 3 will discuss how process design can potentially utilize polymorphs, such as those of acetaminophen (APAP). The type II polymorph of APAP is metastable but highly attractive for pharmaceutical applications since it compresses and dissolves better than the stable type I polymorph. Novel behavior was observed for type II APAP prepared from milled and nano-coated acetaminophen powders. In addition, an oriented single crystal study of the behavior of Raman-active APAP vibrations as a function of temperature will be presented in Appendix A. Under favorable conditions of temperature, APAP can undergo a phase transition of the stable type I phase into metastable type II,

highly unstable type III, or even the amorphous type. Temperature-dependent molecular data of this type coupled with stress-dependent data obtained elsewhere can help generate predictive models for the behavior of crystallites of active pharmaceutical ingredients during manufacturing processes.

Applications of Raman spectroscopy as an on-line and in-line sensing tool will be presented in Chapter 4. They will be combined with off-line results of complementary Raman mapping and near IR chemical imaging which will be compared and analyzed for griseofulvin particle distribution, quantification and defect formation in newly developed polymeric films for pharmaceutical applications [24]. Chapter 5 will finish the thesis by illustrating the use of SERS phenomena induced by surface plasmon resonance for rapid trace detection of pharmaceuticals, and related organic molecules used in energetic formulations [25]. The closing Chapter 6 will provide a broad overview summary of the results obtained and suggestions for future work.

CHAPTER 2

SPECTROSCOPIC AND X-RAY DIFFRACTION STUDY OF STRUCTURAL DISORDER IN CRYOMILLED AND AMORPHOUS GRISEOFULVIN

2.1 Objective

Structural disorder induced by cryogenic milling and by heating to the amorphous phase in the active pharmaceutical ingredient, griseofulvin, has been studied by Raman spectroscopy, X-ray powder diffraction (XRPD) and fluorescence spectroscopy. A broad, exciting frequency-independent scattering background in the Raman spectra and changes in intensities and splitting of some of the Raman lines due to lattice and molecular modes, have been observed. In the cryomilled samples this strong background is deconvoluted into two components: one due to lattice disorder induced by cryomilling and the other due to Mie scattering from nanosized crystallites. A single-component background scattering attributed to lattice disorder is seen in the Raman spectrum of the amorphous sample. Fluorescence measurements showed an intrinsic fluorescence signal in as-received griseofulvin that does not correspond to the inelastic background in the Raman spectra, and moreover decreases in intensity on cryomilling, thus excluding an assignment of the Raman background intensity to impurity- or molecular defect- induced fluorescence. Wide-angle XRPD measurements on cryomilled griseofulvin shows a broad two-component background consistent with the background scattering component in the Raman data associated with lattice disorder at longer correlation lengths. Persistence of this disorder to even longer correlation lengths is evident from small-angle Synchrotron

XRPD data on micronized griseofulvin, which were taken as a function of temperature as the sample changes from the crystalline to the amorphous phase.

2.2 Introduction

Milling is widely used by the pharmaceutical industry to reduce the particle size of active pharmaceutical ingredients (APIs). Size reduction leads to increase in the surface to bulk ratio of the particle which enhances its bioavailability and dissolution rate. During milling, however, mechanical stress can induce changes in the crystal lattice of the API which will modify its physical and chemical properties. Both ball and jet milling, commonly used by industry, can affect crystal morphology and induce structural disorder [26]. These changes can cause crystal defects that are believed to mostly exist at the surface of the crystallites [27] and may originate from molecular conformational changes or unit cell distortions. Many types of defects exist and the most common ones include those due to varying grain sizes, edge dislocations and grain boundary effects [28]. Crystalline defects act as higher energy sites that are thermodynamically unstable compared to those in the stable crystalline form. Defects can progressively transform during processing into longer range disorder in atomic positions resulting eventually in the formation of an amorphous phase or a polymorph [29].

Raman spectroscopy is particularly sensitive to structural changes, see Chapter 1. The first order lattice or inter-molecular modes observed in Raman spectra typically occur at frequencies below 200 cm^{-1} [30, 31]. Lattice modes include translational and librational vibrations that are very sensitive to structural disorder and polymorphism. Intra-molecular deformation, rocking wagging, breathing and stretching modes which

typically lie in the frequency range above 200 cm^{-1} [32] are also sensitive to changes in the local crystal field caused by disorder or polymorph formation [33]. Therefore, changes in peak positions and intensities or the appearance of new lines in the Raman spectra would indicate the formation of defects or disorder, an amorphous phase or a new structural polymorph [34-36]. In addition, structural defects or disorder in the crystal may generate background scattering in the Raman spectra and diffuse scattering superimposed on X-ray diffraction patterns that resemble X-ray scattering from amorphous solids [18, 37-39]. Background intensity in Raman spectra is often caused by fluorescence when the excitation wavelength is close to an intrinsic electronic transition in the sample or it is caused by impurities introduced during processing or sample preparation. In both these cases the background intensity would vary with the excitation wavelength used. If the scattering background is excitation frequency-independent it may be attributed to other possibilities, especially if the material had undergone mechanical processing that can produce structural defects or disorder.

In the present study, cryomilled griseofulvin was investigated for defect and disorder formation and structural stability using spontaneous Raman scattering and X-ray powder diffraction (XRPD) techniques. Prior work by Bates *et al* [37] and Yamamura *et al* [38] focused primarily on x-ray diffraction studies of disorder in organic crystal systems, whereas Veprek *et al* [18] investigated the transition to the amorphous phase in silicon, a covalently bonded inorganic crystal, using both x-ray diffraction and Raman spectroscopy. In this paper, Raman spectroscopic and diffuse inelastic light scattering data have been obtained and correlated with x-ray diffraction and scattering data obtained from polycrystalline samples of as-received and processed griseofulvin, an organic solid,

and from amorphous griseofulvin. Quantitative estimates of crystallinity and particle sizes were obtained by differential scanning calorimetry (DSC) and from scanning electron microscope (SEM) images, respectively. The Raman spectra were examined using two different Raman instruments with different excitation wavelengths in order to rule out fluorescence and other extraneous effects in the data. Fluorescence spectroscopy, and wide-angle XRPD and small-angle XRPD using a Synchrotron source were also conducted. Laser and high humidity annealing experiments were performed to understand the nature of the defects and disorder induced by cryomilling. In laser annealing, heat is applied locally to form a thin solid-liquid interface not commonly formed in bulk thermal treatment. Laser annealing using rastering and broadening of the laser beam is therefore capable of rapidly removing defects and disorder [39]. The overall objective of the present work is to develop fast and non-destructive characterization of APIs like griseofulvin to detect mechanically-induced defects or disorder which could initiate the growth of undesirable polymorphic forms [40-42].

2.3 Experimental Materials and Methods

2.3.1 Materials

Crystalline Griseofulvin: Obtained from Sigma-Aldrich (St. Louis, MO) and stored at 0ºC in a freezer. Commercially available micronized griseofulvin, USP grade, was purchased from Spectrum Chemical (Gardena, CA) and also stored at 0ºC in a freezer.

Cryomilled Griseofulvin: Samples of cryomilled griseofulvin were prepared using cryogenic milling which was performed with a SPEX CertiPrep 6750 cryogenic impact mill (Metuchen, NJ) as described in reference [34]. The mill consisted of a cylindrical

vessel made out of polycarbonate within which a stainless steel rod was vibrated by means of an oscillating magnetic field. Liquid nitrogen was used to pre-cool 2 g of crystalline griseofulvin. After pre-cooling, the sample was milled in five cycles of 2 minutes milling and 2 minutes cooling. This milling process was repeated three times. Upon completion, the cryomilled material was placed in a cold water bath for around 10 minutes until it reached room temperature. It was then stored in a desiccator at 0^{o}C. Three cryomilled samples, referred to as samples 1, 2 and 3 in the text were prepared under these conditions.

Amorphous Griseofulvin: Two amorphous griseofulvin samples were prepared for this study, one from crystalline Sigma-Aldrich griseofulvin and the other from cryomilled griseofulvin. To obtain the amorphous form, small amounts of each sample were placed on a glass slide, heated on a hot plate at 220ºC (slightly above the melting point of 218ºC) until completely melted and then allowed to cool rapidly to room temperature to form a clear solidified film on the glass slide. Raman spectra were run immediately after preparation of the amorphous samples. The appearance of a strong peak at 656 cm^{-1} in the Raman spectra was used to confirm the formation of amorphous griseofulvin.

2.3.2 Methods

Raman Spectroscopy: Two different Raman instruments were used to collect Raman spectra: (a) A confocal Horiba- Jobin Yvon LabRam micro-Raman spectrometer with a 20 mW He-Ne laser source emitting at a wavelength of 632.8 nm focused to a spot size of 10 μm with a 10x lens; and (b) A Mesophotonics SE (Southampton, UK) 1000 Raman spectrometer calibrated to 2 cm^{-1} with a 250 mW near-infrared laser operating at 785 nm with a 130 μm diameter spot size.

Typical acquisition time for all spectra recorded was 10 sec per scanned spectrum. Each spectrum acquired using the Horiba-Jobin Yvon LabRam micro-Raman spectrometer was averaged over 2 scans. Data acquired with the Mesophotonics SE 1000 Raman spectrometer represent an average of 5 scans, for a total of 50 seconds. All Raman data shown are as-recorded by the instruments used. During spectral acquisition, powder samples were placed on glass substrates, whereas amorphous samples were both prepared and analyzed on glass substrates.

Spectral Deconvolution: The inelastic scattering Raman background and diffuse X-ray scattering background were fitted using a multi-peak fitting package provided in IGOR Pro software from WaveMetrics, Inc. (Lake Oswego, OR). Deconvolution was performed using both Lorentzian and Gaussian functions.

Annealing Procedures: The annealing of cryomilled griseofulvin samples was performed using two different methods – laser irradiation and exposure to high humidity conditions. The effects of the annealing were then monitored by Raman spectroscopy. Laser annealing was performed using 20 mW of focused 632.8 nm radiation from a He-Ne laser in the Horiba-Jobin Yvon LabRam micro-Raman spectrometer. Each sample was exposed to constant laser radiation for a total of 30 minutes, with spectra being obtained periodically. The initial spectrum was recorded prior to the laser treatment and the final spectrum was recorded upon completion of laser exposure.

Samples for monitoring the effect of high humidity were placed in a sealed desiccator along with a beaker containing approximately 50 mL of boiling hot de-ionized water and a humidity meter from Taylor Indoor Humidiguide (Las Cruces, NM). Humidity levels were maintained at 70-80% and the water was boiled again whenever the

humidity level dropped below 70%. The temperature was maintained between 21 - 23°C. Small amounts of sample were removed periodically for Raman measurements using the Mesophotonics SE 1000 Spectrometer and were disposed of after each measurement.

X-Ray Powder Diffraction: See Chapter 1 for wide-angle Philips X'pert PW3040 X-Ray Diffractiometer and small-angle Synchrotron X-ray powder diffraction measurements details.

Scanning Electron Microscopy (SEM): See Chapter 1 for details.

Differential Scanning Calorimetry (DSC): See Chapter 1 for details.

Fluorescence and UV-Vis Spectroscopy: Solid state fluorescence spectra were acquired at room temperature using a Hitachi F-3010 Fluorescence spectrophotometer (Schaumburg, IL) with a Xe lamp. The spectra were measured at a 60 cm^{-1}/minutes spectral rate and excitation wavelength (λ_{ex}) of 300 nm. The UV-Visible absorption spectrum corrected for the solvent signal was acquired with a Varian Cary 50 Bio UV-Visible spectrophotometer (Palo Alto, CA) using a 3 ppm solution of griseofulvin in acetone in a 3 ml quartz cuvette.

2.4 Results and Discussion

2.4.1 Scanning Electron Microscopy

Because particle size and shape can affect the Raman and XRPD data obtained, SEM imaging of the different griseofulvin samples were carried out. Representative SEM images from as-received micronized and cryomilled griseofulvin sample no. 3 used in this study are shown in Figures 2.1 (a) and (b), respectively. Reduction in crystallite sizes from the breakup of the rod-like particles in the micronized sample can be seen on

comparing the images. For example, the arrowed regions show fine grains in the nanometer size range for the cryomilled sample.

2.4.2 Raman Spectra of Crystalline, Cryomilled and Amorphous Griseofulvin

Crystalline molecular solids, such as griseofulvin, have the molecules organized in stable low energy conformations and in periodic arrays to produce an ordered lattice with inter- and intra-molecular vibrations which interact with light to give rise to well-resolved Raman spectra. This highly ordered structure can change under processing or high temperature conditions to a new crystalline structure, a defected or partially disordered

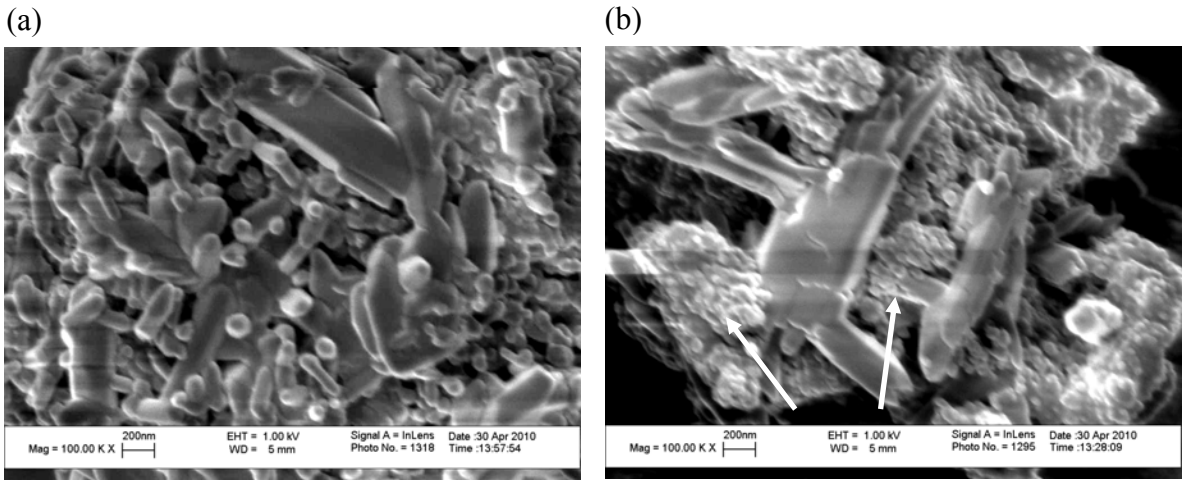

Figure 2.1 SEM images at a magnification of 100,000 of griseofulvin samples used. Panel (a) shows a typical image for commercially micronized griseofulvin and panel (b) show an image for cryomilled griseofulvin. Arrows indicate nano-sized grains in the cryomilled sample.

version of the structure, or an amorphous solid where the molecules are oriented in a random fashion while still maintaining their original stable conformation or a new conformation stabilized in the newly disordered lattice potential. The inter-molecular lattice modes of the crystalline phase are replaced by large amplitude diffusive or relaxational modes in the amorphous phase [43]. The lattice mode Raman lines of the

crystals broaden substantially in the amorphous phase whereas the intra-molecular vibrational lines remain largely unchanged if there is no change in molecular conformation. Typically, however, there are changes in molecular conformation and inter-molecular hydrogen bonding interactions in the amorphous phase and in polymorphs, resulting in shifts in line frequencies, linewidth broadening and changes in line intensities. In the case of a defected structure, the Raman spectrum will depend on the nature of the defects formed. Localized molecular defects would give rise to new lines in the molecular vibration frequency region coupled with excitation wavelength dependent fluorescence superimposed on the Raman spectrum as a broad signal. Crystal defects, such as dislocations and orientational defects of the type discussed by Feng *et al* [34] will most likely occur at grain boundaries created by milling. These defects give rise to longer range disorder manifested as a scattering background in the XRPD data, whereas shorter range disordered domains will give rise to a broad inelastic scattering background in the Raman spectra [15, 44]. These aspects of the Raman spectra and XRPD data from Griseofulvin will be discussed below. Milling-induced reduction in crystallite size to dimensions comparable to that of the Raman excitation wavelength can in addition give rise to excitation frequency independent Mie scattering superimposed on the Raman spectrum as discussed by Kiefer [45].

The Raman spectra of crystalline, cryomilled and amorphous griseofulvin obtained with 632.8 nm laser radiation using the confocal Horiba- Jobin Yvon LabRam micro-Raman spectrometer are shown in Figure 2.2. The observed Raman lines for the crystalline and amorphous samples, which are largely in agreement with the Fourier-

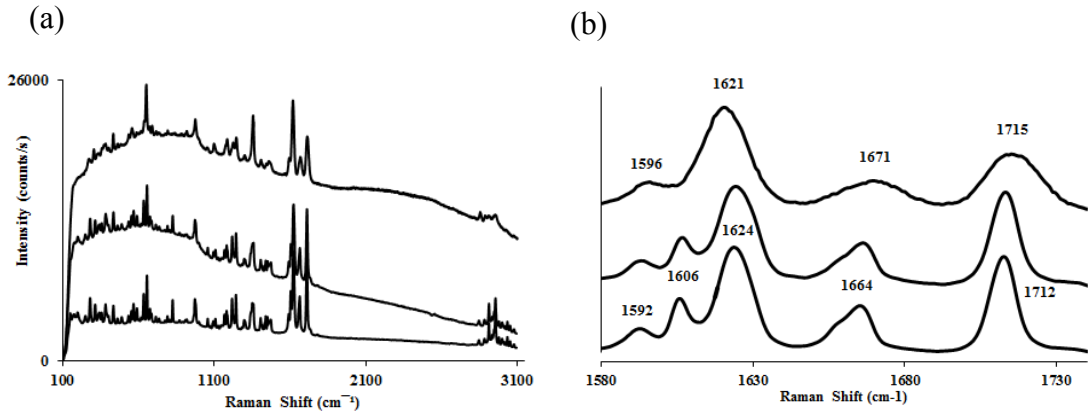

Figure 2.2 Raman spectra taken with the Horiba-Jobin Yvon LabRam micro-Raman spectrometer using 632.8 nm laser excitation in: (a) The 100 to 3300 cm^{-1} range of as-received, micronized crystalline griseofulvin (bottom), cryomilled griseofulvin sample no. 2 (middle), and amorphous griseofulvin (top); and (b) The corresponding zoomed spectra in the 1580 to 1740 cm^{-1} range.

transform Raman data of Feng *et al* [34], are listed and qualitatively assigned in Table 2.1.The lowest frequency lines at 152, 176 and 201 cm^{-1} in the crystalline phase are assigned to mainly translational lattice modes of the griseofulvin molecule. The lattice mode assignments have been made qualitatively in terms of a theoretical and experimental study of similar modes in the Raman spectrum of the molecular crystal sym-triazine [46], which showed that translational modes lie at higher frequencies than the librational lattice modes. The calculations in ref [46] also indicate that the translational eigenvectors in sym-triazine are mixed to some degree with those of the librational modes, and this may also be the case in griseofulvin. The lines at 253 and 283 cm^{-1} are tentatively assigned to second order translation-libration and molecular deformation-libration modes, respectively (see Table 2.1). Significant differences in relative peak intensities and positions can be observed when the spectra of amorphous and crystalline (or cryomilled) griseofulvin are compared. Most of these changes are evident in the low-frequency region discussed above, as well as in the lines from 500 to

1800 cm^{-1}, and from 2800 to 3200 cm^{-1}. The lines in the 560 and 640 cm^{-1} frequency regions [Figure 2.2 (b)] observed for both crystalline and cryomilled samples, become two broadened peaks in the amorphous sample with peaks at 565 cm^{-1} and 656 cm^{-1}, respectively, which are attributed to C-Cl stretching modes in the molecule [47]. It was noticed that the formation of a strong line at 656 cm^{-1} strongly correlates with the presence of a highly disordered or amorphous phase in the griseofulvin samples as evident from the zoomed spectra shown in Figure 2.2 (b). It appears as a strong line in amorphous griseofulvin (Figure 2.2 top) and in cryomilled sample 3 [Figure 2.3 (a)] which is 63% amorphous as determined [34] from the DSC data shown in Figure 2.4. The inset in the DSC scan in Figure 2.4 (b) shows a broad two step exothermic event for cryomilled griseofulvin sample 3 starting at 60^{o}C, which indicates crystallization of the disordered component in the sample. The DSC scan of the as-received micronized griseofulvin sample however shows high crystallinity with no indication of a crystallization transition [Figure 2.4 (a)]. However, a glass transition-like step is seen near 130^{o}C for both the micronized and cryomilled samples.

Table 2.1 Raman Frequencies and Qualitative Mode Assignments in Crystalline and Amorphous Griseofulvin

Crystalline Frequency (cm^{-1})	Intensity	Amorphous Frequency (cm^{-1})	Intensity	Qualitative Assignment
152	m	-	-	Translational lattice mode
176	m	-	-	Translational lattice mode
201	m	-	-	Translational lattice mode
253	w	-	-	Translation+libration
283	m	279	broad,w	Ring deformation + libration
315	m	310	broad,w	Out-of-plane ring deformation
344	w	-	-	Out-of-plane ring deformation
359	w	-	-	C-Cl deformation
384	m	385	broad,w	C-Cl deformation
435	m	439	broad,w	C-Cl deformation
555	w	560	broad,w	Ring stretching
570	m	-	-	C-Cl stretching
592	w	594	broad,w	C-Cl stretching
635	m	-	-	C-Cl stretching, ring deformation
658	s	656	s	C-Cl stretching
828	m	-	-	Cyclohexanone ring stretch
974	m	978	m	Benzene ring asymmetric stretch
1169	w	-	-	CH-rocking
1185	w	1189	broad,w	Ring vibration, -C-O-C stretch
1219	m	1228	broad,w	-CH in-plane deformation
1245	m	1249	broad,w	-CH in-plane deformation
1301	w	1307	broad,w	-CH in-phase twist
1353	broad,m	1360	sharp,s	-CH_3 and -CH_2 deformations
1440	w	1445	broad,w	-Asym CH_3 deformation
1454	w	1464	broad,w	-Asym CH_3 deformation
1467	m	1476	broad,w	-Asym CH_3 deformation
1592	w	1596	broad,w	C=O stretch
1606	w	-	-	C=O stretch
1624	s	1621	broad,s	C=O mixed with C=C stretch
1664	m	1671	broad,w	C=C stretch in cyclohexanone
1712	s	1715	broad,s	C=O stretch in benzofuran
2846	w	2855	broad,w	-CH symmetric stretch
2883	w	2887	broad,w	-CH_3 symmetrical stretch
2912	m	2913	broad,w	-CH_2 symmetrical stretch
2932	w	-	-	-CH_3 asymmetrical stretch
2955	m	2855	broad,m	-CH_2 asymmetrical stretch
2978	w	-	-	-CH_3 symmetrical stretch
3001	w	-	-	-CH_3 symmetrical stretch
3018	w	-	-	-CH_3 symmetrical stretch
3033	w	3032	broad,w	Aromatic =CH stretch
3052	w	-	-	-CH_3 asymmetrical stretch
3077	w	3078	broad,w	-CH_3 asymmetrical stretch
3107	w	3108	broad,w	-CH_3 asymmetrical stretch
3143	w	3138	broad,w	-CH_3 asymmetrical stretch

s – small, m – medium, w – week

Another feature in the Raman spectra is the disappearance of the 828 cm^{-1} line, attributed to the cyclohexanone ring stretching vibration, with decrease in crystallinity of the sample. The 1550 to 1800 cm^{-1} spectral range corresponding to the C=O stretching vibrational frequencies of the benzofuran ring [30] displays a characteristic triplet of lines which undergoes frequency shift, broadening, and decrease in relative peak intensity in the amorphous phase. For crystalline and cryomilled samples, the first peak of the triplet splits into three additional peaks at 1592, 1602, and 1624 cm^{-1} respectively [Figure 2.2 (b)], resulting probably from the interaction between the two C=O stretching modes and partial conjugation in the neighboring cyclohexanone ring where the π-electron system is delocalized [47, 48]. Conjugation in this part of the molecule is also significantly distorted due to the presence of a 2-methoxy group in the cis-conformation relative to the double bond on the cyclohexanone ring [49]. In the amorphous form, this splitting no longer exists and only two broader peaks, both shifted to higher frequencies, are observed.

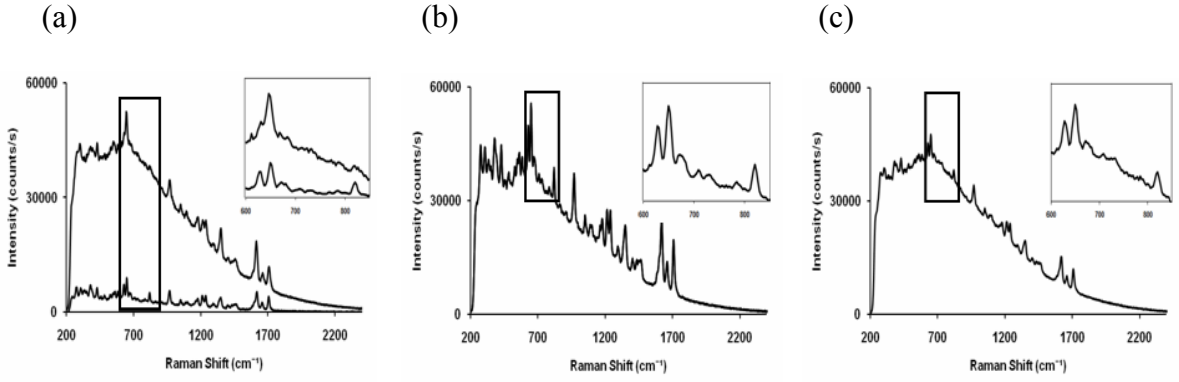

Figure 2.3 Raman spectra recorded with 785 nm excitation using the Mesophotonics SE 1000 spectrometer in the 100 to 2400 cm^{-1} range of: (a) As-received micronized griseofulvin sample (bottom) and cryomilled griseofulvin sample no. 3 (top), (b) Cryomilled griseofulvin sample no. 2, and (c) Cryomilled griseofulvin sample no 1. The boxed spectral region around 700 cm^{-1} on each panel are expanded and shown as insets on the top right of each panel.

Furthermore, examination of the C-H stretching region in the 2800 to 3150 cm^{-1} range shows substantial loss in intensities over several peaks in the amorphous phase due to changes in inter-molecular hydrogen bonding interactions.

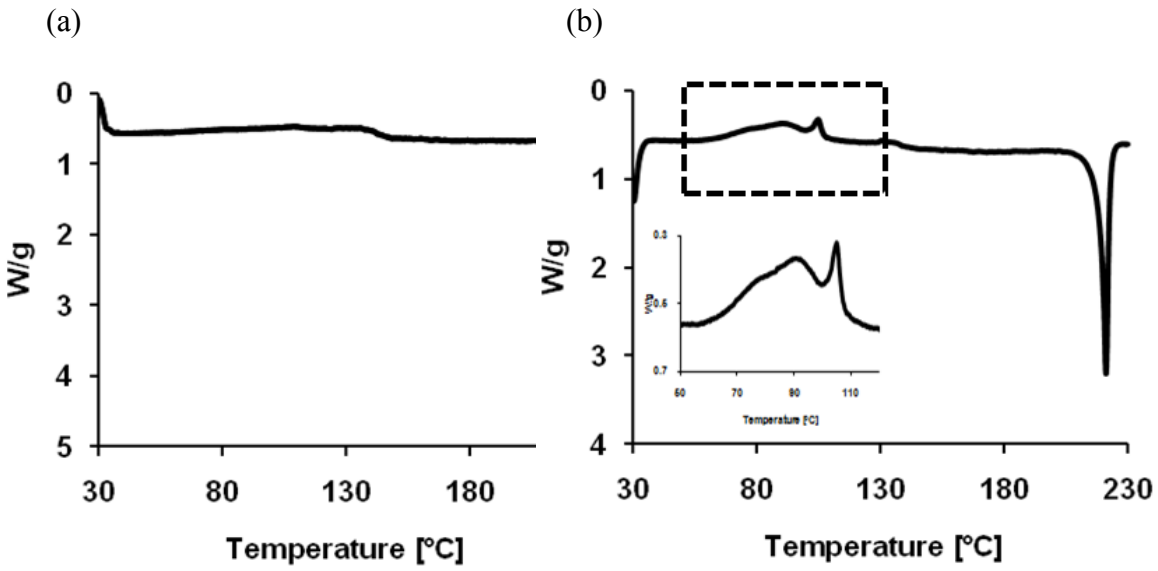

Figure 2.4 Differential scanning calorimeter scans for: (a) As-received micronized griseofulvin, and (b) Cryomilled griseofulvin sample 3. An expansion of the boxed-in region between 60 and 110°C is shown in the inset.

2.4.3 Inelastic Raman Scattering Background

A key feature in the Raman spectra is a superimposed broad, excitation energy-independent inelastic scattering background observed both in cryomilled and amorphous griseofulvin samples. This broad scattering was observed using two different Raman spectrometers operating with 632 and 785 nm laser sources as shown in Figure 2.2 and 2.3, respectively. As discussed below, the observed background does not correspond to fluoresence spectra taken from the same samples. This strong background in the Raman spectra is assigned to lattice disorder induced by cryomilling [34, 36]. In addition to this, particle size reduction to the range of the exciting laser wavelength will concomitantly

give rise to Mie scattering in the milled samples [45]. In the largely amorphous samples however the background scattering in the Raman spectra is primarily associated with lattice disorder.

The inelastic scattering background for cryomilled griseofulvin was fitted to two peaks using a Lorentzian function as shown in Figure 2.5 (a). The number of peaks included in the fitting was determined by the lowest residual value obtained during fitting. The two-peak fit suggests the existence of light scattering at two correlation lengths – the narrower one associated probably with Mie scattering resonances discussed earlier and the broader one to amorphous-like disorder in the sample. This is consistent with the fact that only a single peak fit is obtained for the amorphous sample in Figure 2.5 (b).

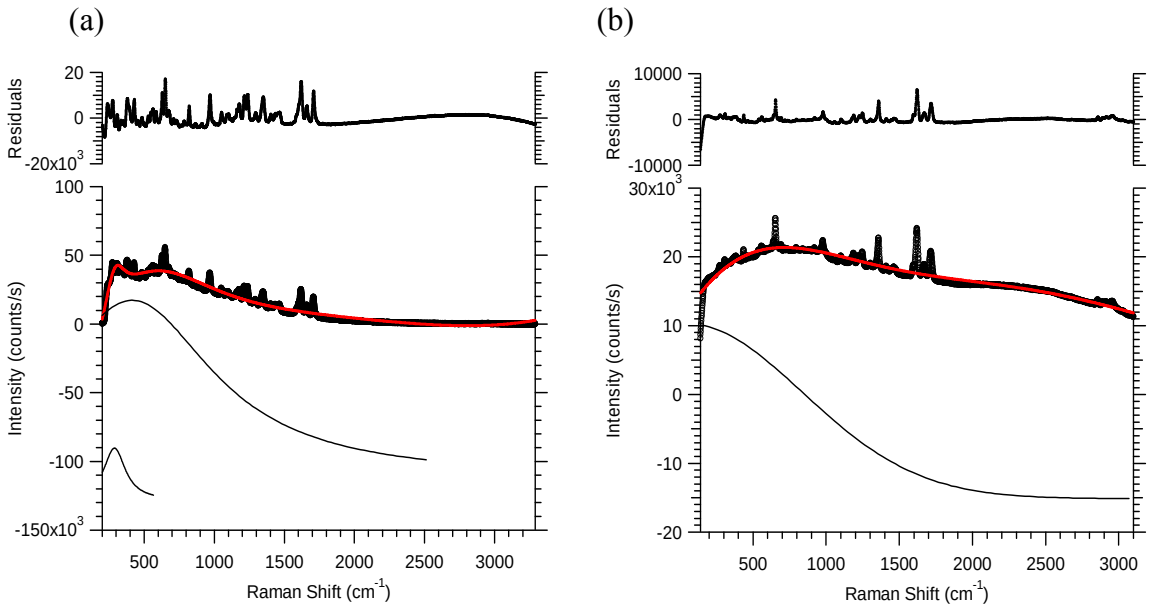

Figure 2.5 Fit of the inelastic Raman scattering background using a Lorentzian function. Panel (a) shows the fit for cryomilled griseofulvin sample 2, and panel (b) shows the fit for the amorphous griseofulvin sample.

To obtain further insight into cryomilling-induced disorder and Mie scattering, the effect on the Raman spectra of humidity and laser annealing of the cryomilled samples, was studied as described and interpreted below:

(a) Effect of exposure to high humidity

Humidity treatment is known to result in crystal growth by Oswald ripening. Griseofulvin is highly insoluble in water and exposure to water vapor in a humid atmosphere can modify its surface properties similar to water acting as a plasticizer [50]. The humidity treatment experiment conducted on cryomilled griseofulvin sample 1 showed a reduction in background intensity as observed by a consistent decrease in the inelastic scattering background compared with a minimal change in the as-received reference griseofulvin sample [Figure 2.6 (a)]. The cryomilled sample showed a reduction in background

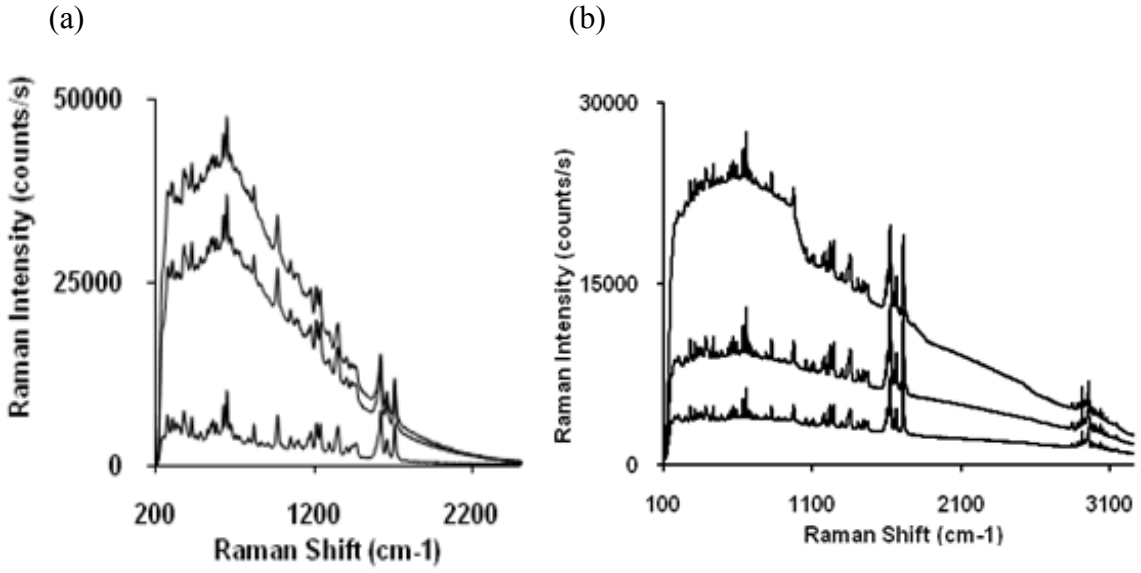

Figure 2.6 Comparison of the effect of annealing treatments on the Raman spectra of cryomilled griseofulvin after: (a) Humidity exposure taken with the Mesophotonics SE 1000 Raman spectrometer and 785 nm excitation, and (b) 30 minutes of 632 nm laser exposure taken with the Horiba-Jobin-Yvon Raman spectrometer. In each panel, the top spectrum is that of cryomilled griseofulvin sample 1, the middle spectrum is that of same cryomilled sample after annealing treatment (see text for details), and the bottom spectrum is that of as-received, micronized griseofulvin from Sigma Aldrich.

intensity at the location of the line at 656 cm^{-1} from the original baseline-corrected intensity of 41,709 counts/seconds to a value of 30,038 counts/seconds. This represented a 28% decrease in background intensity after seven days of exposure to high humidity. The background intensity remained at approximately 30,750 counts/seconds after seven days of exposure to high humidity, suggesting that most of the Oswald ripening occurred near the initial exposure. The baseline corrected background intensity of the reference sample remained essentially constant during this period. The observed decrease in Raman background intensity is also consistent with the assignment of this signal to crystallite size related disorder and Mie scattering rather than fluorescence.

(b) Effect of laser exposure

Laser annealing has been widely used to rapidly induce crystal nucleation in amorphous silicon films [51-53]. In the case of organic materials, there are few reports of successfully annealing crystal imperfections by inducing preferred molecular arrangements [54-56]. In this study on cryomilled griseofulvin sample 1 using focused 632.8 nm laser irradiation, the most pronounced annealing occurred after only 30 minutes of exposure as evident from Figure 2.6 (b). Background intensity was reduced for the peak at 656 cm^{-1} from the original value of 28,000 to 13,000 counts/seconds. This is a reduction of 54%, which can be attributed to annealing of defects and disorder due to growth in crystallite size. The relative intensity of the Raman signal remained constant with only minor deviation throughout the process indicating that no sample degradation was occurring. As pointed out in the Introduction, laser annealing applies heat locally and thus forms a solid-liquid interfacial strain region which is not formed in bulk thermal annealing. Laser annealing would therefore rapidly remove defects or disorder, and by

using rastering and broadening of the laser beam would have potential pharmaceutical application as a processing procedure.

2.4.4 Fluorescence Spectroscopy

Defect states can exist in the band gap of insulating and semiconducting solids [57] which give rise to fluorescence emission in molecular crystals with localized defects. As discussed above, the Raman spectra from cryomilled griseofulvin is associated with disorder and Mie scattering rather than localized defects. To further confirm this interpretation, solid state fluorescence spectra of cryomilled griseofulvin were measured and compared with the spectrum from as-received, micronized griseofulvin. The solvent corrected UV-visible spectrum of a griseofulvin solution in acetone showed a strong absorption band near 300 nm. This wavelength was therefore used to excite the fluorescence emission spectra from both the as-received and cryomilled samples of griseofulvin. The fluorescence spectra do show that as-received griseofulvin emits in the mid-infrared range, but the emission is partially quenched by cryomilling. Moreover, there is a lack of correspondence between the fluorescence and the background Raman spectra. This is evident from the combined plots of the Raman and fluorescence intensities versus wavelength shown in Figure 2.7.

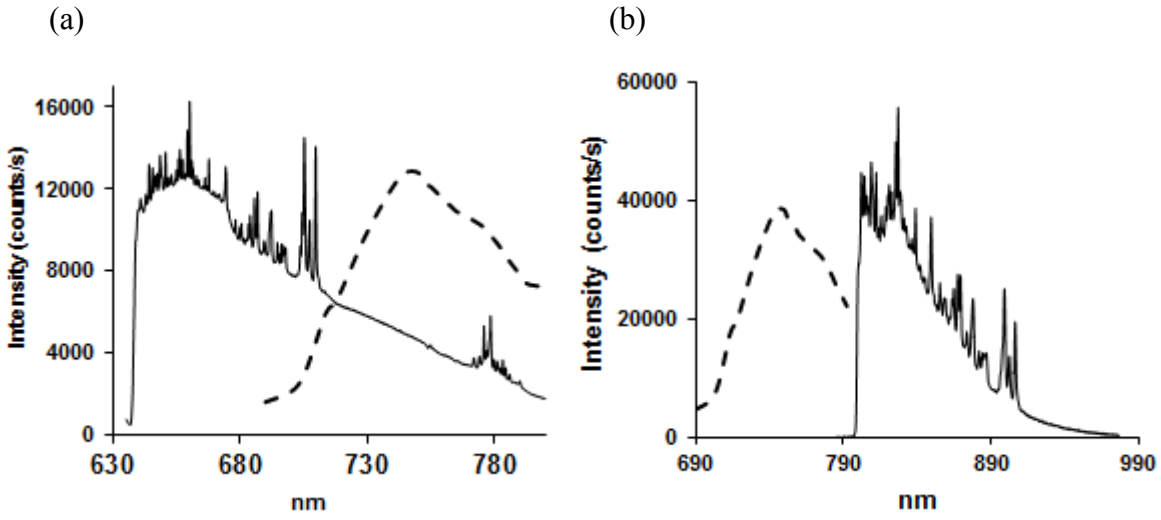

Figure 2.7 Raman (—) and fluorescence (---) spectral intensities plotted versus wavelengths for cryomilled griseofulvin sample 1. Panel (a) shows the combined plot of the Raman λ_{ex} = 632 nm spectrum taken using the confocal Horiba Jobin Yvon LabRam micro-Raman spectrometer and fluorescence spectrum taken with λ_{ex} = 300 nm. Panel (b) shows the combined plot of the Raman λ_{ex} = 785 nm taken using the Mesophotonics SE1000 Raman spectrometer and fluorescence spectrum taken with λ_{ex} = 300 nm.

2.4.5 Powder X-Ray Diffraction (XRPD)

Wide-angle XRPD diffraction and scattering data obtained using CuK_{α} radiation are shown in Figure 2.8 (a) for the as-received micronized and cryomilled griseofulvin sample 3, respectively. A broad scattering background is observed superimposed on the diffraction peaks in the cryomilled sample, but except for an increase in scattering at small angles, it is clearly absent in the as-received sample. The broad scattering in the cryomilled sample can be deconvoluted into two Gaussian components as shown in Figure 2.8 (b), pointing to the presence of disorder in the sample at two correlation lengths. The XRPD data from a micronized sample has also been obtained using a Synchroton X-ray source as a function of increasing temperature to the amorphous phase through the melting point at 218^{o}C, as shown in Figure 2.8 (c). As evident from the

figure, a two-peak small-angle background is seen in the crystalline phase which persists into the amorphous phase where the diffraction lines disappear.

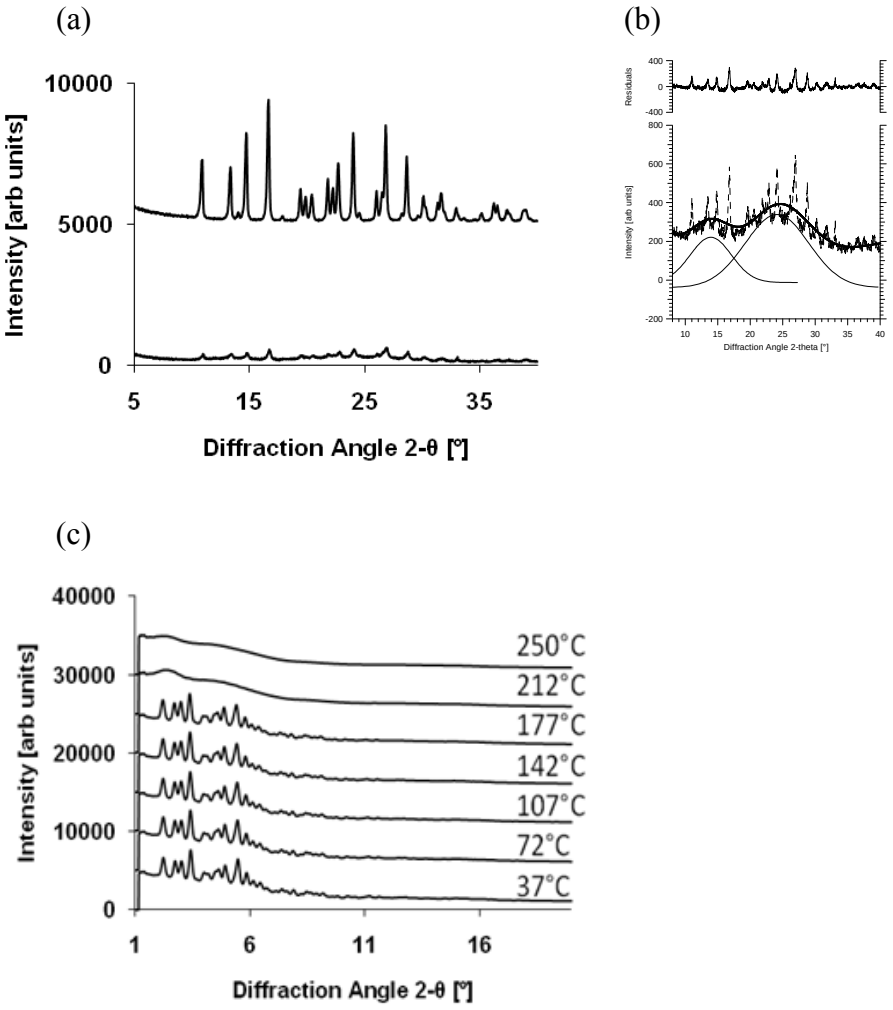

Figure 2.8 (a) Wide-angle X-ray powder diffraction patterns of cryomilled sample 3 (bottom) and as-received micronized griseofulvin (top) obtained using CuK_{α} radiation, λ =1.5406 Å; (b) Shows Gaussian function fits to the X-ray scattering background in the wide-angle diffraction pattern of cryomilled griseofulvin sample 3 shown in panel (a); and (c) Shows a sequence of plots of small-angle Synchrotron (1.09 Å) X-ray powder diffraction patterns of as-received micronized griseofulvin as a function of temperature to above the melting point at 218°C. The diffraction data in panels (a) and (b) have been offset for easy viewing.

2.5 Conclusions

A broad scattering background which can be deconvoluted into two components is observed in the Raman spectra of cryomilled griseofulvin relative to the spectra of reference samples of as-received, micronized griseofulvin. Comparison of the Raman with fluorescence spectra has ruled out fluorescence from molecular defects and impurities as the cause of the background scattering. It was concluded that structural disorder and associated Mie scattering centers on nanosized crystals are produced on cryomilling and contributes to the inelastic scattering background in the Raman spectra. Similar but more intense background scattering, which can be fitted to a single Lorentzian function, is seen in thermally produced amorphous griseofulvin. Wide-angle XRPD data on cryomilled griseofulvin shows a diffuse scattering component which can be fitted to two Gaussian functions due to disorder at two correlation lengths. Disorder at longer lengths has been probed by small-angle XRPD using Synchrotron radiation on micronized griseofulvin as a function of temperature from the crystalline to the amorphous phase. Disorder at two levels, which persists without much change into the amorphous phase, is also evident in this range.

Although it is widely known that Raman spectroscopy provides important information regarding the presence of crystalline and amorphous forms based particularly on the half-widths of Raman lines [15, 43], the results presented here show that additional effects like the onset of diffuse scattering superimposed on the Raman lines in organic solids can be used to assess the degree of disorder introduced as a result of mechanical processing. This will therefore expand the application of Raman spectroscopy to the characterization and quality control of active organic pharmaceuticals.

CHAPTER 3

POLYMORPH CHARACTERIZATION AND STABILIZATION IN PROCESSED AND UNPROCESSED ACETAMINOPHEN POWDERS

3.1 Objective

The objective of this chapter is to discuss and understand a novel approach developed here to stabilize the metastable type II acetaminophen (APAP) polymorph. A new interface of the stable type I APAP particles was created by micronization of the crystallites or by dry-coating with nanosized silica. These micronized and coated particles when converted to type II showed extensive long-term stability of the metastable type II phase. Type II APAP is commercially important because it is known to have improved tabletting properties. In previous studies, polymers have been used [58, 59] to formulate a more stable type II APAP phase. The newly developed type II stabilization discussed here can therefore have important implications in pharmaceutics.

Raman spectroscopy together with analysis by complementary techniques, such as X-ray powder diffraction (XRPD), and conventional and intrinsic dissolution were used to characterize the stabilized type II phase. The XRPD experiments also confirmed Raman data showing that no structural change to type II occurs when type I was initially micronized or dry-coated with nanosilica. Raman spectroscopy also showed the onset of a time-dependent background scattering in stabilized type II APAP. This scattering is similar to that seen in cryomilled griseofulvin [3] and is likely to be associated with the further growth of small amounts of initially formed nanosized nuclei of the stable type I polymorph detectable by XRPD, and defects associated with this growth process. It is

expected that further optimization of the stabilization process would make the type II phase indefinitely stable.

Topics that follow below are: Polymorphism in APAP, experimental methods used, interpretation of the Raman spectra of APAP in its different phases, Raman spectral monitoring as a function of time of the stabilized type II APAP, complementary characterization of the type II phase by other techniques, and conclusions. In addition, an oriented single crystal Raman study of type I APAP and a study of the spectra as a function of temperature were performed. The latter is important in understanding thermal changes that occur during milling processes employed to reduce particle size to improve drug dissolution for pharmaceutical applications. The results and discussion of the single crystal data are included in Appendix A at the end of this thesis. A corresponding uniaxial pressure study simulating another component of the milling process is planned in the future.

3.2 Polymorphism in Acetaminophen

Acetaminophen (APAP), one of the model drugs under investigation in this study is a widely used analgesic drug and it is an excellent example of a polymorphic system as it is known to exist in three forms with different crystalline packing, and a disordered, amorphous form. Type I APAP is a monoclinic crystal, type II is orthorhombic, whereas type III is too unstable for its structure to be determined. Type I (commercially available) is the most stable at room temperature, but it has poor binding and densification properties [60]. Both types I and II phases can be grown out of the molten state of APAP crystals. The unstable type III can also be grown from the melt but only between two

surfaces. From the commercial point of view, it is desirable to stabilize the metastable type II due to its enhanced compression behavior and higher intrinsic dissolution rate [61, 62] compared to phase I. The compression properties of type I and II polymorphs relate to different molecular packing in the two forms. The molecules form puckered layers in the type I polymorph and flat sheets or layers in type II, as evident from Figures 3.1 (a) and (b), respectively. Van der Waals intermolecular bonding occurs between the sheets and stronger intermolecular hydrogen bonding exists among the molecules in the sheets. As shown in Figure 3.2 (b), two types of hydrogen bonding, NH···O and OH···O, which differ significantly in their corresponding bond lengths - 2.91 Å and 2.65Å in type I and 2.97Å and 2.72Å in type II phases, are observed in APAP crystals [42]. The shorter (stronger) intra-layer hydrogen bonding in type I results in its higher melting point and greater thermodynamic stability relative to the type II phase [63, 64]. Another interesting feature is the higher plastic deformability of type II relative to the type I phase, which is consistent with its flat layered architecture in contrast to the puckered architecture of the molecules in the type I phase.

(a) (b)

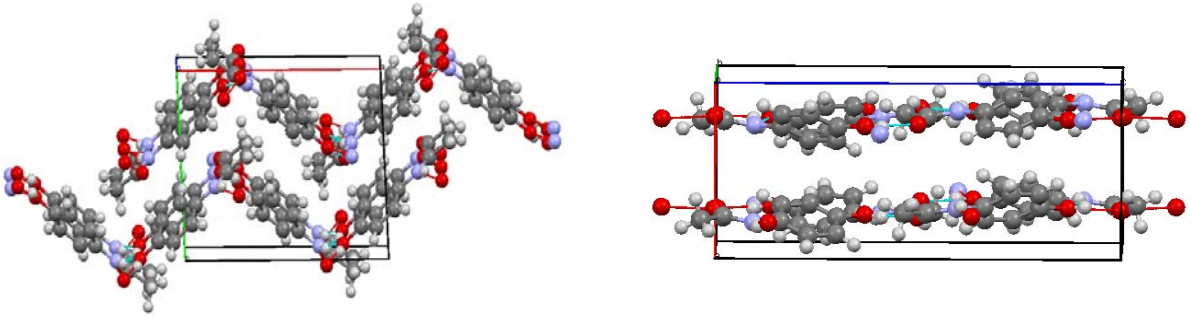

Figure 3.1 Unit cells of acetaminophen in: (a) Type I, and (b) Type II phases.

(a) (b)

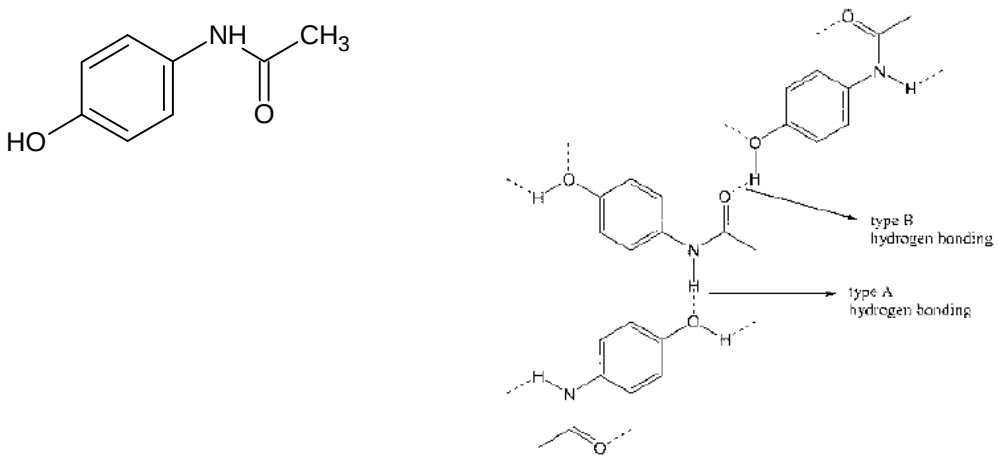

Figure 3.2 (a) Molecular structure of acetaminophen, and (b) Type A and type B hydrogen bonding between acetaminophen molecules in type I and type II acetaminophen phases [42].

The relative orientation of layers of acetaminophen molecules in each structural type relates to compaction properties and behavior of each phase under pressure. The more planar orientation of the sheets in type II is attributed to its well-developed slip system and higher plastic deformability [65]. Type I does not deform plastically since the relative orientation of the molecular sheets resembles a zig-zag or puckered arrangement. As a result, type I breaks by brittle fracture and requires binding agents during manufacture to ensure that the tablets remain intact after compression.

Based on structural orientations, APAP can be classified as an unstable crystal compared to the relatively stable griseofulvin which shows no polymorphic transitions except for the amorphous state. It is of importance to understand how process design can potentially benefit from polymorphic transitions of a crystal [66]. A large number of publications have been devoted to APAP behavior during pharmaceutical processing [59-

61, 67, 68] since its polymorphism is known to influence mechanical properties and dissolution rate. In particular, the more elastic but metastable type II APAP can be compressed directly but it transforms to the stable type I form within days. Several techniques have been employed to stabilize type I APAP by using stabilization agents, such a gelatin, polyvinylpyrrolidone (PVP) or starch [69]. Di Martino prepared the pure orthorhombic type II phase of APAP for direct compression with fairly good results and stability up to 11 months [67]. In the present study, two methods are used to increase the stability of type II APAP. In the first method, metastable type II APAP is produced from the melt using micronized type I APAP. In the second method, unmicronized type I APAP is dry-coated with nano-silica and then type II APAP is generated from it.

3.3 Experimental Methods and Details

In this section the sources and preparation of the following APAP samples and characterization methods used are described:

APAP I – Purchased form AnMar International Ltd (Bridgeport, CT), and used as-received.

MAPAP (micronized APAP) I – Purchased form AnMar International Ltd (Bridgeport, CT), and used as-received.

SiO_2 APAP I – Hydrophilic Nano-silica was purchased from Cabot Corp (U.S.A). SEM characterization showed the particle size of nano-silica to be about 40 nm. APAP I was coated with 1% (w/w) nano-silica using the dry-coating technique described below.

Raman spectroscopy confirmed that no chemical and structural changes resulted from nano-silica dry coating.

Dry coating: The dry particle coating used the technique of magnetic assisted impaction coating (MAIC), to disperse the nano-sized guest silica particles onto the surface of the primary host particles. The dry particle method is discussed in detail in reference [70] and was performed by Laila Jallo in Prof. Rajesh Dave's group at NJIT.

APAP II – Normal type II APAP was generated from as-received crystalline type I APAP. A few milligrams of APAP I was placed on a glass slide and melted at 190°C. To obtain the type II phase, the hot melt was rapidly cooled in a freezer resulting in a thin film of sample on the glass slide.

MAPAP (micronized APAP) II – Type II APAP was generated from MAPAP I following the same procedure as for APAP II.

SiO_2 APAP II – Type II APAP was generated from SiO_2 APAP I following the same procedure as for APAP II.

All samples prepared in this manner were stored in ambient conditions.

The formation of the orthorhombic phase II in all fabricated samples of acetaminophen, in particular APAP II, MAPAP II, and SiO_2 APAP II in thin films or crushed powders (for dissolution studies) were confirmed by Raman spectroscopy.

Conventional Dissolution Rate (CDR): Dissolution analysis was performed using a basket dissolution tester Distek 2100A USP apparatus 1 (North Brunswick, NJ). Samples were tested according to the USP29-NF24 monogram for acetaminophen capsules. The dissolution profile was obtained as per specified monogram conditions using a dissolution tank with six dissolution vessels, 900 ml each, equipped with rotating baskets with samples. Approximately 50 mg of sample was enclosed in a gelatin capsule as shown in Figure 3.3 (a) and placed in each of the dissolution baskets, immersed into the

vessel with DI water at 37°C, and rotated at a constant speed of 50 rpm. The water bath temperature was constant during the experiment.

Aliquots of 5 ml were removed at time interval, t = 0, 5, 10, 15, 20, 25 and 30 minutes and analyzed using a UV-vis spectrophotometer (for instrument details see Chapter 2). A calibration curve was generated by a set of freshly prepared standard solutions of 0.005 mg/ml, 0.010 mg/ml, 0.025 mg/ml, 0.050 mg/ml, and 0.060 mg/ml concentrations of as-received type I acetaminophen in water. All samples were run in triplicate to create a dissolution profile and reliable data set. Dissolution analyses were performed for the following types of acetaminophen: APAP I, APAPA II, MAPAP II, and SiO_2 APAP II.

Intrinsic Dissolution Rate (IDR): A Venkel, VK 7000 dissolution apparatus equipped with compacted and rotating disk was employed, as shown in Figure 3.3 (b) to perform

(a) (b)

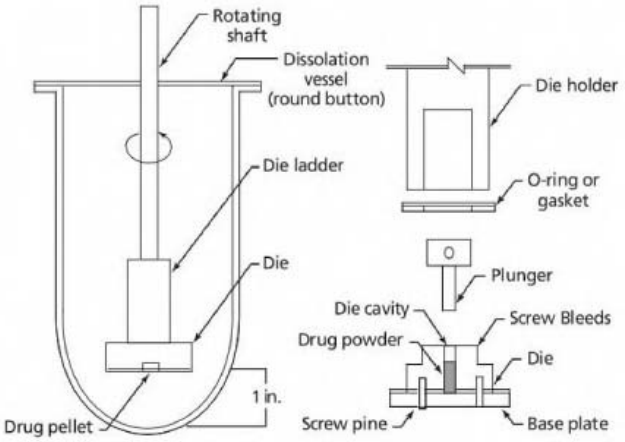

Figure 3.3 (a) APAP capsule used for conventional dissolution analysis, and (b) Schematic of an intrinsic dissolution apparatus consisting of a steel plunger and a die, and a rotating shaft with attached sample holder immersed in the dissolution vessel [71].

intrinsic dissolution on four batches of acetaminophen: APAP I, APAP II, MAPAP II, and SiO_2 APAP II. Sampling and experimental conditions were the same as described above for the conventional dissolution rate study. A typical IDR apparatus consists of a steel plunger and die, and a stainless steel sample holder for direct compaction as shown in Figure 3.3 (b). Approximately 40 mg powder sample of APAP I was directly compressed using a hydraulic press Carver Press, Model C, applying a pressure of 3 kN for 30 seconds to form a 0.6 mm diameter disc inside the sample holder. The same procedure was repeated for the remaining batches, where for each batch analysis was performed in triplicate. The sample holder was attached to the rotating shaft and immersed into the dissolution bath. Prior to analysis, the air pockets formed at the bottom of the sample holder during immersion were carefully removed. Using a Cary 50 UV-vis spectrometer, and a set of standards of the same concentrations as above, the mass of dissolved acetaminophen was calculated after correcting for the change in volume and including the disk area. The IDR analysis was performed in collaboration with Dr Shirlyn Chen's group at Boehringer-Ingelheim, Ridgefield, CT.

For both types of dissolution testing, thin films were gently crushed to generate powders which were then confirmed to be type II APAP by Raman spectroscopy.

For brief descriptions of Raman spectroscopy, small and wide angle XRD, and SEM instrumentation, see Chapter 2.

3.4 Raman Spectra of Acetaminophen Polymorphs

After X-ray diffraction, Raman scattering is one of the most widely used methods employed to study polymorphism and structural transformations because of its high sensitivity to crystalline structure. In the case of acetaminophen, three different

arrangements of the molecules in the crystalline state are known besides the disordered amorphous phase obtained from the melt. Among the three phases only type I is known to be thermodynamically stable and is the form that is used in pharmaceutical applications. However, it was discovered in this work that composite formation due to dry coating with nanoscale silica and surface modification by top-down micronization provide long-term stability to type II APAP possibly via the formation of a new interface which stabilizes the molecular architecture of this normally metastable phase. As previously discussed in Chapters 1 and 2, Raman spectroscopy is particularly suited to understand evolving structural behavior and is therefore used here as the primary tool to monitor the changes in type II APAP as a function of elapsed time. Raman spectra shown in Figure 3.4, together with the frequencies and their possible assignments in Table 3.1, for all four types of APAP have been measured down to 100 cm^{-1} and are in essential agreement with the data previously reported by both Szelagiewicz *et al* [72] and Kauffman *et al* [73]. Raman lines below 200 cm^{-1}, studied for the first time to the best of our knowledge, are assigned to inter-molecular or lattice modes which are particularly sensitive to the crystalline arrangements and clearly show differences between the four types of APAP phases. For type I, the lowest frequency lines at 136 cm^{-1} and 155 cm^{-1} are assigned to largely translational motions of the acetaminophen molecule, similar to observations in griseofulvin discussed in Chapter 2. Both of these lines shift to lower frequencies (127 cm^{-1} and 145 cm^{-1}, respectively) in type II APAP. In the amorphous phase, long-range crystalline order is lost and the molecules are randomly oriented. The low frequency Raman lines persist in the amorphous phase due to some short-range order but are substantially broadened due to long-range disorder. The low frequency Raman spectrum

of type III APAP is interesting. The translational mode features are not evident and appear to be embedded in a broad scattering background similar to that seen in cryomilled griseofulvin (see Chapter 2). The observation of a strong scattering background suggests that the type III structure is highly defected and probably stabilized by these defects.

Raman lines attributed to intra-molecular vibrational modes are observed at frequencies above 200 cm^{-1} for the different polymorphs and the amorphous phase as shown in Figure 3.4 (a). Changes in these lines occur in the different phases due to changes in local potentials and are more subtle than those for the Raman features assigned to inter-molecular or lattice vibrations discussed above. More detailed views of the Raman features in the spectral regions between 1200 to 1280 cm^{-1} and between 1500 to 1650 cm^{-1} are indicated in Figures 3.4 (b) and (c), respectively. The Raman lines in the 1200 to 1260 cm^{-1} frequency region correspond to C-N, C-H, and phenyl ring vibrations [47]. The characteristic C-N stretching Raman line at 1237 cm^{-1} for type I APAP develops into two well resolved peaks at 1221 cm^{-1} and 1245 cm^{-1} in type II APAP due to change in local symmetry. Further, there is substantial broadening of the 1237 cm^{-1} line in the amorphous phase with almost no frequency shift relative to that of the line in the type I phase. In the type III phase this line broadens and upshifts by 6 cm^{-1} to 1243 cm^{-1} indicating some strengthening of the C-N bond.

Additionally, other changes in the intra-molecular vibrational lines are observed in the Raman spectra as a function of crystalline polymorph or amorphous phase in the 1500 to 1650 cm^{-1} frequency region shown in Figure 3.4 (c). Here, changes occur in the relative intensities and peak positions of Raman lines that are attributed to –N-H

deformation and C=O stretching modes. The strongest lines for type I APAP are seen at 1611 cm^{-1} and 1649 cm^{-1} and are assigned to –N-H deformation and C=O stretching modes, respectively. In the amorphous phase both of these lines upshift by 9 cm^{-1} together with significant broadening as well as increase and decrease in relative peak intensity, respectively. These changes are most likely associated with the absence of ordered intermolecular interaction in the amorphous phase and type A and B hydrogen bonding explained above. The upshift in the peak positions indicate that the force constants for N-H deformation and C=O stretching increase probably because inter-molecular interactions are disrupted in the amorphous phase. In case of type III APAP intermolecular interactions persist, and the line at 1611 cm^{-1} upshifts by 3 cm^{-1} whereas the line at 1649 cm^{-1} downshifts by 2 cm^{-1} due to changes in the local inter-molecular potentials. For type II, the type I APAP line at1611 cm^{-1} splits into two peaks at 1578 cm^{-1} and 1623 cm^{-1} indicating substantial changes in the hydrogen bonding interactions.

(a)

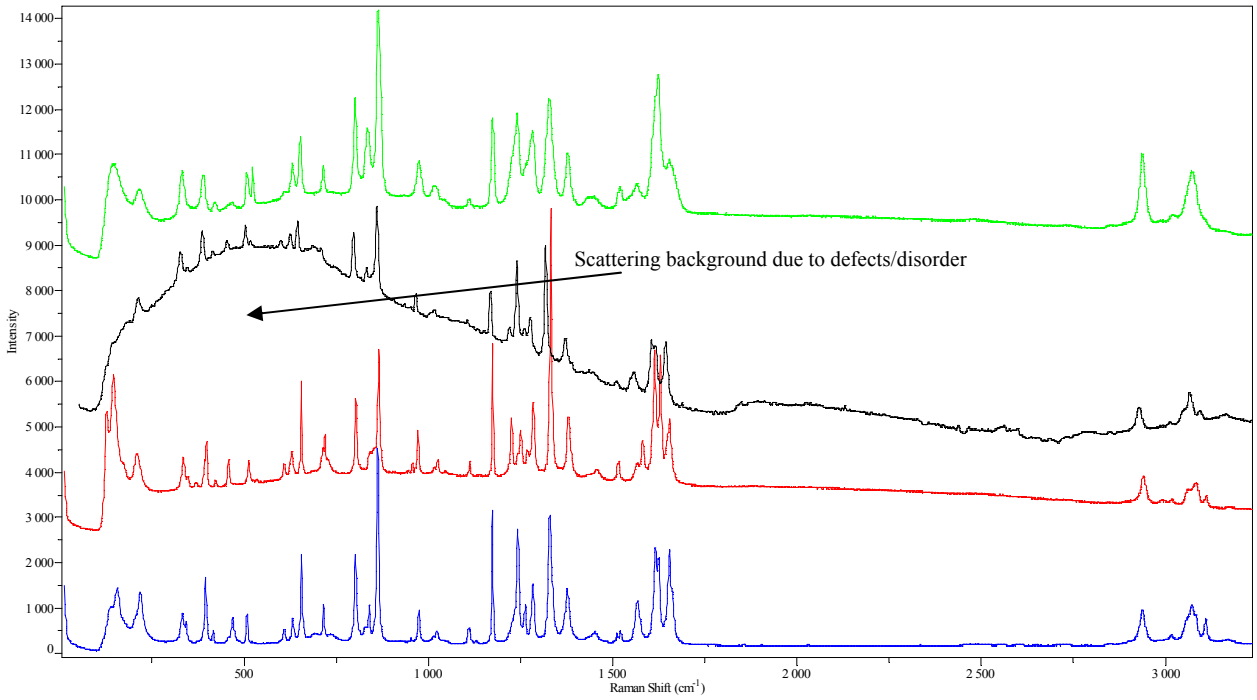

(b) (c)

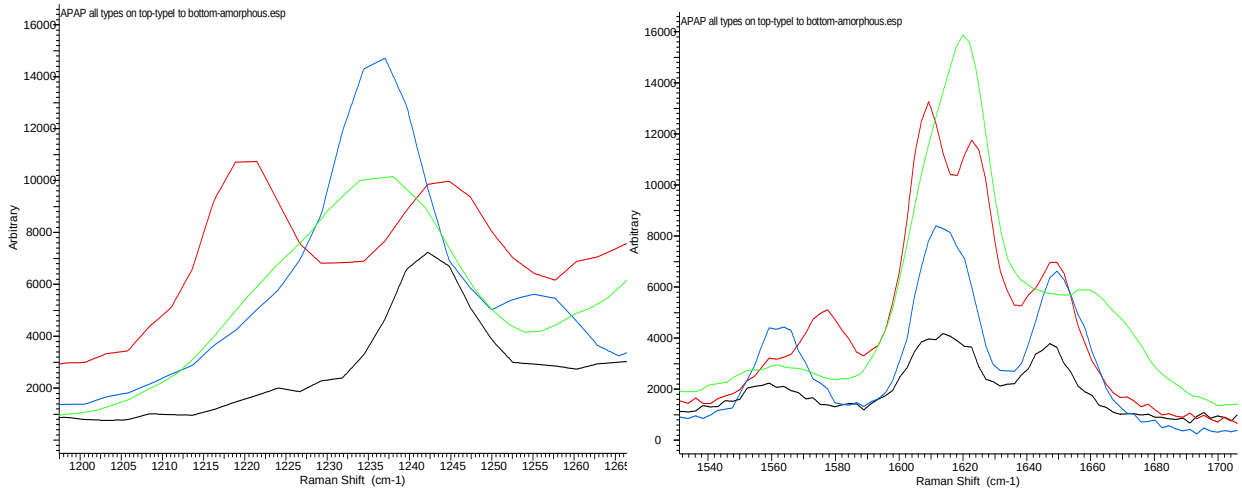

Figure 3.4 Raman spectra of acetaminophen polymorphs and its amorphous phase prepared directly from its stable type I phase in the spectral regions: (a) 100 to 3500 cm^{-1}, (b) 1200 to 1260 cm^{-1}, and (c) 1500 to 1650 cm^{-1}. Color coding: Green (amorphous), blue (type I), red (type II) and black (type III).

Table 3.1 Raman Frequencies and Qualitative Mode Assignments of Acetaminophen in its Three Polymorphic and Amorphous Phases

Type I (cm^{-1})	Type II (cm^{-1})	Type III (cm^{-1})	Amorphous (cm^{-1})	Qualitative Assignments
135	127	-	-	
155	145	146	143	Translational lattice modes
-	172	183	-	
205	208	210	-	
218	-	-	215	
326	330	330	330	Out-of-plane ring deformation
388	388	388	388	
462	452	457	458	Out-of-plane ring deformation
501	5050	505	508	Out-of-plane ring deformation
649	649	646	650	In-plane ring deformation
796	796	799	800	Phenyl ring stretch [74]
839	-	-	831	C-H out-of-plane bend
856	856	862	864	Phenyl ring C-H stretching
1169	1169	1172	1174	C-H in-plane bend
-	1221	-	-	C-C stretch carbon phenyl ring
1237	-	-	1238	C-N stretch
-	1245	1242	-	
1278	1278	1278	1280	O-H and C-O combination, (ar) C-N stretch
1324	1326	1321	1328	C-H bend
1371	1376	1374	1378	$-CH_3$ umbrella mode
1559	-	1562	1562	-H-N-C=O stretch [74]
-	1578	-	-	
1611	1609	1614	1620	-N-H deformation [74]
-	1623	-	-	
1649	1649	1647	1658	C=O stretch [74]
2937	2940	2928	2938	$-CH_3$ symmetric stretch
3016	3018	3009	3018	$-CH_3$ symmetric stretch
-	-	3045	-	$-CH_3$ symmetric stretch
3058	3069	-	-	$-CH_3$ symmetric stretch
-	-	3067	-	$-CH_3$ asymmetric stretch
3072	-	-	3072	$-CH_3$ asymmetric stretch
3083	3083	3095	-	-CH asymmetric stretch, phenyl ring
-	-	3095	-	
3110	3111	-	3107	-CH asymmetric stretch, phenyl ring
3163	3166	3159	3155	O-H stretch
3326	3328	3329	-	N-H stretch

3.5 Monitoring the Stability of the APAP II Polymorph by Raman Spectroscopy

As noted above, new interfaces in type I APAP were created by micronizing and dry coating with nanosized silica to form a stabilized type II APAP. In this section results on monitoring the stabilized phase by Raman spectroscopy as a function of time are discussed.

The spectra over a period of months for type II APAP prepared from micronized and dry-coated type I APAP are displayed in Figure 3.5 (a) and (b) show that the Raman spectral features of type II APAP discussed above remain unchanged. No molecular scale events appear to take place based on the frequencies, intensities and linewidths of the Raman lines. However, a broad scattering background superimposed on the Raman spectra similar to that seen in griseofulvin [3] is observed. The intensity of this scattering increases up to 180 days for the sample from micronized APAP and then starts to decrease as shown in the inset in Figure 3.5 (a). The scattering intensity for the sample from dry-coated APAP shown as an inset in Figure 3.5 (b) appears to saturate already after 90 days, but has been monitored so far for only 150 days.

One interpretation of the background scattering is that it is associated with scattering from defects associated with growing nanocrystallites of the stable type I phase in the matrix of the type II phase, albeit initially form in quantities that are too small to be observed in the Raman spectra but detectable by XRPD as discussed below. With time these defects anneal out as indicated by reduction or saturation in the background scattering intensity. Further studies will continue in the type II sample from nanocoated APAP to see if a reduction in background scattering intensity occurs there as well.

Although a quantitative model needs to be developed, it can be conjectured that the stabilization of the type II phase by dry coating and micronization occurs through local potential energy minima of the conformational space at the interface between APAP and nanosilica, and between surface and bulk APAP, respectively. As an interesting observation, it was noticed throughout multiple sample preparations that the formation of the metastable type II APAP phase appears to begin at the sample surface. In dry coated and micronized APAP, stabilization can occur via immobilization of the type II structure at the coating-APAP and surface-bulk interface followed by rapid crystallization of this phase throughout the film formed from the melt. Further improvement in phase II stabilization is therefore possible via APAP improved dry coating and APAP particle size reduction.

(a) (b)

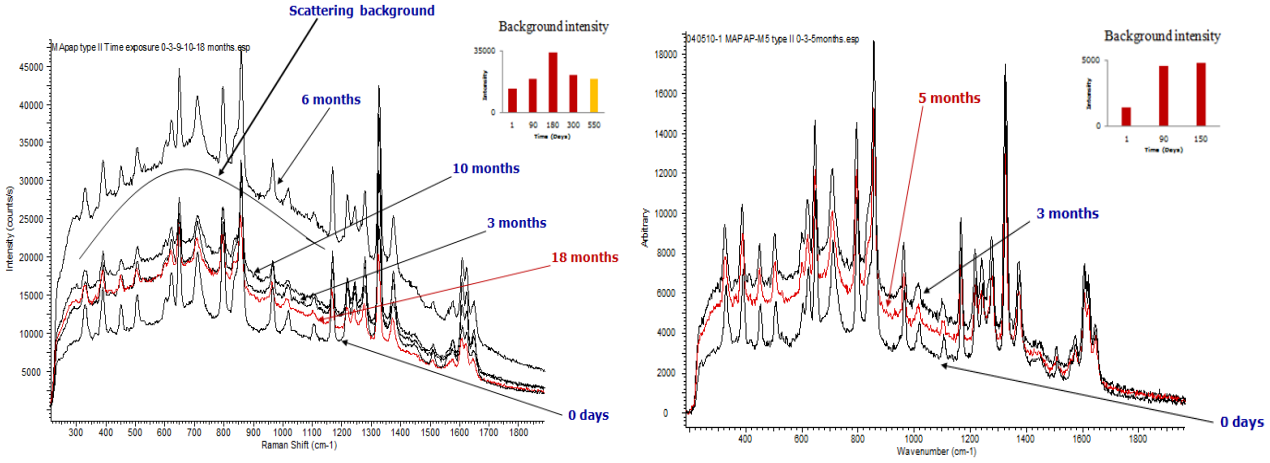

Figure 3.5 Raman spectra showing the stabilization of type II acetaminophen as a function of time for samples prepared by melt formation from: (a) Micronized type I APAP I, and (b) Nano-silica dry-coated type I APAP.

3.6 Characterization of the APAP II Polymorph by SEM, XRPD and Dissolution Measurements

3.6.1 Scanning Electron Microscopy (SEM)

The SEM studies were carried out to image the physical features of the samples since various sample types with different morphologies were employed: as-received powders, fabricated thin films, and powders from crushed films. The orthorhombic and monoclinic phase II and phase I polymorphs can be easily recognized due to differences in their corresponding crystal habit, especially when a high magnification tool, such as SEM is used. Figure 3.6 (a), (b), and (c) show representative images of as-received crystalline APAP I, as-received micronized APAP I, and nano-silica coated APAP I, respectively. Figures 3.7, 3.8, and 3.9 show SEM images of APAP II, MAPAP II, and SiO_2 APAP II, fabricated as thin films. Interestingly, APAP II in Figure 3.7 showed a large number of air pockets formed during film solidification which explains the fact that substantial absorption of water vapor through the air pockets accelerates the transition to the stable APAP type I. Air pockets were not observed for MAPAPA II and SiO_2 APAP II samples. Crystal habits of both type I APAP (monoclinic) and type II APAP (orthorhombic) were observed on the surface of nanocoated SiO_2 APAP II films shown in Figure 3.9 (indicated by arrows) consistent with XRPD results discussed below.

(a) (b) (c)

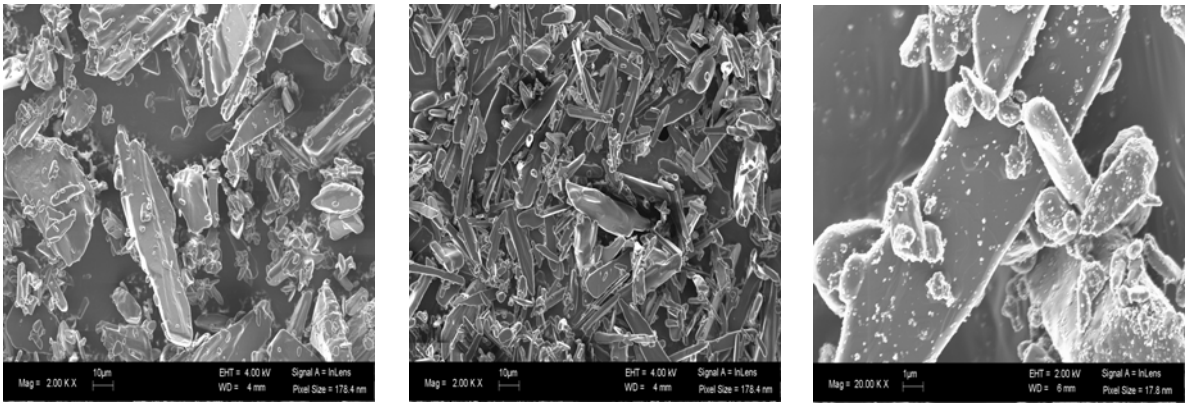

Figure 3.6 SEM images of (a) As-received crystalline APAP I, (b) As-received micronized APAP I, and (c) Nano-silica dry coated APAP I.

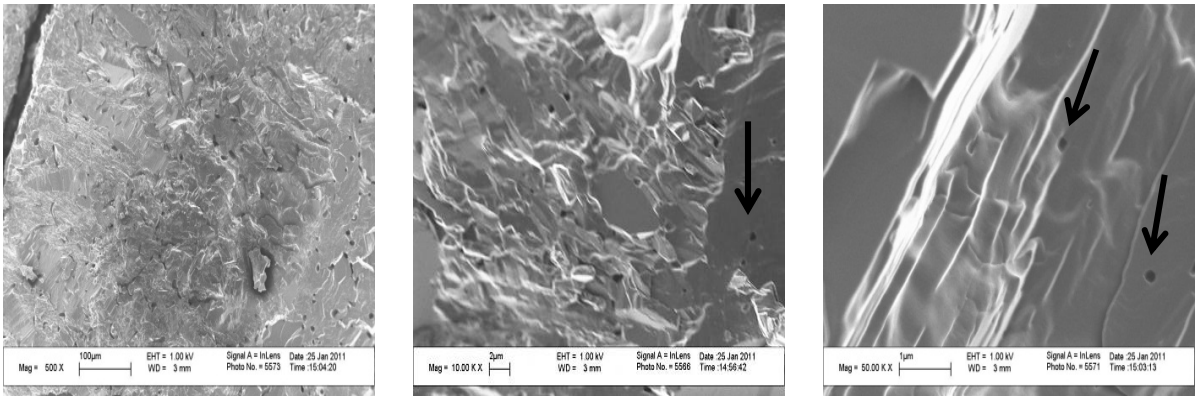

Figure 3.7 SEM images of APAP II sample fabricated as a thin film. Formed air pockets are indicated by arrows. Images are shown in order of increasing magnification.

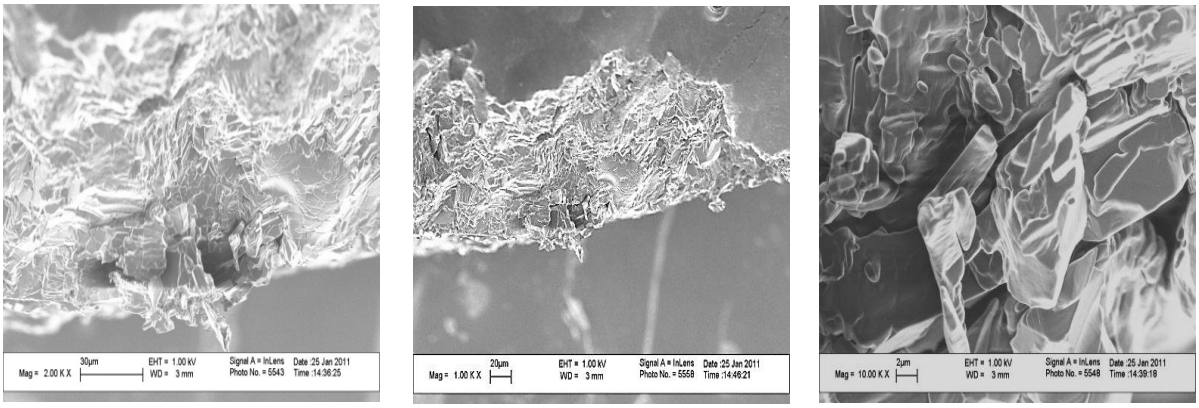

Figure 3.8 SEM images of MAPAP II sample fabricated as a thin film. Images are shown in order of increasing magnification.

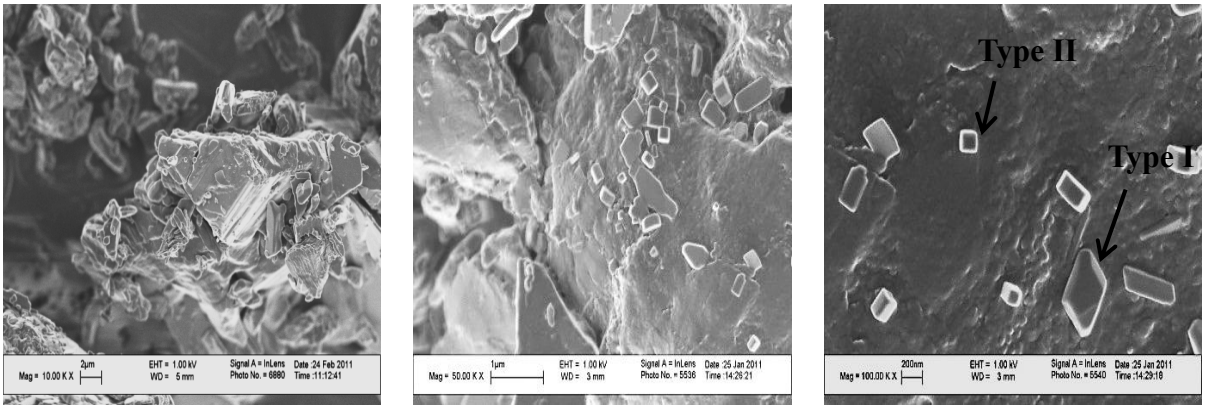

Figure 3.9 SEM images of SiO2 APAP II sample fabricated as a thin film. Presence of monoclinic and orthorhombic crystals indicated by arrows.

3.6.2 X-Ray Powder Diffraction (XRPD)

Wide-angle XRPD diffraction and scattering data obtained using CuKα radiation are shown in Figure 3.10 (a) for as-received MAPAP I and MAPAP II and Figure 3.10 (b) for dry-coated SiO_2-APAP type I and fabricated SiO_2-APAP type II samples, respectively. XRPD data for MAPAP I and II, and SiO_2-APAP I, agree with that published by Welton *et al* [75]. By contrast, the XRPD pattern for type II SiO_2-APAP is

different from that reported in the literature. After careful evaluation of the diffraction patterns and SEM images it was concluded that the XRPD pattern resulted from the presence of small quantities of type I (not detected by Raman) in the primarily type II phase sample, consistent with the SEM images discussed in section 3.6.1 above.

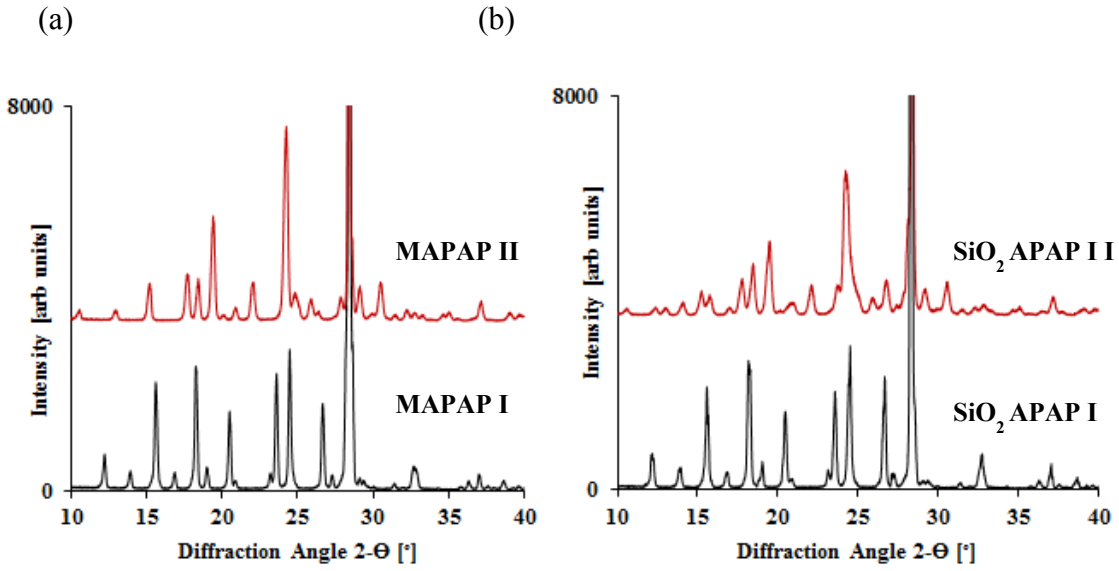

Figure 3.10 Wide-angle X-ray powder diffraction patterns of acetaminophen samples obtained using CuK_α radiation, λ =1.5406 Å, (a) MAPAP I and MAPAP II and (b) SiO_2 APAP I and SiO_2 APAP II.

3.6.3 Dissolution Profiles

By definition, "dissolution is defined as the process by which solid substances enters a solvent to yield a solution" [71]. Conventional dissolution rate (CDR) analysis was carried out to test the behavior of the stabilized type II APAP samples. Since all samples used for CDR were enclosed in gelatin capsules, the initial physical state of the sample, such as micronized size or surface coating with nano-silica, were not accounted for. Figure 3.11 (a) compares the dissolution profiles of types I and II APAP with stabilized type II APAP samples via conventional dissolution rate analysis. It can be seen that

almost complete mass release is seen in type I APAP within the first 10 minutes of analysis; this was followed by type II APAP. The two modified acetaminophen type II samples showed no improvement in dissolution rate, in fact it took almost three times as long, compared to APAP type I, for these samples to completely dissolve.

Since modified APAP type II samples are generated from micronized and silica-nanocoated APAP I, potential variations in the surface area are created which affect the conventional dissolution rate. Intrinsic dissolution rate (IDR) is characteristic of the initial physical state of the sample. IDR is described by the equation 3.1 which is also referred to as the Noyes-Withney equation [76]:

$$J = \frac{dm}{dt} \bullet \frac{1}{A} = k(C_s - C) \tag{3.1}$$

where,

dm/dt – Rate of increase of the mass of solute released per unit time t

k – Mass transfer coefficient

A – Surface area of the sample

C_s – Intrinsic solubility at sample surface

C – Concentration of solute dissolved at time t.

Equation 3.1 can be further reduced to equation 3.2 since for sink conditions $C_s >> C$,

$$J = \frac{dm}{dt} \bullet \frac{1}{A} = k(C_s) \tag{3.2}$$

Equation 3.2 indicates that the rate of dissolution may vary if the surface area of the solid is altered. There are many known surface modification techniques, such as particle size (micronization), crystalline form of a solid (polymorphs), or coating that can act as a barrier to the dissolution rate. Since both micronization and surface coating were employed here to generate type II APAP samples, intrinsic dissolution with a compressed disk of known area was employed to eliminate surface area and surface electrical charges as dissolution variables. The dissolution rate so determined can be correlated with the physical properties of the sample [76].

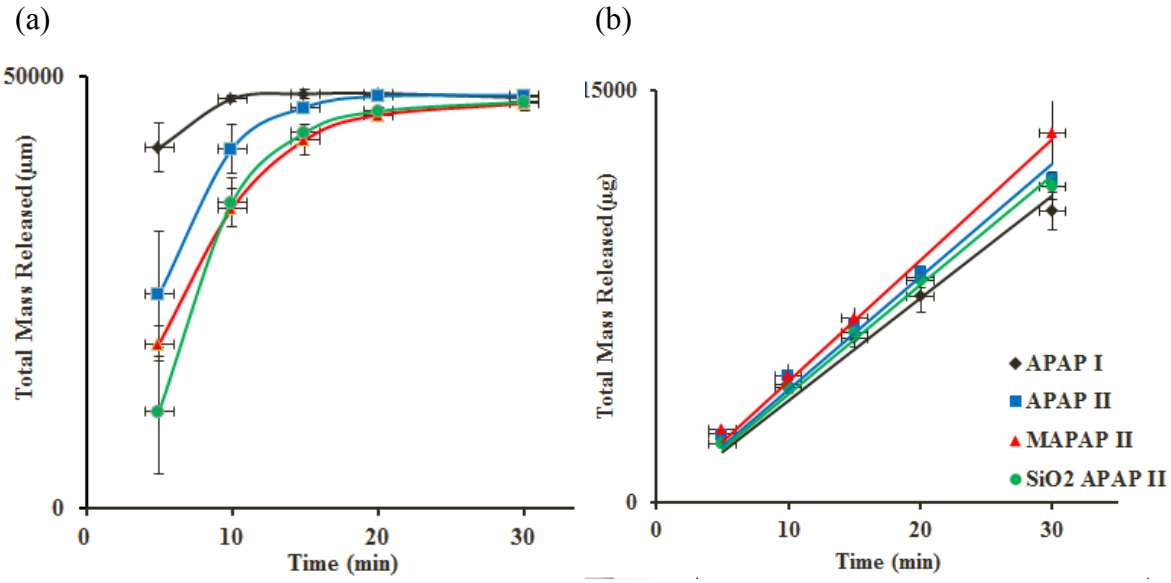

Figure 3.11 Dissolution profiles for acetaminophen samples based on (a) Conventional dissolution rate, and (b) Intrinsic dissolution rate (IDR).

Figure 3.11 (b) shows the linear IDR profile of a compressed disk under sink conditions. Both modified type II APAP (MAPAP II and SiO_2 APAP II) show increase in dissolution profile compared to results from conventional dissolution. Improved IDR for MAPAP II indicates that micronization not only promotes sample stabilization but also modifies the surface area resulting in the highest dissolution rate. From the dissolution

profile of the stable type I APAP phase, it can be concluded that it dissolves the slowest, whereas the corresponding metastable type II APAP has improved release profiles. Dry coated type II APAP also showed improvement in mass release, but the improvement relative to type I APAP is small.

3.7 Conclusions

New interfaces in type I APAP were created by micronization or by dry-coating with nanosized silica. Raman spectroscopy was utilized, among other analytical (XRPD and SEM) and dissolution techniques to, respectively, monitor the stability and determine the dissolution profile of the newly developed type II APAP phase. Raman studies conducted on the stabilized metastable type II phase as a function of time showed stability for over 18 months; however, a diffuse scattering background superimposed on the Raman spectra, observed previously in griseofulvin, developed with time and was attributed to the growth of nanosized nuclei of the stable type I polymorph in the type II phase matrix of the particles. No molecular changes at the new interfaces were, however, detected based on the Raman spectra taken as a function of time. In addition, improved dissolution profiles for the stabilized type II APAP relative to the type I phase were observed. The results obtained therefore indicate the potential of the stabilized type II APAP phase for use in pharmaceutical applications.

CHAPTER 4

IN-LINE AND OFF-LINE RAMAN SENSING OF PHARMACEUTICAL DOSAGE FORMS

1.4 Raman Spectroscopy as a Sensing Tool

Raman spectroscopy is a significant analytical tool for process understanding in the pharmaceutical industry. Process and bench top applications exist for Raman spectroscopy and can be applied for qualitative and quantitative process evaluation. Successful pharmaceutical applications include blend uniformity, reaction monitoring, solid quantification, coating monitoring and probably most significantly, crystallization monitoring and polymorph detection and analysis [3]. Significant technological development in the area of instrumentation has allowed the implementation of fiber optics, immersion and big spot size probes, and dispersive components into Raman systems, making them highly robust and versatile tools for on-line, in-line, and off-line characterization in the pharmaceutical industry [4].

Spectral imaging using Raman spectroscopy is a common tool for chemical characterization of various pharmaceutical dosage forms [8, 24, 77] including the newly developed thin polymeric films in Test Bed 2 of the NSF-Engineering Research Center [24]. Since the film's design employs small API particles, for example that of griseofulvin uniformly dispersed in a film composition, it is an excellent micro- and nano-particle based system for alternative delivery. Performance and drug behavior is based on the film's advanced functionality and ability of the active media to maintain

small particles ranging between 10 μm to 300 nm in a non-agglomerated form. This makes it possible to precisely control the release of the drug.

Low dissolution rates of poorly soluble drugs [27, 78, 79] and content uniformity of drugs administered in low doses [80-82] are the most common issues encountered by the pharmaceutical industry. In films, the small particle size in a uniformly dispersed configuration can significantly affect some of the commonly encountered problems by potentially enhancing the dissolution rate of poorly soluble drugs, in particular griseofulvin, and the content uniformity of drugs administered in low doses.

Since the crystalline state of any API affects its use in pharmaceutical applications as a drug processed into pills or capsules for pharmaceutical applications, it is necessary to develop effective, fast, and non-destructive methods that would allow elimination of crystalline defects and potential polymorph formation [6-8]. Implementing Raman and NIR spectroscopic techniques as on-line and in-line sensing tools, provides molecular level understanding and monitoring of solid-state behavior, uniformity, and particle size distribution in a dosage form.

In this Chapter, Raman imaging provides the spatial distribution of micro- and nano-sized griseofulvin in the polymeric films and explores the possibility for developing innovative dissolution methods based on drug allocation on the film's surface [24]. Various film compositions were prepared and analyzed by Raman imaging [39]. In addition, complementary Raman and NIR imaging (by Jarez, Zarow *et al* [24]) was performed on a set of four films and will be discussed below.

Raman spectroscopy is also used to demonstrate the feasibility of in-line Raman spectroscopy to dynamically monitor the crystallinity and particle size of griseofulvin in

stable nanosuspensions that are being developed (Bhakay, to be published). The behavior of griseofulvin nanosuspensions will be presented and discussed in sections below.

4.2 Chemical Mapping and Imaging

Applications of vibrational spectroscopy, Raman and NIR in particular, have gained significant recognition in the pharmaceutical community as techniques for analyzing solid dosage formulations [72, 83-86]. The concept of chemical imaging is relatively new as it was developed and applied to pharmaceutical samples in the mid-1990s [87]. It was quickly realized that this techniques can offer much needed understanding and detail information to solve problems related to product development. Both Raman and NIR chemical imaging (CI) provide chemical and physical information at different scales of scrutiny [24]. The presence of specific spectral bands can be used to identify components of the formulation, their spatial distribution, particle sizes, and most importantly their crystallinity and polymorphic states. The main advantage of using vibrational techniques is characterization of dosage forms on an as-received basis with no sample preparation. NIR and Raman spectroscopy, given their complementary origins, result in characteristic vibrational spectral features. NIR spectra show broad second-order bands due to combinations and overtones of fundamental vibrations which sometimes are difficult to assign to the individual functional groups [88]. On the contrary, Raman-active vibrations above 200 cm^{-1} are associated with narrower first-order spectral lines resulting from interatomic bond vibrations [6]. In the solid-state, the line-shapes and line-widths, and splittings of these narrow bands can also provide important information on the crystallinity of the investigated material [23].

Among the advantages of using Raman CI for characterization of formulations during pharmaceutical development and manufacturing processes are: chemical visualization of spatially resolved components of a sample mixture at a microscopic scale, visualization of impurities and degradants generated during processing, determination and quantification of different physical forms, and low limits of detection per mapped area (better than 0.025 %) [8, 89, 90]. The main disadvantage of Raman CI is the long acquisition time necessary compared to NIR-CI, and if the mapped area is relatively small, a large number of maps are required to be representative of the bulk sample.

Principle of Raman Imaging: Raman CI can be acquired using point and line mapping, or global illumination. Independent of the mapping technique used, the collected data result in generation of the same chemical image, also called hyperspectral data cube [91] presented in Figure 4.1 (a). This 3D block contains two types of data: spatial, composed of x and y coordinates and spectral, composed of wavelength and intensity. Due to the detector design, the 3D cube results, however, in a 2D representation.

During point mapping, the sample area is selected first using the microscope to focus on the specific detail or location on the surface. The area is then divided into mapping points and the hyperspectral data cube is generated by acquiring the entire Raman spectrum (or specific range) at each point for all points as shown in Figure 4.1 (b). The line mapping is obtained in similar fashion, except the laser source is stretched into a line and results in timely completion of the map [92] comparing to point mapping [Figure 4.1 (c)]. When a global illumination technique is used, the selected sample area is exposed to defocused laser radiation allowing coverage of a much larger area as shown in

Figure 4.1 (d). The sample response is obtained at a specific wavelength simultaneously for the entire illuminated area. Since point and line techniques collect high quality Raman spectra, and are not wavelength specific, they generate a wealth of chemical information from the mapped sample area. Global illumination, on the other hand, is a much faster technique but may result in poor chemical information since the emphasis is on the spatial information.

(a)

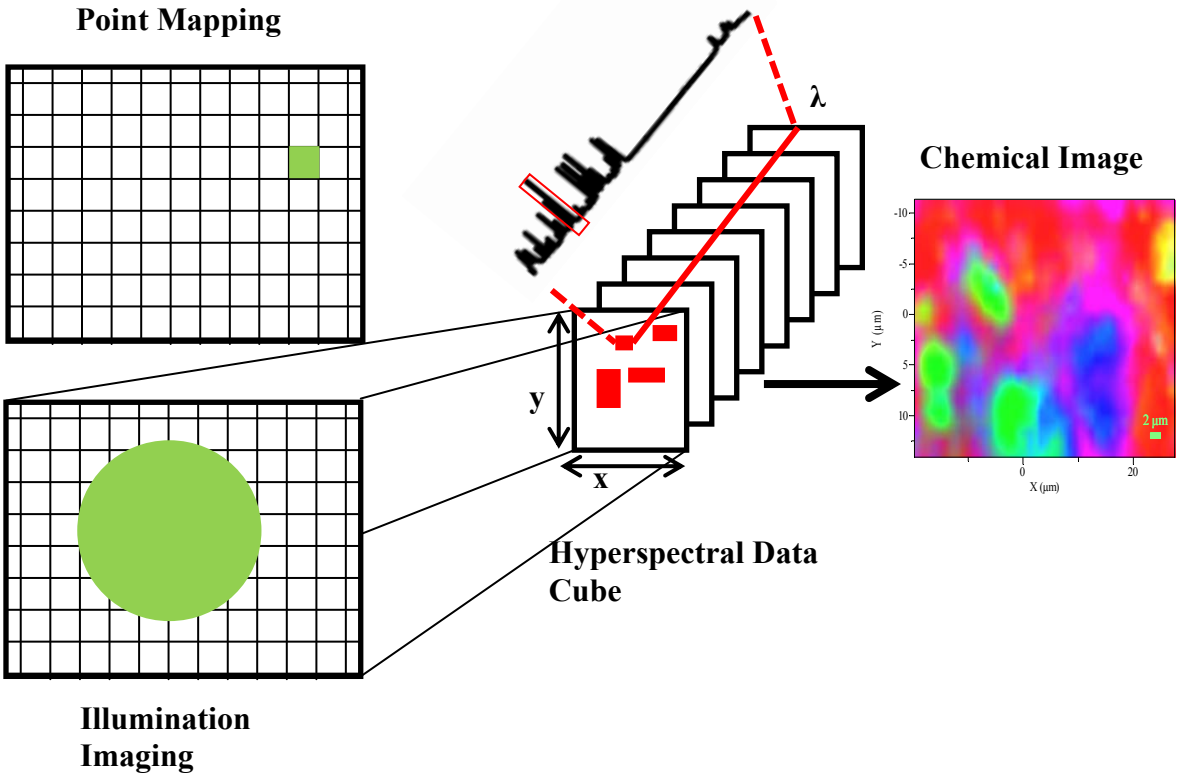

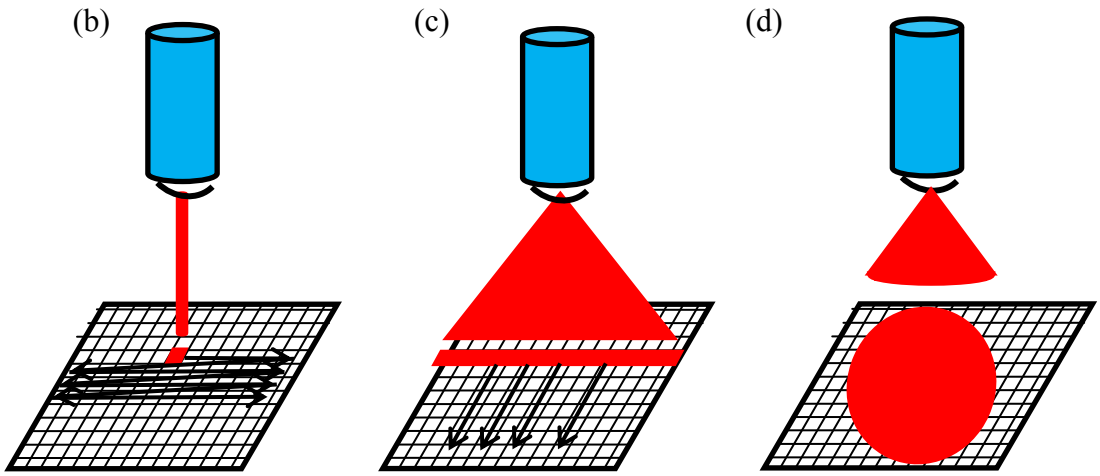

Figure 4.1 Schematic representations of hyperspectral cube and approaches to chemical imaging: (a) Methods of acquiring the hyperspectral cube; (b) Point mapping; (c) Line mapping; and (d) Illumination.

To visually represent a hyperspectral data cube as a chemical image, various statistical tools need to be implemented. It should be remembered that a hyperspectral data cube represents a set of raw data and can become a chemical image that shows intensity variation of these raw data only upon statistical processing. The data processing tools used in this study are described in section 4.3.

4.3 Analysis of the Hyperspectral Data Cube

During acquisition of a spectral image, a very large amount of data is collected. For example, a Raman hyperspectral data cube with spatial dimensions of 20 μm x 20 μm and 120 x 120 pixels can result in 14400 spectra, each with approximately 3000 data points. To extract the relevant chemical, physical and spatial information from such a dense dataset, various statistical algorithms need to be employed. This practice has led to the development of a new chemical field that is also known as chemometrics [6]. The

majority of commonly used chemometrics techniques rely on univariate and multivariate classification of the data. For a univariate approach, only a specific wavenumber of each component is selected to create a chemical image, whereas multivariate analyses take into account all spectral information contained in the data cube and employ techniques like Principal Component Analysis (PCA) [93], Partial Least Squares (PLS) [94], or Direct Classical Least Square (DCLS) to produce a chemical image.

Typical steps in a data analysis procedure consist of unfolding a three-dimensional data cube into a two-dimensional representation, preprocessing, classification of data, and image processing [77]. Data preprocessing is usually performed to remove the non-chemical biases that arise form scattering effects due to surface roughness, particle size, random noise, or optical effects. These techniques include mathematical methods such as:

- Standard Normal Variate (SNV) – identical to auto-scaling, reduces slope variation from spectrum to spectrum. It results in a similar background in all spectra and therefore enhances the differences due to band intensities
- Smoothing – improved S/N ratio by averaging signal over many spectra using Fast Fourier transform (FFT) or Savitsky-Golay methods
- Mean-centering – subtracting the mean from all spectral data resulting in the shift of the data towards the mean
- Normalization – results in similar scale of the intensity range for all spectra.
- Baseline Flattening – polynomial functions are used to fit a baseline followed by its subtraction from the spectral baseline
- Derivatives – 1^{st} and 2^{nd} are most commonly used. They eliminate slopes or

curved background in spectra due to fluorescence, structural defects, or Rayleigh wings and resolve peak overlaps [6].

After data preprocessing, qualitative and/or quantitative analysis is performed. Among the most recognized processing methods are PCA, PLS, and DCLS, which are explained briefly below.

In case of PCA, a set of orthogonal representations is found for the analyzed data cube by expressing the data matrix (M) as the product of two other matrices – the scores matrix T and the transpose of the loadings matrix L as in the following equation 4.1:

$$X = TL^T \tag{4.1}$$

PCA gives information on the most variance in the observed variables and is used as a prediction or criterion of a variable in subsequent analyses [91]. While PCA calculates loadings independently of the concentrations of the components, in PLS spectra are highly correlated to the concentrations resulting in loadings that account for the maximum variance in both the spectra and the concentrations [6]. PLS classification can be also calculated using pure reference spectra to extract the distribution map. This technique is called PLS discriminant analysis (PLS-DA). Another chemometrics technique is DLCS, also known as Ordinary Least-Square algorithm (OLS). DLCS finds linear combination of data from pure components and creates a combination that most closely matches the original data providing quantitative estimates of the concentrations [95].

In the research presented, polymeric films 1-3 and 5 were analyzed by PLS-DA and the results are explained in the following section. All of the remaining films were analyzed using a DCLS algorithm. Particle size calibration was performed using the univariate method.

4.4 Experimental Details

Griseofulvin, a poorly soluble drug, was used as a model active pharmaceutical ingredient (API) in micronized and nanosized forms. The total of nine films was investigated in this study to determine the distribution of the embedded griseofulvin in the polymeric matrix. Hydroxypropyl methylcellulose (HPMC) was selected as the film-forming excipient for all films. In some cases, sodium dodecyl sulfate (SDS) and glycerol (GLY) were added as surfactant to the HPMC matrix, as indicated in Table 4.1. Micronized griseofulvin and HPMC were purchased form Sigma-Aldrich Corporation (Milwaukee, WI), SDS was purchased from Fisher Scientific (Fair Lawn, NJ), and GLY was supplied by J. T. Baker Inc (Phillipsburg, NJ). Films labelled as 6, 7, 8 and 9 were prepared from griseofulvin nano-suspensions with particle size of approximately 260 nm. Films labelled as 12C, 1, 2, 3, and 5 were prepared form micronized griseofulvin with a particle size of 10 μm.

4.4.1 Preparation of Griseofulvin Films and Nanosupensions

Films 1, 2, 3, and 5: Blends of micronized API and HPMC were prepared by first dispersing the two components together in hot water (80^{o}C), followed by stirring for 12 hours and drying at room temperature. The films produced have a thickness on the order of 100 μm. A total of five film batches were prepared but only four films were selected

for this study as indicated in Table 4.1 and analyzed by Raman mapping and NIR-CI. Since only films with different drug concentrations were considered, film 4 was not studied because it had the same concentration as film 2. Every sample was analyzed by the two imaging methods, Raman and NIR spectroscopy. However, the instrumental setup precludes the possibility of analyzing the exact same region of the film by the two methods.

Films 12C: Prepared as films 1, 2, 3, and 5 above with addition of different SDS and GLY amounts during the dispersion of the blends as indicated in Table 4.1.

Films 6, 7, 8, and 9: Blends were prepared in the same fashion as for film 12C and milled using a MicroCer media mill from Netzsch Fine Particle Technology (Exton, PA) with 400 μm zirconia beads and milling speed of 3200 rpm to generate sub-micron particles. Upon media milling completion, t = 64 minutes, stable griseofulvin nanosuspensions were obtained and used to cast films dried at various temperature conditions as indicated in Table 4.1. Particle size analysis at t = 64 minutes was performed with Beckman Coulter LS13320 laser diffraction particle size analyzer from Beckman Coulter (Brea, CA) , and determined to be in a range of 240 nm (D90).

Griseofulvin Nanosuspension: For in-line particle size characterization and crystallinity study of griseofulvin nanosuspension, new blends were produced with the following concentration: 8.84% (w/w) griseofulvin, 2.21% (w/w) HPMC, and 0.44% (w/w) SDS; and media milled using same technique as in case of films 6 through 9. During media milling, periodical sampling of the suspension was performed at t = 1, 2, 4, ….64 minutes. Laser diffraction spectrometry was used to analyze the particle size of the collected samples. Results of particle size analyses are presented in Table 4.2. Solid-state

analysis of griseofulvin nanosuspensions was performed by collection of static and dynamic (suspension was magnetically stirred) Raman spectra recorded with a fiber optic Raman spectrometer.

Table 4.1 Prepared Compositions of Griseofulvin Films

Film Name	Griseofulvin (%)	HPMC (%)	SDS (%)	GLY (%)	Drying Temperature (°C)
1	57.00	43.00	-	-	25.00
2	50.00	50.00	-	-	25.00
3	44.00	56.00	-	-	25.00
5	36.40	63.60	-	-	25.00
12C	9.30	69.70	0.02	20.90	25.00
6	49.14	29.66	2.00	18.76	25.00
7	37.63	51.97	1.87	8.51	25.00
8	37.63	51.97	1.87	8.51	50.00
9	37.63	51.97	1.87	8.51	42.00

Table 4.2 Particle Sizes of Sampled Griesofulvin Nanosuspensions

Milling Time (min)	Particle Size [D90 (μm)]	Particle Size [Mean (μm)]
0.00	7.29	3.96
1.00	6.16	3.18
2.00	5.71	2.86
4.00	4.71	2.07
8.00	1.63	0.92
16.00	0.73	0.48
32.00	0.48	0.26
48.00	0.31	0.19
64.00	0.24	0.16

4.4.2 NIR Chemical Imaging

The near infrared hyperspectral images were obtained by Jerez at the University of Puerto Rico, Mayaguez and acquired using a SyNIRgi (Spectral Dimensions Inc., Olney, MD) instrument. The images were obtained in the diffuse reflectance mode with a spatial resolution of 320 X 256 pixels. A 10 μm per pixel objective was used to analyze a film area of approximately 3.2 x 2.6 mm. The spectra were obtained with 5 scans in a spectral range of 1200-2400 nm. Two different areas within the same gel strip film were analyzed.

4.4.3 Raman Chemical Imaging

Films 1 - 3, 5 and 6 - 9: Raman mapping spectra were collected using a Jobin Yvon/Horiba LabRAM micro-Raman spectrometer, with 632.81 nm He/Ne laser excitation and a 10x objective. For higher magnification objectives, such as 50x and

100x, significant de-focusing was observed on the sample surface due to heating, which precluded mapping experiments. The Raman spectra were recorded in the 800-1650 cm^{-1} range. The films were analyzed "as is," without sample preparation or modification, and no sample damage was observed during the experiment. The data collected were analyzed using the Malvern NIR Instrument's Isys software to generate chemical images.

For films 1 - 3 and 5 a typical chemical map consisted of 30 x 30 pixels, with a step size of 0.3 μm. The mapping was performed by acquiring Raman spectra from thirty points in the x direction and 10 μm distance and repeating the same for 10 μm in the y direction. Since the laser was moved by 0.3 μm each time, a new Raman spectrum was acquired, which resulted in high sampling frequency along both directions giving higher spectral content and therefore more accurate information on chemical behavior and borders of particle domains. This relatively high sampling frequency at the laser spot size results in sampling of 10% of new area at each step size, giving more thorough chemical evaluation of the film components. Each spectrum was acquired for 3 seconds at each pixel or stage position resulting in a total acquisition time of 1 hour and map size of approximately 10 μm x 10 μm. Achievable laser spot size and spatial resolution of the micro-Raman spectrometer were calculated to be 3 μm and 1.5 μm respectively and were calculated based on lateral spot size (1.22λ/numerical aperture), and spatial resolution = 0.61λ/numerical aperture) [96]. Four maps were recorded for films 1-3 and 5. Films 3 and 5 were subsequently re-analyzed resulting in an additional five maps for films 3 and 5.

Chemical maps for films 6 - 9 consisted of 30 x 30 pixels with step size of 1 μm. Raman spectra were acquired from thirty points in the x direction and 30 μm distance and repeating the same for 30 μm in the y direction resulting in the 30 μm x 30 μm mapped

area. Single Raman spectrum acquisition time and total mapping acquisition time were as above.

For film 12C, chemical maps were performed with a Jobin Yvon/Horiba LabRAM Aramis confocal Raman microscope using 632.8 nm He/Ne laser excitation and a 100x objective with a spatial resolution of 1 μm. Two maps form independent locations on the film were recorded. Location 1 map comprised of 60 x 60 pixels with 0.5 μm step size resulting in the approximately 30 μm x 30 μm mapped area. Location 2 map consisted of 90 x 60 pixels with 0.5 μm step size resulting in the approximately 30 μm x 45 μm mapped area.

4.4.4 Raman Instrumentation for Solid-State and Particle Sizes Sensing

Solid-State Raman Spectra of Griseofulvin Nanosuspensions: An EZRaman LE Raman Analyzer System from Enwave Optronics with a HRP 8 high throughput fiber probe and a 250 mW 785 nm laser focused at a working distance of 6 mm was used for simulated in-line measurements of crystallinity of griseofulvin nanosuspensions. Raman spectra were collected with 10 seconds acquisition time each.

Griseofulvin Particles Sizes in Nanosuspensions: EZRaman LE Raman Analyzer System coupled to MicroVievew adapter with a 4x objectives and 15 μm spot size; and Mesophotonics SE1000 Raman spectrometer with a 300 mW power 785 nm excitation laser and 130 μm diameter spot size were used to measure the particle sizes of griseofulvin in nanosuspensions. Each sample measurement corresponded to an average of 5 scans, each 10 seconds long, totaling 50 seconds in scanning time.

4.4.5 Data Treatment

Data Treatment for NIR Spectra (Films 1-3 and 5): The data were analyzed using the Malvern NIR Instrument's Isys vresion 5.0.0.14 software. The logarithm, $\log_{10}(1/R)$, was first applied to the data cube to convert the spectra to absorbance units. Bad pixels were replaced by the average response of the neighboring pixels. A low-pass Fourier filter was applied to reduce spectral noise caused by the use of transflectance for a semi-transparent matrix. The spectra were normalized using the Standard Normal Variate and Savitzky-Golay second derivative (filter order 3, filter width 9) [24].

Data Treatment for Raman Maps: The data were analyzed using the Malvern NIR Instrument's Isys version 5.0.0.14 software. Raman spectra were collected in the 850 to 1650 cm^{-1} frequency range. A spatial mask was initially applied in order to eliminate background pixels, followed by a low pass filter, baseline correction, normal standard variate (SNV) transformation and Savitzky-Golay second derivative (filter order 3, filter width 13). The resulting spectra were obtained from 850 to 1650 cm^{-1} frequency range. Partial least squares discriminant analysis (PLS-DA) was performed to provide a chemical image based on the distribution of the drug throughout the film. For films 6 - 9, same data pretreatment was applied as above followed by univariate analysis of the 820 cm^{-1}Raman line intensity for the solid-state characterization of the films produced from griseofulvin nanosuspensions. For film 12C, data processing was performed by using Jobin Yvon/Horiba LabSPEC 5 version 5.42.18 software. The collected map was normalized and analyzed using the Direct Classical Least Square (DCLS) technique.

Data Treatment for In-Line Particle Size Raman Spectra: Data collected were analyzed using Mesophotonics SE1000 Raman instrument's ACD/Labs SpecManager

version 12.01 software. All Raman spectra were normalized and smoothed by a Savitzky-Golay filter (order 5, width 11) and analyzed using the univariate method by monitoring 822 cm^{-1} and 1706 cm^{-1} Raman lines intensities at each sampling interval. The Raman line at 822 cm^{-1} is known to be attributed to cyclohexanone ring stretching vibrations and disappears with decrease in crystallinity of the sample as reported by Zarow *et al* [23].

4.5 Sensing of Films and Nanosuspensions

4.5.1 Films

The overall objective of this chapter is to use results of off-line Raman spectroscopic characterization, such as those described in Chapters 2 and 3, to help interpret on-line Raman monitoring performed in the test-beds of the ERC. Off-line Raman mapping was performed for griseofulvin films of various concentrations and analyzed for particle distribution, quantification and defect formation. In addition, complementary NIR and Raman chemical analyses were performed for some of the films [24] to investigate the presence of agglomerates and the solid-state morphology of embedded particles. The goal of off-line imaging is to provide input to in-line Raman data interpretation particularly regarding the homogeneity of dosage forms in pharmaceutical films and tablets. Previous studies have used NIR-CI for polymeric films containing dissolved API [97] whereas in this study the drug particles are suspended in the matrix. Partial Least Squares Discriminant Analysis (PLS-DA) and Direct Classical Least Square (DCLS) are performed to develop a chemical image based on the spatial distribution of the drug throughout the film for various films [24].

a) Film 12C

Distribution of griseofulvin particles embedded in a pharmaceutical film is crucial to determining the optimal preparation conditions and monitoring any morphological changes during film fabrication. Figures 4.2 (a) and (b) represent Raman chemical maps and Raman chemical images resulting from data processing of two independently mapped locations on film 12C with 9.30 wt% API, 69.7 wt% HPMC, 20.9 wt% GLY and 0.02 wt% SDS respectively. Chemical images correspond mostly to the API particles, shown in light blue or green, and HPMC shown in red. The shades of blue/green indicate API scattering intensity which changes due to the topology of the film and uneven HPMC coverage. The mapping data indicate no chemical or structural changes of the API and shows drug agglomerations into larger particle regions from 5 to 10 μm. There are also smaller particles of size less than 5 μm.

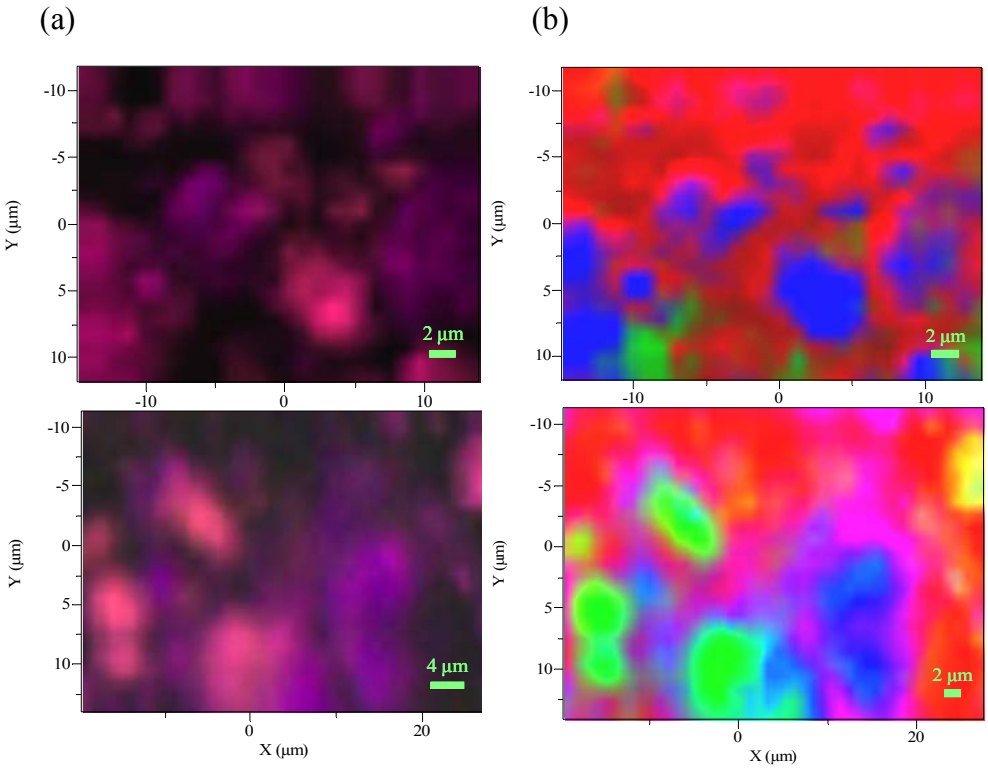

Figure 4.2 Raman chemical analysis of film 12C: (a) Raman chemical maps of griseofulvin distribution for location 1 (top) and 2 (bottom) on the film, and (b) Raman chemical images developed for location 1 and 2 using DCLS analysis.

b) Films 1, 2, 3, and 5

NIR Mapping – Due to the large overlap between NIR bands for griseofulvin and HPMC, second derivative spectra were obtained and the absorption band at 2080 nm was used since it represents an important change of slope in the spectrum of griseofulvin [24]. Figure 4.3 shows resulting NIR chemical images and histograms of griseofulvin films. Films 1, 3 and 5 show differences in the variation of the distribution in each histogram, associated with differences in the distribution of HPMC and griseofulvin in the film. The binary image analysis, not shown here, confirmed the absence of large clusters in the film. However, in films 1 and 4 the particles are not as widely dispersed as in the other films. The particles are widely dispersed when the area covered is higher, and more aggregated when the area covered is reduced [24].

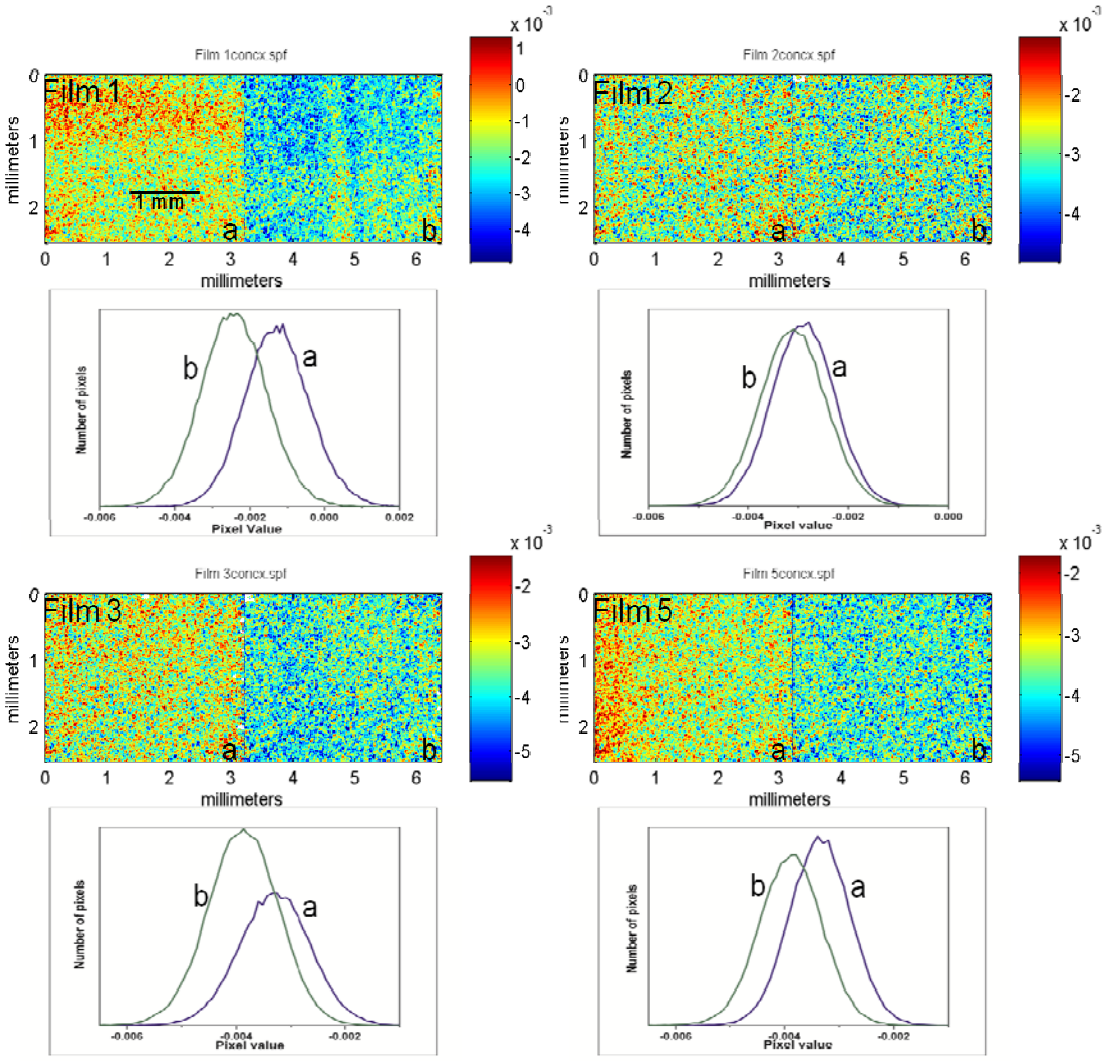

Figure 4.3 Near IR chemical images and histograms for the different components within the films 1, 2, 3, and 5 at 2080 nm [24].

Raman Mapping - Figure 4.4 shows Raman spectra of individual film components, HPMC, griseofulvin, and composite HPMC-griseofulvin film. The boxed region indicates the spectral region with the strong 1620 cm^{-1} griseofulvin band [23]. The HPMC-griseofulvin film spectra were obtained in spectral regions, as in film 3, where the 1620 cm^{-1} band intensity is high and HPMC lines are not interfering. Pure HPMC and griseofulvin spectra from film 3 were used to create a reference library based on partial

least squares discriminant analysis PLS-DA. The image scores are based on the degree of association of each pixel with the reference library; higher scores indicate a spectrum more similar to the loading. A red-green (RG) color-coded composite image was developed to show the localization of two components simultaneously. Figure 4.5 (a) shows the false color spatial mapping for the predicted distribution of API (red) and HPMC (green) in the four films. The corresponding image represents a sample area of about 100 μm^2 hence providing a high resolution view of the distribution of the API particles in a smaller area. Higher spatial resolution is therefore obtained by micro-Raman mapping, and this method could also eventually detect the presence of inhomogeneity, impurities and/or API polymorphs in the films [98]. The spectra obtained were compared to those from a prior study where the structural disorder induced by cryogenic milling and by heating to the amorphous phase in the active pharmaceutical ingredient were studied using Raman spectroscopy, X-ray powder diffraction (XRPD), and fluorescence spectroscopy [23]. For griseofulvin films, Raman mapping analysis did not show any solid-state transition, such as amorphization upon film formation, as determined by the enhanced intensity of a characteristic Raman line for crystalline griseofulvin at 820 cm^{-1} reported by Zarow *et al* [23].

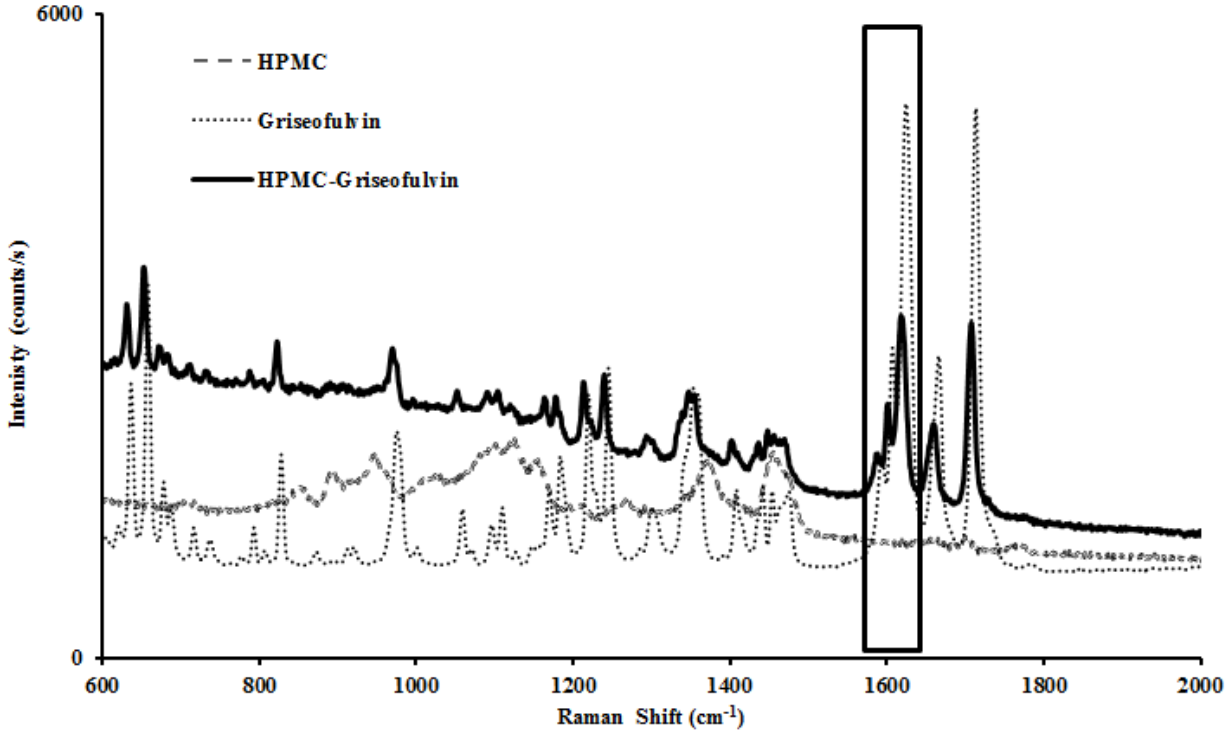

Figure 4.4 Raman spectra of griseofulvin, HPMC, and HPMC-griseofulvin. The boxed region shows lines associated only with griseofulvin.

PLS-DA provided an assessment of drug distribution throughout the films. Table 4.3 summarizes the results showing that the predicted values agree closely with the nominal concentration values, except for film 2. However, the small area analyzed (≈ 100 μm^2) might not be representative of the concentration in the film. Therefore, five different areas of films 1 and 5 were further analyzed. Table 4.4 shows that the average value of five measurements is close to the nominal value of the film, however, area 4 in film 1 and area 2 in film 5 show significant differences between predicted and nominal concentrations. The results obtained indicate that the sampling error resulting from the small area analyzed is likely the main reason for the difference in the prediction.

Table 4.3 PLS-DA Concentration Prediction of Griseofulvin and HPMC in Films 1, 2, 3, and 5

	Film 1	**Film 2**	**Film 3**	**Film 5**
API Nominal	57.0%	50.0%	44.4%	36.4%
API Predicted	50.0%	62.0%	44.0%	34.0%

Table 4.4 PLS-DA Concentration Prediction of Griseofulvin in Analyzed Areas of Films 1 and 5

	Predicted Value of Griseofulvin					**Average**
	Area 1	**Area 2**	**Area 3**	**Area 4**	**Area 5**	
Film 1	59.0%	55.0%	59.0%	48.0%	54.0%	55.0%
Film 2	33.0%	56.0%	36.0%	36.0%	31.0%	38.0%

Figure 4.5 (b) shows the histograms based on PLS-DA scores for the different films. The histograms show a very low number of areas with high scores. The high scores are indicative of high concentrations of HPMC or griseofulvin. However, a large number of areas are observed where the scores range from 0.4 – 0.6 indicating a lower concentration of the griseofulvin or polymer. These intermediate concentration values indicate that the Raman method is detecting both griseofulvin and polymer, and that these are mixed throughout the film at a fine scale. Raman spectra acquired through high frequency sampling of the 10 x 10 μm mapping area provided a thorough chemical evaluation. This type of information is unique to hyperspectral images and is not available from spectra recorded from sample averaging or integrating spectrometers.

c) Films 6, 7, 8, and 9

This set of films consisted of films manufactured using various concentrations of griseofulvin nanosuspensions and dried at different temperatures. It was of great importance to study the effect of film formation on nanosized drug in suspensions and to monitor crystallinity and particle size distribution in resulting thin films. Figure 4.6 shows black-white (BW) color-coded composite images developed by monitoring the 822 cm^{-1} griseofulvin Raman line using univariate analysis where black-white colors correspond to low and high intensity of the line, respectively. For griseofulvin films manufactured from nanosuspensions, Raman mapping analysis, at a given resolution, did not show any solid-state transition, as determined by the presence of the characteristic Raman line at 820 cm^{-1} [23]. At this early stage of analysis, it was concluded that the chemical composition of the drug embedded in the films was not affected by the manufacturing conditions. Distribution and size of griseofulvin particles could not be determined at this time since the Raman chemical images showed no individual particles or agglomerations throughout the mapped areas shown in Figure 4.6.

(a) (b)

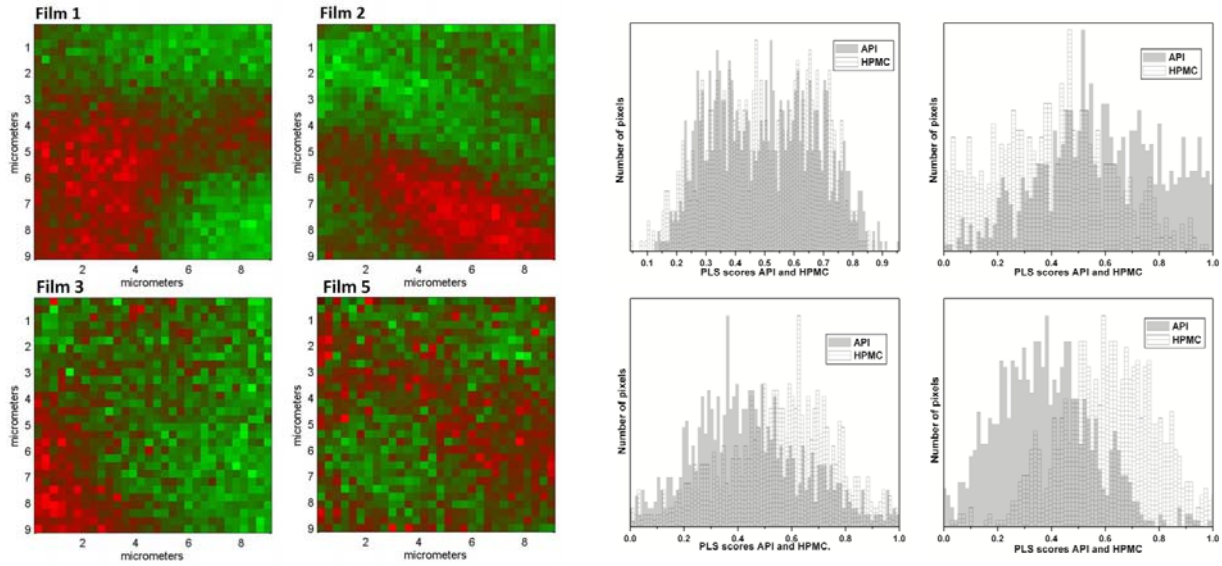

Figure 4.5 (a) Red-Green (RG) color-coded Raman images where red represents the distribution of the API, griseofulvin and green that of the excipient, HPMC; and (b) Histograms providing quantitative descriptions of griseofulvin and HPMC contents for films 1, 2, 3, and 5.

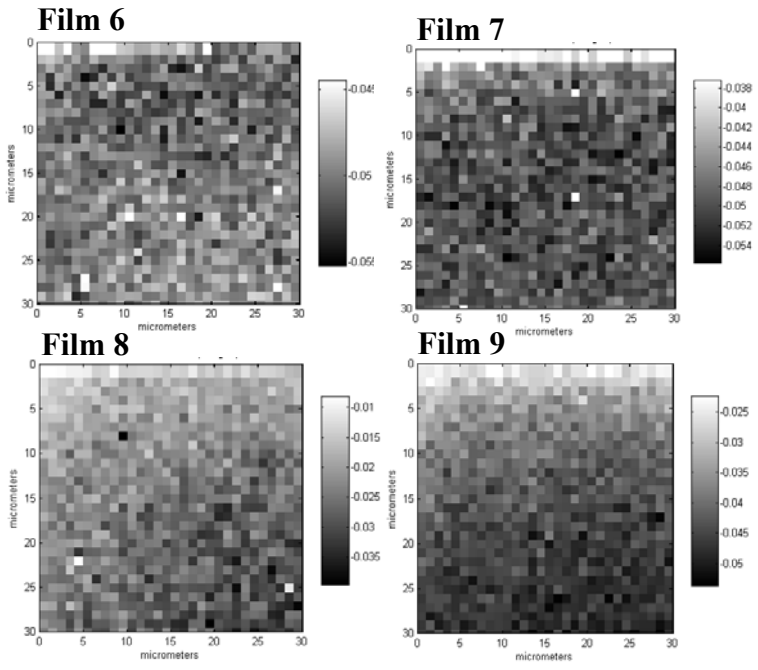

Figure 4.6 Black (low intensity of the 820 cm^{-1} Raman line) - White (high intensity of 820 cm^{-1} Raman line) color-coded Raman images of griseofulvin nanosuspension films 6 through 9 processed with the univariate method.

4.5.2 Nanosuspensions

The effect of media milling on newly developed stable suspension of griseofulvin of 8.8 wt% nano-sized griseofulvin and HPC-GLY-SDS composites was studied. The stable suspension at various griseofulvin concentrations was later used to manufacture thin films by casting. The structural and chemical stability of nanosized drug particles in formulated suspensions were studied. Media milling was used to increase the bioavailability of this poorly soluble drug by decreasing its particle size. The previous study of cryomilled griseofulvin with particle size of the order of 300 nm, resulted in formation of structural disorder and loss of crystallinity on processing [23]. Since media milling generated nanosized griseofulvin in a similar size range of approximately 240 nm, it was critical to study the effect of media milling on the solid state properties of griseofulvin. The structure of the nanosized particles were determined based on the characteristic Raman lines for crystalline griseofulvin in the 500 to 850 cm^{-1} spectral range [23]. An initial study of dynamic and static Raman spectra, collected by a fiber optic Raman spectrometer to simulate in-line monitoring of the solid-state of the drug in suspension, showed no indication of an amorphous component in nanosized griseofulvin in the stable suspension (Figure 4.7).

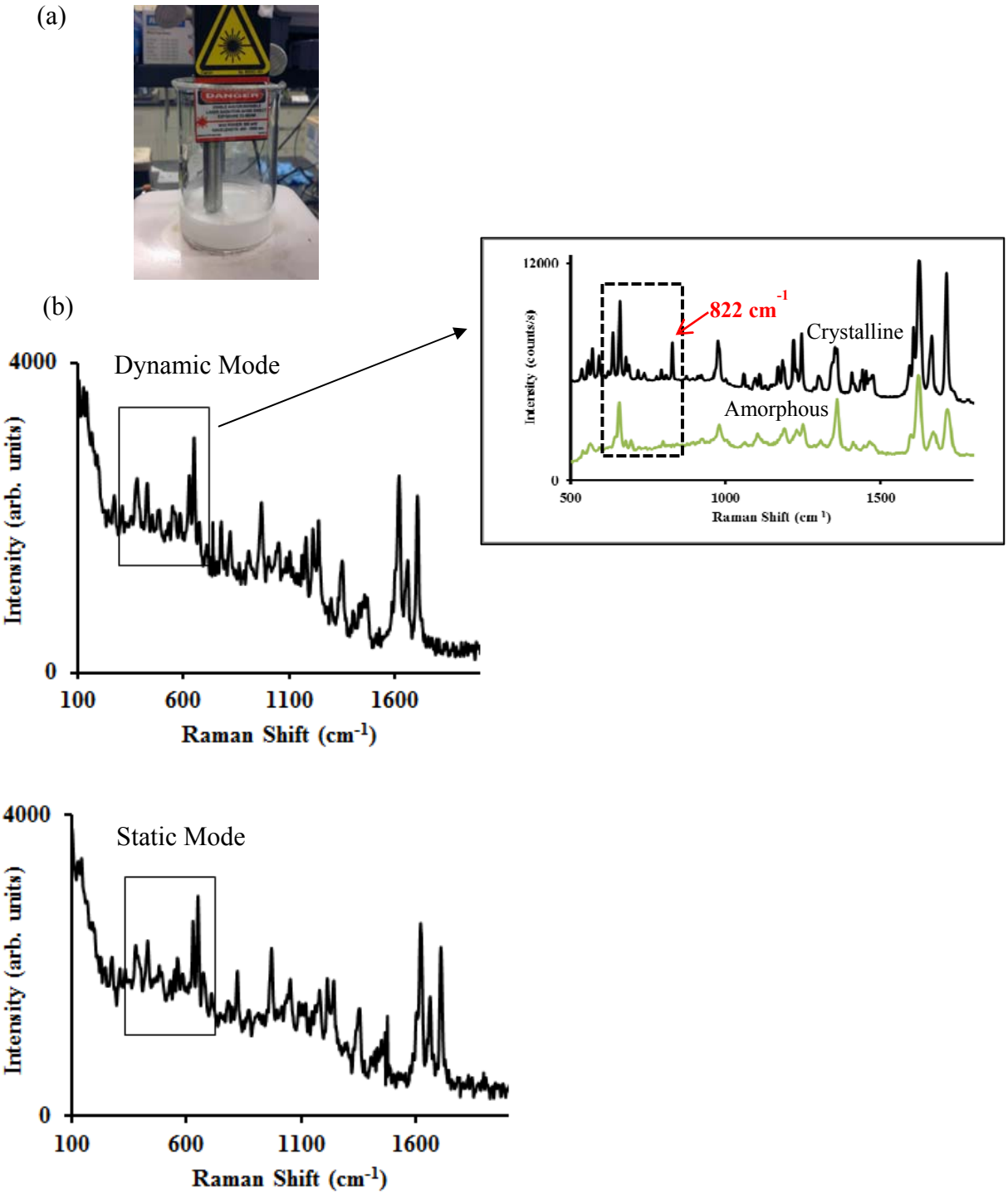

Figure 4.7 Simulation of on-line crystallinity monitoring of griseofulvin nanosuspension: (a) Photograph showing set up for the acquisition of dynamic and static Raman spectra with a fiber optic Raman spectrometer, and (b) Recorded Raman spectra in dynamic (top) and static (bottom) modes. Boxed region shows vibrational spectral differences between amorphous and crystalline griseofulvin.

The dependence of Raman scattering on particle size has been widely investigated mostly for inorganic materials. Wang *et al* [13] studied the intensity of the Raman signal in pressed powders using a fiber optic spectrometer similar to that employed in this work, in relation to the particle size for a range of inorganic compounds. They found a decrease of Raman intensity with increasing particle size which was attributed to increased diffuse reflectance for larger particles. Iqbal *et al* found an increase in Raman linewidths and decrease in peak frequencies in nanoscale silicon below crystallite sizes of 10 nm [99, 100] which is widely recognized today as associated with quantum localization in nanocrystals and quantum dots. In the present study, the objective was to investigate the average particle size of griseofulvin in nanosuspensions (with particle sizes well above the quantum limit but below the size range investigated as referenced) as a function of milling time by a combination of laser diffraction and Raman spectroscopy. The intensity of the 1706 cm^{-1} Raman line increases with decreasing particle size in agreement with Wang *et al* due to increased laser light throughput or decreased diffuse reflectance in suspensions with smaller particles.

Calibration models for particle size prediction of nanosized drug suspensions were created for multiple sets of data collected with two Raman instruments operating in the micro and fiber optic modes with different laser spot sizes of 15 μm and 100 μm, respectively. Different Raman instruments were employed to minimize the influence of particle size on calibration models. In all data sets, the Raman signal intensity used for calibration was taken as the difference between the maximum of the 1706 cm^{-1} Raman line and a baseline constructed from the minima immediately adjacent to the peak. First the calibration model was built to determine sensitivity of the instruments by monitoring

normalized peak intensity as a function of recorded spectrum at each particle size. Mean values for normalized intensity at each particle size was also calculated. Figure 4.8 shows a calibration model built for data collected with a laser spot size of 130 μm which resulted in much better correlation of the signal intensity to the spectrum number, R^2 = 0.95 (Mean R^2 = 0.97), comparing to data collected with the much smaller laser probe of a micro-Raman instrument, R^2 = 0.67. The variation in the R^2 values is mostly related to the sensitivity of Raman instruments and laser probe spot size. Higher peak noise and therefore lower R^2 (R^2 =0.67) value is reported for the instrument with smaller probing size. Based on the following determination, the remaining collection of Raman data was performed using the instrument with larger laser spot size. Variation of the peak intensity was next correlated with particle size values from laser diffraction analysis. Table 4.2 shows D90 and mean values of particle size measurements for griseofulvin nanosuspension as a function of milling time. For calibration purposes, the D90 value was used as it represented the particle size for the 90% of the sample. D90 along with larger laser spot size resulted in a better correlation value when compared to the mean value and larger laser spot size, R^2_{D90} = 0.94 vs R^2_{MEAN} = 0.87 respectively. Figure 4.9 shows the results of the particle size calibration based on intensity of the 1706 cm^{-1} Raman line for the data set collected with larger, 130 μm laser probe size for D90 and mean size of griseofulvin particles.

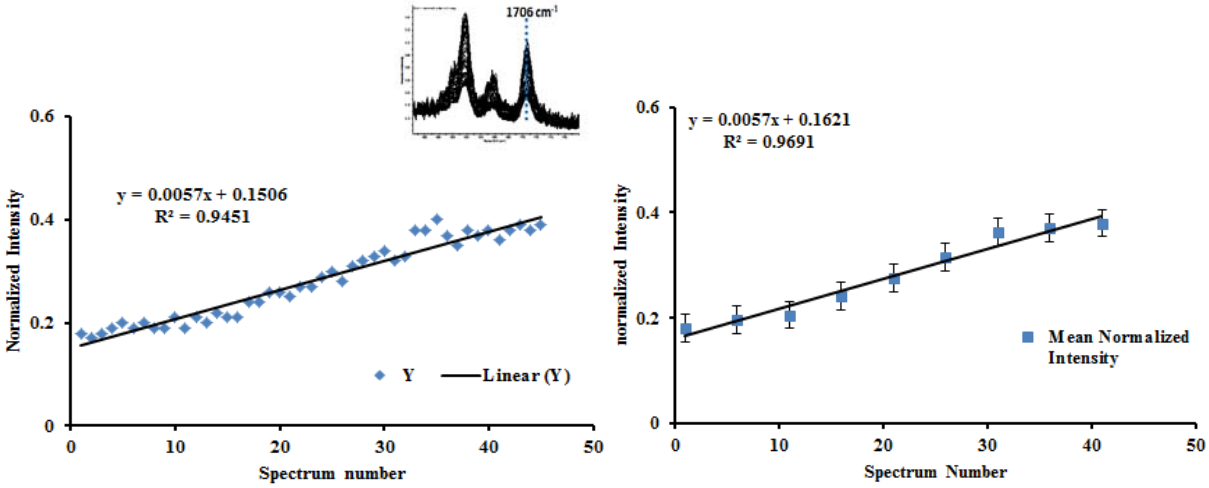

Figure 4.8 Calibration model representing normalized Raman spectra as a function of various particle sizes of sampled griseofulvin nanosuspensions: (a) Using all values of normalized intensity, (b) Using mean values of normalized intensity. Calibration performed by monitoring 1706 cm^{-1} Raman line in set of data collected with 130 μm laser spot size.

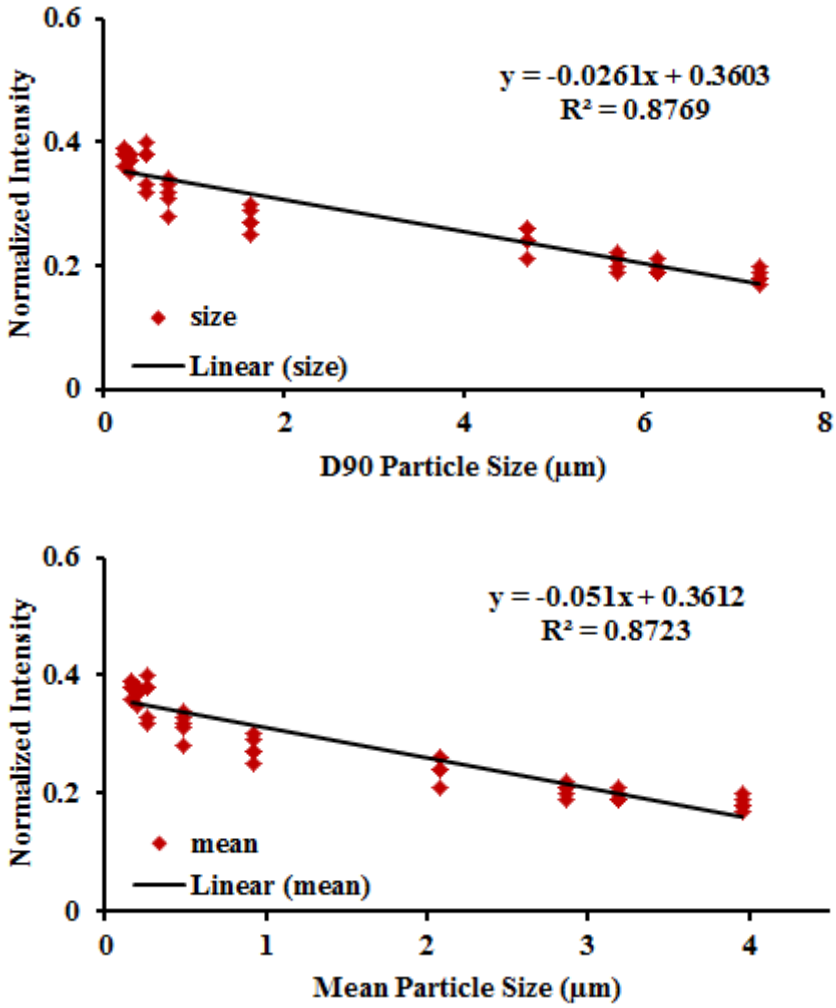

Figure 4.9 Correlation of D90 (top) and mean (bottom) particle sizes with normalized intensity of the 1706 cm^{-1} Raman line for griseofulvin nanosuspensions.

4.6 Conclusions

Polymer films loaded with small (low micron or submicron sizes) API particles represent API composite materials with many possibilities for functionalization and use as drug delivery matrices in different types of dosage forms. Trapping fine API particles in a polymeric matrix offers an advantageous way of harvesting engineered particles. The NIR-CI method provides an image of the spatial distribution of the trapped particles in

just a few minutes, and is currently being used to optimize the pharmaceutical formulation and its manufacturing process. Raman mapping on the other hand is being used to complement NIR-CI as discussed here (currently in a less frequent basis), and its primary role is to monitor the crystal form of the API, presence of defects and particle size distributions at the sub-micron level. Raman mapping and NIR-CI are two complementary spectroscopic techniques, which combined, provide detailed information about the distribution of API particles as well as chemical detail regarding the interaction between the drug and the polymer. Raman chemical imaging of thin films fabricated in an ERC Test Bed for film manufacture from micronized and nanosized griseofulvin suspensions confirmed the crystallinty of the embedded drug. This can result in even more innovative film design for poorly soluble drugs like griseofulvin, and can consequently enhance the dissolution profile and content uniformity of the formulation. In addition, applications of Raman spectroscopy for particle size and solid-state monitoring of griseofulvin suspensions during media milling showed that this technique is capable of on-line quality control during pharmaceutical manufacturing processes.

CHAPTER 5

SURFACE ENHANCED RAMAN SPECTROSCOPY (SERS) OF PHARMACEUTICAL AND STRUCTURALLY RELATED ENERGETIC MOLECULES

5.1 Overview

Trace level identification of chemical entities plays an important role in pharmaceutical, biological and environmental sciences, and in security applications [85, 101, 102]. Typical analytical techniques rely on the use of chromatographic methods (HPLC, GC) to separate and identify individual components. However, the chemical information obtained by this identification, is based mostly on UV-visible or fluorescence spectroscopic data which lack direct structural and molecular information of individual components of a complex system [103, 104]. Surface enhanced Raman spectroscopy (SERS) has been shown to be sufficiently sensitive for analytical applications in the pharmaceutical industry with the capability ultimately of single molecule detection [105, 106].

Discovery of SERS phenomenon was first observed in 1973 by Fleischman *et at* [107] who observed strong enhancement of the Raman signal from pyridine molecules adsorbed on a silver electrode. Few years later, in 1977, the phenomenon was also independently reported by Jeanmarie and Van Duyne [108] and Albrecht and Creighton [109]. SERS involves enhancement of the Raman signal via surface plasmons on, for example, nanostructured gold or silver nanowire substrates. Since the discovery, SERS has been extensively studied all around the world but much has yet to be learnt about the

phenomenon. One of the main challenges has long remained in the area of SERS-active substrate and in particular, its uniformity and reproducibility in detection. Over the past two decades, however, substantial progress has been achieved in the fabrication of improved substrates in a highly reproducible fashion due to advances in nanotechnology which allowed for the fabrication of various new designs [110, 111]. The standard molecules employed for trace level detection by SERS investigators are various dyes, such as Rhodamine 6G or crystal violet, [112, 113] used mostly due to their strong resonance properties, and benzenethiol [110] used due to its ability to form self-assembled monolayers (SAMs) on the SERS active area of substrates.

In this Chapter as part of the overall Raman spectroscopy theme of the thesis, the primary focus is on the trace detection of key pharmaceutical and structurally related organics rather than dyes and SAMs that are commonly used by others in SERS studies. Rather than developing new substrates, the focus will be on SERS detection and evaluation of one of a few, to the best of the author's knowledge, commercialized SERS substrates.

The substrates used are comprised of periodic, photonic crystal arrays of gold-coated, inverted square pyramidal cavities etched on a silicon wafer to induce surface-enhanced Raman scattering. In this study SERS was used to detect low concentrations of pharmaceutical compounds: griseofulvin, the active ingredient in antifungal drug, and acetaminophen or N-acetyl-p-aminophenol (APAP), a common pain medication; and the aromatic organic energetic compound 2,4,6 trinitrotoluene (TNT), and non-aromatic organic energetic compounds: 1,3,5-trinitroperhydro-1,3,5-triazine (RDX), and 1,3,5,7-tetranitro-1,3,5,7-tetrazocane (HMX). SERS is induced on these substrates by the strong

interaction of trapped surface plasmons (see section 5.2) within the void architecture of the cavities with incident visible and near-infrared laser radiation. As discussed below, highly reproducible surface-enhanced Raman spectra on the SERS-active substrates were obtained using 785 nm laser excitation at a detection level of 8.8×10^{-5} M for TNT and detection levels of 10^{-4} M for non-aromatic RDX and HMX. A lower detection level of 5.6×10^{-7} M was achieved for griseofulvin and the lowest, 1.3×10^{-8} M, was obtained for acetaminophen. The data for these molecules were compared to those obtained for the SERS standard dye Rhodamine 6G recorded under the same conditions.

Raman spectra of species at extremely low concentrations are those of the free molecules since the ordered lattice of a crystalline solid does not exist at that concentration level [106, 112]. In the case of APAP and griseofulvin adsorbed on the engineered photonic crystal substrates, the surface enhanced spectra were different from that of the molecular conformation in their most stable polymorphic forms. However, for energetic compounds with similar molecular dimensions as the pharmaceuticals, but with nitro and nitramine groups attached, such as, TNT, RDX, and HMX, the SERS spectra were essentially the same as the molecules in their known stable crystal forms.

5.2 The SERS Mechanism

Surface enhanced Raman scattering (SERS) when coupled with chemically induced enhancement due to molecular electronic transitions, is a powerful analytical tool which can provide chemical and molecular structure information as well as trace level detection comparable to that achieved by fluorescence spectroscopy [113-116]. Understanding how the local electromagnetic environment modulates the spectral response in SERS has been

an area of growing interest since the initial discovery of SERS [107, 108, 117, 118]. It has become increasingly clear that localized surface plasmons, which are quantized excitations associated with free electron oscillations in a metal or so-called "hot spots" from nanostructures like colloidal aggregates or crystal junctions and edges in nanostructured gold or silver coated substrates give rise to intense local fields that are responsible for the electromagnetic contribution to SERS [119-121] with enhancements up to 10^{12}. Another two or three orders of magnitude of chemically-induced enhancement can occur either due to resonance Raman scattering or from charge-transfer transitions resulting from the formation of a molecule-metal surface bond. The overall enhancement factor of 10^{14} to 10^{15} therefore makes single molecule detection possible by SERS. "Hot spots" typically occur at randomly formed locations or fractal structures that can fortuitously provide the configurations necessary for electromagnetically-induced SERS. These effects together with variations in surface roughness and particle size on nanostructured substrates [122] lead to irreproducibility in detection applications.

As a result of improvements in nanofabrication techniques, a number of regularly ordered periodic nanostructures have been prepared for surface-enhanced Raman spectroscopy [123, 124]. In spite of these efforts a number of challenges remain, particularly in the scalable and reproducible production of inexpensive, rugged and reusable SERS-active substrates. A new class of lithographically fabricated substrates comprised of a periodically arrayed photonic crystal void architecture capable of supporting trapped plasmons was initially fabricated by Perney *et al* [111] and commercialized as Klarite® by Mesophotonics Ltd (now owned by Renishaw Diagnostics Ltd). In this chapter the author will discuss the application of these highly robust

substrates for the SERS detection of low concentrations of the following widely used molecules:

- Griseofulvin and acetaminophen or N-acetyl-p-aminophenol (APAP) used as active ingredients in the pharmaceutical industry.
- Aromatic trinitrotoluene (TNT), and the non-aromatic nitramines: 1,3,5-trinitroperhydro-1,3,5-triazine (RDX) and 1,3,5,7-tetranitro-1,3,5,7-tetrazocane **(**HMX**)** used world-wide as the active ingredient in energetic formulations.

The differences in detection limits and surface-enhanced Raman spectra observed for these compounds and a qualitative explanation for these differences will be provided in the following sections.

5.3 Klarite® SERS Substrates

Klarite® SERS substrates consist of a periodic square lattice of inverted square pyramidal pits as shown by the scanning electron microscope image in Figure 5.1 (a). The pits are produced by conventional photolithography using a silicon dioxide mask on a (100) oriented silicon wafer. KOH was used to preferentially etch the (111) planes to give a periodic array of inverted pyramidal pits. The pitch or periodic separation of the pits formed ranged from 0.7 μm to 1.0 μm. A uniform 300 nm layer of gold was sputtered on the wafer after completion of the etching process to give a smooth coating on the pit walls and the flat regions between the pits. The substrate design allows the tunable plasmon bands to be in resonance with commonly used excitation 632 and 785 nm wavelengths of Raman spectrometers. The absence of surface Raman enhancement (see Figure 5.3) from the coating away from the etched pits shows that the overall coating, even in the pits, is smooth and therefore does not excite SERS. A tapping mode atomic

force microscope (AFM) image of a gold-coated substrate was obtained using a Nanoscope III MultiMode Scanning Probe Microscope and shown in Figure 5.1 (b). The reproducibility of the SERS signal across the active area was investigated by Perney *et al* [111].

(a)

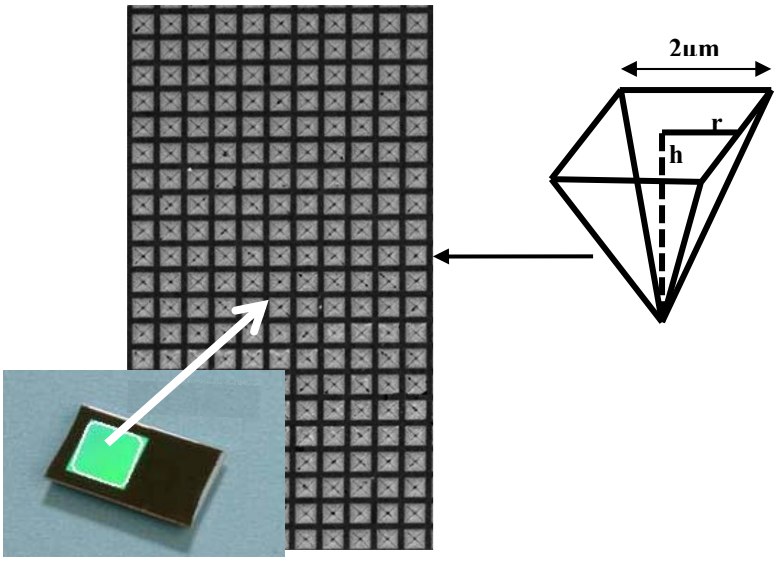

(b)

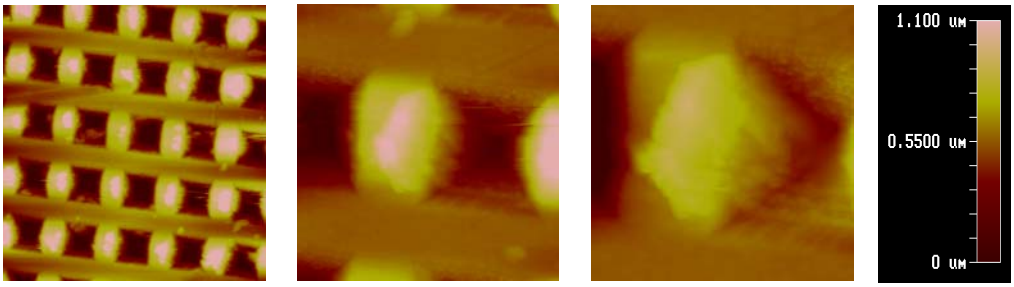

Figure 5.1 (a) Top view scanning electron microscope (SEM) image showing 2 µm wide inverted pyramids, and (b) A 10 mm wide atomic force microscope (AFM) image showing the inverted pyramidal pits of the photonic crystal SERS substrate with a 300 nm thick gold layer. Blow ups of the pits and the region between the pits are shown on the images to the right.

5.4 Experimental Details

Raman Spectroscopy: Raman scattering experiments were carried out using a Mesophotonics SE 1000 Raman spectrometer with a 250 mW near-infrared laser emitting at 785 nm and a 130 μm diameter spot size. The system operates with an automated XYZ stage and a video camera for easy visualization of the sample. A typical acquisition time used was 10 seconds per scanned spectrum with the data averaged over 10 scans.

Preparation of Solutions: Solutions of the pharmaceutical and energetic compounds under investigation were prepared in high purity solvents (from Sigma Aldrich): griseofulvin (Sigma-Aldrich) in acetone, APAP (Sigma Aldrich) in acetone, TNT (obtained from the US Army) in toluene, RDX (obtained from the US Army), HMX (obtained from the US Army) in acetone, and the SERS standard dye Rhodamine 6G (Lambda Physik). For each compound, the stock solution was made first and diluted by a factor of ten each time to obtain further dilutions. For example in the case of acetaminophen, the stock solution concentration was 20 mg/ml (0.13 M); it was diluted to obtain concentrations of 2 mg/ml (1.3×10^{-2} M), 0.2 mg/ml (8.81×10^{-3} M), 0.02 mg/ml (8.81×10^{-4} M), 0.002 mg/ml (8.81×10^{-5} M), 0.0002 mg/ml (1.3×10^{-6} M),0.00002 mg/ml (1.3×10^{-7} M), and 0.000002 mg/ml (1.3×10^{-8} M). A micro-pipette was used to deposit 0.1 μl of solution on the active region (Figure 5.1) and allowed to dry quickly at room temperature in air. The spectrum of a pristine SERS substrate was similarly recorded; baseline subtracted from the raw data and processed using the ACDLABS 10.0 software from Mesophotonics, to obtain the spectra shown.

Amorphous griseofulvin was prepared by melting a small amount of crystalline griseofulvin on a glass slide heated on a hot plate at 220ºC until completely melted, and

cooled at room temperature to form a solid film. The Raman spectrum of amorphous griseofulvin was recorded immediately upon solidification of the film. The appearance of a strong peak at 656 cm^{-1} and the absence of a peak at 820 cm^{-1} in the spectrum was used to confirm the formation of amorphous griseofulvin.[23] The same procedure was used for preparing amorphous acetaminophen and obtaining its Raman spectrum.

5.5 The SERS Enhancement Factor (SERS EF)

The effectiveness of the Klarite substrate was determined by measuring the enhancement factor (EF) expressed by the following equation [125]:

$$\text{SERS EF [Raman Shift } (cm^{-1})] = \frac{N_{vol} \bullet I_{SERS}}{N_{SERS} \bullet I_{vol}} \qquad (5.1)$$

N_{vol} – Number of molecules in the probed volume area

N_{sers} – Number of molecules in the probed SERS substrate area

I_{vol} – Intensity of the Raman signal from the probed volume

I_{sers} – Intensity of the Raman signal form the SERS substrate.

To determine SERS EF, the limit of detection for all investigated molecules was measured by both conventional and surface-enhanced Raman spectroscopy and compared with that for Rhodamine 6G (R6G), which was used as a SERS standard in this study.

Using conventional Raman spectroscopy, the lowest level of detection for R6G solution was determined to be 0.001004 mol/L or $1x10^{-3}$ M which corresponded to the 4.1×10^{13} number of molecules (N_{vol}) in the given volume of the probed solution (V_{beam}) and was calculated as follows:

$$V_{beam} = \frac{4}{3}\pi r^3 = \frac{4}{3}\pi(6.5\times10^{-3}cm^3)^3 = 6.5\times10^{-7}ml$$

$$N_{vol} = 1x10^{-3}M \times 6.022\times10^{23} \times \frac{6.5\times10^{-7}ml}{10ml} = 4.1\times10^{13}$$

The intensity of the Raman line (I_{vol}) was calculated by integrating the area under the spectral peak recorded for the lowest detectable concentration by conventional Raman measurement. I_{vol} for R6G was found to be 7533 counts/seconds.

For surface-enhanced Raman spectroscopy, the lowest detectable concentration for R6G was measured to be 0.001004 x 10^{-6} mol/L or 1.x10^{-9} M. Similar calculations were followed for the SERS probed volume (V_{SERS}) to calculate the number of molecules in that volume (N_{SERS}). SERS volume (V_{SERS}) was calculated based on the substrate area probed by the laser, the number of wells probed in that area and their corresponding volumes [Figure 5.1 (a)]. For the number of wells probed:

$$\text{Wells}_{\text{probed}} = \frac{A_{laser}}{A_{well}} = 3318$$

Since, the volume of each well corresponds to:

$$V_{well} = \frac{Ah}{3} = 0.9\mu m^3$$

Then, the volume probed by the laser beam on the SERS substrate is:

$$V_{SERS} = 0.9\mu m^3 \times 3318 wells = 3.1\times10^{-9}ml$$

This corresponds to the number of molecules probed on SERS substrate given by:

$$N_{SERS} = 1x10^{-9}M \times 6.022\times10^{23} \times \frac{3.1\times10^{-9}ml}{10ml} = 1.9\times10^{5}$$

The SERS intensity (I_{SERS}) was calculated in similar fashion as I_{vol} except the integrated area under the spectral peak corresponded to the lowest detectable

Table 5. 1 Enhancement Factors and Contributing Concentrations of Probed Compounds to the SERS Recorded Spectra

Compound	Enhancement Factor	Limit of Detection (M)
R6G	$1.0x10^{8}$	$1.1x10^{-9}$
TNT	$6.1x10^{5}$	$8.8x10^{-5}$
Griseofulvin	$1.2x10^{8}$	$5.6x10^{-7}$
APAP	$5.4x10^{8}$	$1.3x10^{-8}$

concentration of each of the investigated compounds using the SERS substrate. Rhodamine 6G gave an enhancement factor of 10^{8} from equation 5.1 as listed in Table 5.1 together with enhancement factors for TNT, griseofulvin and APAP. Enhancement factors for HMX and RDX were not obtained because for safety and security reasons only limited amounts of these compounds were available.

5.6 Raman Spectra of Investigated Molecules on the SERS Substrates

Surface enhanced Raman spectra of griseofulvin, APAP, TNT, RDX, and HMX were taken on the SERS substrates described above using near-infrared excitation at 785 nm. The goal of this work was to examine and evaluate the spectra obtained and determine the SERS sensitivity and enhancement factors using this new generation of photonic crystal substrates. The highly ordered array of inverted square pyramids covered with gold results in highly reproducible Raman signals at low analyte concentrations. The substrate design supports the generation of surface plasmon standing waves localized inside the bottom of each pit, its sidewalls and the connecting surface bridges between the pits [Figure 5.1 (a)]. As a result, the electromagnetic fields are found along the

surface bridges and inside the inverted pyramidal pits [111] leading to effective increase in magnitude of both incoming radiation and scattered fields. The total SERS enhancement is a product of two mechanisms as mentioned above: electromagnetic field (EF) enhancement from the strong coupling between the surface plasmons on the substrate and molecular vibrational excitations, and chemical enhancement (CE) associated with the more localized molecule-surface charge transfer interaction [11]. The surface irregularities of the SERS substrate can significantly affect the enhancement factor and reproducibility but are minimized in the photonic crystal substrates used here by engineering of the pit structure. Reproducibility of the Raman signal across the substrate is reported with less than 10% RSD for a substrate with SAMs of benzenethiol [111]. Reports using SAMs model systems for a range of SERS substrates show a high degree of reproducibility [110, 126]. The results have been used to understand the selective enhancement or loss of intensity of Raman lines by identifying molecule-substrate orientation [127, 128]. SAMs result in monolayer surface bonding which strongly influences the homogeneous distribution of the molecules on a SERS substrate to provide more controllable electromagnetic enhancement. Other studies, however, have shown that this selectiveness in enhancement of Raman lines can be attributed to increased Raman scattering cross sections caused by changes in molecular electronic structure due to surface bonding rather than molecular orientation vis-a-vis the substrate [11, 126, 129]. Examining the behavior of various organic compounds discussed below on the arrayed photonic crystal SERS substrates, it is noticed that some of the SERS Raman spectra vary from that of the bulk material. A possible explanation for this behavior is discussed.

TNT

The Raman spectrum for solid TNT in the 200 to 2000 cm^{-1} fingerprint region is shown in Figure 5.2 (A). Important spectral features consist of a somewhat broadened, intense line peaked at 1362 cm^{-1} assigned to the symmetric stretching -NO_2 mode of the TNT molecule, a doublet at 822 cm^{-1} and 791 cm^{-1} assigned to scissoring and wagging motions respectively of the -NO_2 groups, and lines at 1618 cm^{-1} and 1535 cm^{-1} assigned to the aromatic C=C stretching and asymmetric stretching -NO_2 modes, respectively [130]. The broadening of the line due to the symmetric stretching -NO_2 mode is due to unresolved splitting of this mode caused by a breakdown of the ring symmetry in TNT due to electron donation of the methyl group to the aromatic ring [130]. The lines between 822 and 1362 cm^{-1} can be assigned to in-plane ring bending, CH_3 deformation and C-N stretching modes of TNT, whereas the lines below 791 cm^{-1} can be contributed to out-of-plane ring bending, ring distortion and C-CH_3 wagging modes [131].

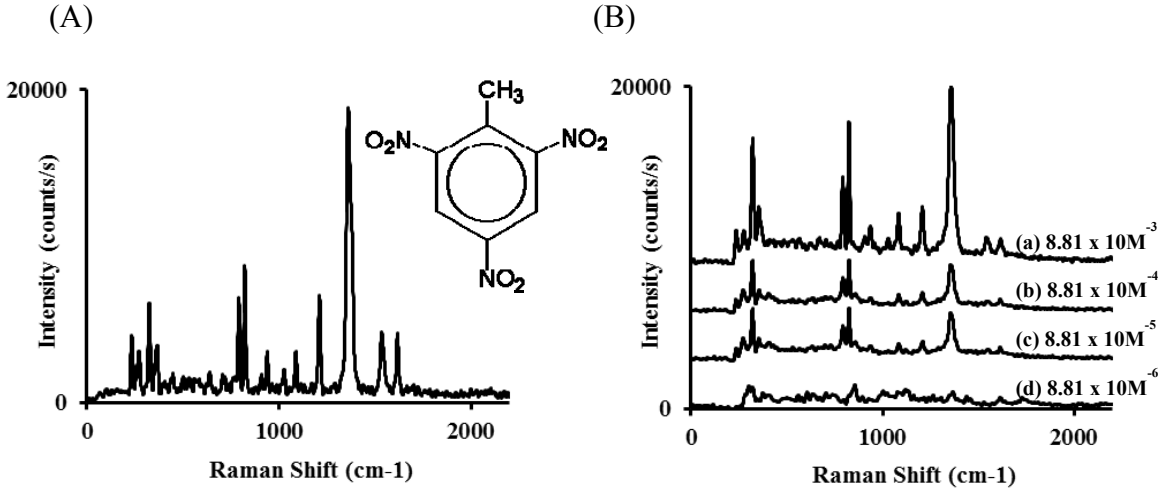

Figure 5.2 (A) Background-subtracted solid TNT spectrum with its molecular structure attached, and (B) SERS from samples prepared by evaporating 0.1 µl solutions of various concentrations of TNT in toluene. 785 nm laser radiation and 10 seconds acquisition time were used for recording the spectra for: (a) 2 mg/ml or $8.81x10^{-3}$ M solution, (b) 0.2 mg/ml or $8.81x10^{-4}$ M solution, (c) 0.02 mg/ml or $8.81x10^{-5}$ M solution and (d) 0.002 mg/ml or $8.81x10^{-6}$ M solution.

Background-subtracted, 10 seconds SERS Raman spectra in the 100 to 2000 cm^{-1} range taken from the active region of the SERS substrates from TNT solutions of different concentrations in toluene down to 0.002 mg/ml or $8.81x10^{-6}$ M, are shown in Figure 5.2 (B). All Raman features are evident in the 0.02 mg/ml spectrum while the stronger Raman features of solid TNT are discernable in the 0.002 mg/ml spectrum which is equivalent to 8.81 x 10^{-6} M TNT in toluene. The weaker features of the 0.002 mg/ml spectrum, however, become evident at higher integration times. It is estimated that the level of detection for TNT is about 0.002 mg/ml solution or 8.8 x 10^{-5} M. The enhancement factor of 10^5 is calculated for TNT using equation 5.1 above as listed in Table 5.1. No Raman spectra at these low concentration levels are observed from the flat inactive region of the substrate away from the inverted square pyramidal cavities.

Comparison of the solid to the SERS Raman data indicates that the overall spectral distribution of the lines is the same. This is also true for data recorded using 632.8 nm excitation. Small shifts in line positions are however observed in the SERS data. For example, the line at 1362 cm^{-1} in the solid state spectra assigned to the symmetric -NO_2 stretching mode shows a highly reproducible down-shift in the SERS data by 3-5 cm^{-1} probably due to the absence of strong intermolecular interactions in the dilute phase sampled by SERS.

RDX and HMX

The Raman spectra for highly pure solid RDX and the stable β-polymorph of HMX used in this study are shown in the 250 to 2000 cm^{-1} fingerprint region in Figures 5.3 (A) and 5.4 (A), respectively. The spectra consist of a complex pattern of several more intense

lines than those in the same region for TNT. The lines in the 250 to 800 cm^{-1} region for both RDX and HMX can be assigned to ring deformation, NO_2 scissoring, rocking and wagging motions [132, 133]. The strongest line is at 882 cm^{-1} in RDX and at 832 cm^{-1} in the larger HMX molecule. In RDX this line can be assigned to a mode consisting of C-N stretching, N-N stretching and $–CH_2$ rocking [132]. There are also two nearby intense lines in HMX at 879 and 949 cm^{-1} which been assigned to ring breathing or stretching modes in HMX by Iqbal *et al* [133] and in RDX by Ciezak and Trevino[132]. The line at 1309 cm^{-1} in RDX and at 1311 cm^{-1} in HMX, and lines between 1500 and 1600 cm^{-1} in RDX and HMX can be assigned to the symmetric and asymmetric stretching modes, respectively, of the $-NO_2$ groups [133].

The surface-enhanced Raman spectra for RDX and HMX taken from the SERS active region of the substrate are shown in Figures 5.3 (B) and 5.4 (B), respectively. The limit of detection of the primary Raman lines is 0.1 g/ml or 4.5 x 10^{-4} M which is about two orders of magnitude higher or less sensitive than the limit of detection for TNT. This suggests that the plasmon-phonon coupling responsible for SERS is much higher for the aromatic TNT molecule with more delocalized electrons. Moreover, the surface-enhanced spectra of RDX and HMX have fewer lines relative to the solid state spectra, probably because the spectra are in the highly dilute molecular phase and therefore the strong intermolecular hydrogen bonding, O···O and O···C interactions present in the solid are absent. The strongest Raman line at 882 cm^{-1} in solid RDX downshifts by 6 cm^{-1} similar to the behavior observed for the $-NO_2$ symmetric stretching mode in solid TNT which is the strongest Raman line in the TNT spectrum. In HMX however the line at 949 cm^{-1} downshifts by 12 cm^{-1} whereas the line at 832 cm^{-1} increases in frequency by

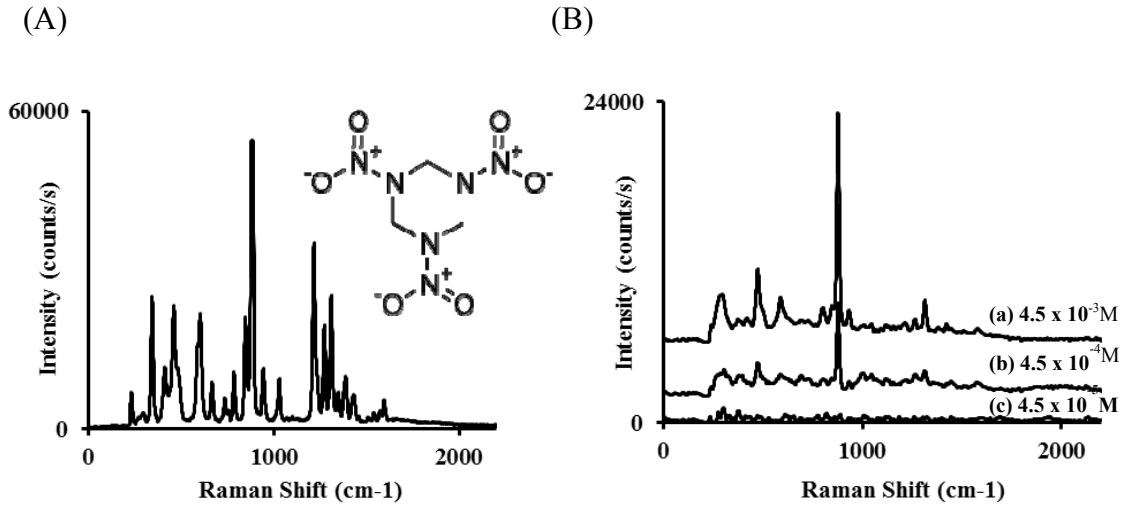

Figure 5.3 (A) Background-subtracted solid RDX spectrum with its molecular structure attached and (B) SERS from sample prepared by drying 0.1 µl solutions of various concentrations of RDX in acetone, using 785 nm laser radiation and 10 seconds acquisition time: (a) 1 mg/ml or 4.5 x 10^{-3} M solution, (b) 0.1 mg/ml or 4.5 x 10^{-4} M solution, and (c) 0.01 mg/ml or 4.5 x 10^{-5} M solution.

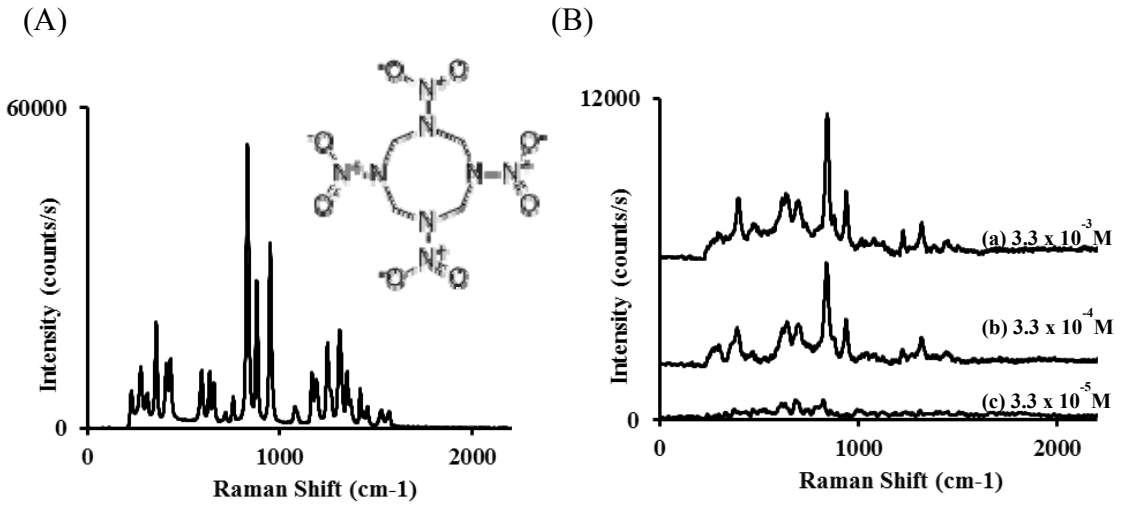

Figure 5.4 (A) Background-subtracted solid β-HMX spectrum with its molecular structure attached, and (B) SERS from sample prepared by evaporation of 0.1 µl solutions of various concentrations of β-HMX in acetone, using 785 nm laser radiation and 10 seconds acquisition time: (a) 1 mg/ml or 3.3 x 10^{-3} M solution, (b) 0.1 mg/ml or 3.3 x 10^{-4} M solution, and (c) 0.01 mg/ml or 3.3 x 10^{-5} M solution.

12 cm^{-1} due to structural renormalization in the molecular phase. Another interesting feature is that the line assigned to the -NO_2 symmetric stretching mode increases in frequency relative to the solid in SERS both for RDX and HMX by 5 to 7 cm^{-1} in contrast to the behavior of the corresponding mode in TNT where there is a downshift.

Griseofulvin

The Raman spectrum of solid griseofulvin in the 100 to 210 cm^{-1} region are shown in Figure 5.5 (A) and are in agreement with the spectrum reported by Zarow *et al* [23]. Griseofulvin is an aromatic organic but unlike TNT does not have strongly electronegative nitro substituent groups. A series of background-subtracted SERS Raman spectra of drop deposited griseofulvin of concentrations down to 0.0002mg/ml or 5.6 $x10^{-7}$M and the normal Raman spectrum of amorphous griseofulvin, are shown in Figure 5. 5 (B). The enhancement factor of 10^8 was calculated based on equation (5.1) and is shown in Table 5.1. Characteristic Raman lines for the SERS spectra of griseofulvin molecules show major differences when compared to the Raman spectra of solid, crystalline griseofulvin as shown in Table 5.2. A detailed examination of all SERS spectra shows strong resemblance of these spectra with the normal Raman spectrum of amorphous griseofulvin. Upon crystalline-to-amorphous transition, the distinctive Raman line at 820 cm^{-1} corresponding to the cyclohexanone ring stretching mode is completely lost [23] which is also the case for the SERS spectra. In addition, the triplet in the 650 cm^{-1} spectral region of the crystalline form transforms into a broad singlet at 646 cm^{-1} in the SERS spectra. The lines for the –CH in-plane deformation in the solid state Raman spectra show a highly reproducible 2 to 5 cm^{-1} upshift in the SERS data and are more

intense than the corresponding Raman lines in amorphous APAP discussed below. Similar frequency upshifts are observed for the -CH_3 and -CH_2 deformation, and C=O and C=C stretching modes as summarized in Table 5.2 which indicate increases in C-H, C=O and C=C bond force constants on going from the crystalline to the molecular state. Increases in line frequencies are also seen in part on going from the crystalline to the amorphous phase since the amorphous phase of an organic can be considered to be a frozen liquid with randomly oriented molecules and no long range inter-molecular coherence [25].

Even though the EF for griseofulvin and APAP are of the same order (10^8), the corresponding detection sensitivities are different, 10^{-7} M versus 10^{-8} M, respectively. This can be related to the presence of electron withdrawing and donating groups on the respective aromatic benzene rings in each of the molecules which can influence the electron density on the ring. In griseofulvin, the presence of an -OCH_3 moeity can result in transfer of some of the substituted group electrons to the ring via a resonance effect. On the other hand, in case of griseofulvin, the presence of a strong electronegative -Cl group (similar to –NO_2 groups in TNT) will promote withdrawal of ring electrons via the sigma bond to decrease electron density on the aromatic ring. In the case of APAP, however, the aromatic ring is bonded to electron donating groups, –OH and –H-N-C=O and hence electron density on the aromatic ring will increase, resulting in increased coupling with surface plasmons and higher SERS sensitivity in agreement with experimental results.

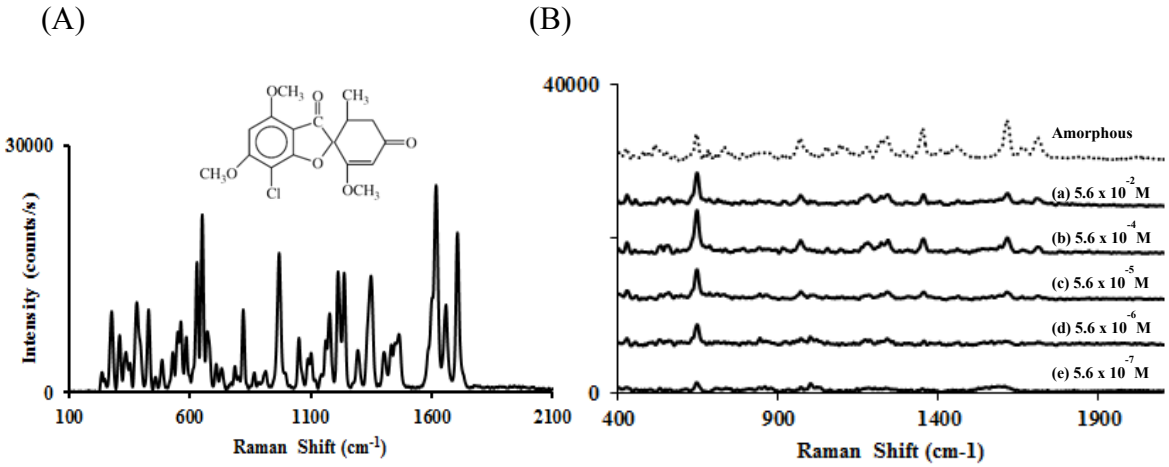

Figure 5.5 (A) Solid spectrum of griseofulvin with its molecular structure attached, (B) SERS from sample prepared by evaporating 0.1 µl solutions of various concentrations of griseofulvin in acetone, using 785 nm laser radiation and 10 seconds acquisition time: (a) 20 mg/ml or 5.68 x10^{-2} M solution, (b) 0.2 mg/ml or 5.68 x10^{-4} M solutions, (c) 0.02 mg/ml or 5.68 x10^{-5} M solution, (d) 0.002mg/ml or 5.68 x10^{-6} M solution and (e) 0.0002 mg/ml or 5.68 x10^{-7} M solution. Top Raman spectrum shows melt-quench amorphous griseofulvin.

Table 5.2 Raman Frequencies and Qualitative Mode Assignments in Crystalline, Amorphous and SERS Griseofulvin

Crystalline Frequency (cm^{-1})	Amorphous Frequency (cm^{-1})	SERS Frequency (cm^{-1})	Qualitative Assignments
428	426	428	C-Cl deformation
628	-	-	C-Cl stretching, ring deformation
650	647	646	C-Cl stretching
820	-	-	Cyclohexanone ring stretch
968	967	968	Benzene ring asymmetric stretch
1178	1178	1181	Ring vibration, -C-O-C stretch
1213	1217	1220	-CH in-plane deformation
1238	1239	1242	-CH in-plane deformation
1349	1350	1354	- CH_3 and -CH_2 deformations
1618	1613	1614	C=O mixed with C=C stretch
1659	1663	1663	C=C stretch in cyclohexanone
1707	1706	1709	C=O stretch in benzofuran

Acetaminophen (APAP)

APAP, which is a purely aromatic molecule like griseofulvin, can exist in three polymorphic forms besides its solid amorphous phase [73]. The monoclinic yype I phase crystallizes as the most thermodynamically stable form. Its solid Raman spectrum in this stable phase in the 200 to 2000 cm^{-1} fingerprint region is shown in Figure 5.6 (A). The characteristic Raman lines at 1650 cm^{-1} and 1616 cm^{-1} are assigned to the C=O stretching and the N-H deformation modes, respectively, as indicated in Table 5.3. The line at 1562 cm^{-1} is attributed to the H-N-C=O amide carbonyl group vibration, the line at 1324 cm^{-1} to the C-H bending mode whereas the line at 1169 cm^{-1} is due to the C-H deformation vibration. The strongest Raman lines are in the 800 cm^{-1} spectral region where characteristic modes for the phenyl ring stretch and aromatic C-H out of plane vibration exist at 796 cm^{-1} and 856 cm^{-1} respectively [74, 84].

Surface enhanced Raman spectra of APAP taken from the active region of the substrate show noticeable differences from the solid Raman spectra of the drug mainly because as in griseofulvin, the SERS spectra correspond to those of APAP molecules. The limit of detection for the primary enhanced line at 856 cm^{-1} is 2 x 10^{-6} g/ml or 1.3 x 10^{-8} M, which gives an enhancement factor of 10^{8} based on equation (5.1). The C=O stretching, N-H deformation and HN-C=O bending-stretching modes of the solid Raman spectrum are very weakly enhanced and can be only detected at high concentrations of 2 mg/ml and cannot be observed for further dilutions as shown in Figure 5.6 (B). It is interestingly noticed that the strongest enhancement is recorded for the mode corresponding to the aromatic phenyl ring vibrations in the 800 cm^{-1} region. The SERS

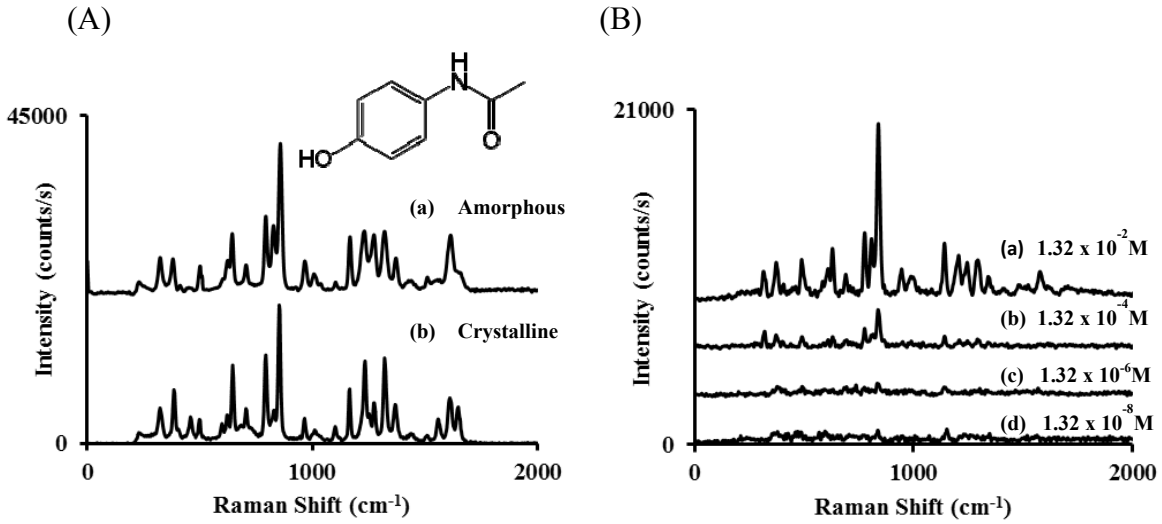

Figure 5.6 (A) Normal Raman spectrum of (a) solid and (b) amorphous acetaminophen with molecular structure attached, and (B) Background-subtracted SERS spectra from sample prepared by evaporating 0.1 µl solutions of various concentrations of acetaminophen in acetone, using 785 nm laser radiation and 10 seconds acquisition time. The SERS spectra are for: (a) 2 mg/ml or 1.32 x 10^{-2} M, (b) 0.02 mg/ml or 1.32 x 10^{-4} M solution, (c) 0.0002 mg/ml or 1.32 x 10^{-6} M solution, (d) 0.000002 mg/ml or 1.32 x 10^{-8} M solution.

spectral features resemble the normal Raman spectrum of amorphous acetaminophen as in griseofulvin, indicating the absence of intermolecular interactions. The highly reproducible up- and down-shifts of several Raman lines in the SERS spectra are summarized in Table 5.3. The strongest Raman line at 856 cm^{-1} upshifts by 4 cm^{-1} similar to the behavior of the C-H out-of-plane bending mode for amorphous APAP. The remaining Raman lines in the SERS spectra show 2 cm^{-1} to 5 cm^{-1} downshifts and agree with shifts of these lines on going from the crystalline to the amorphous phase. Two Raman lines, however, show even higher downshifts than the corresponding amorphous phase Raman lines. These lines are the out-of-plane deformation mode at 326 cm^{-1} which decreases in frequency by 5 cm^{-1} in the SERS spectra, whereas only a 2 cm^{-1} downshift is seen for this line in the amorphous phase. Similarly to -N-H deformation mode at 1616

cm^{-1} decreases in frequency by 5 cm^{-1} in the SERS spectra and only 2 cm^{-1} in the spectrum of the amorphous phase. This trend is opposite to what is seen in griseofulvin, where most of the SERS lines showed upshifts suggesting increases of the interatomic force constants. This behavior may be associated with differences in molecular structure (see discussion in griseofulvin section).

Table 5.3 Raman Frequencies and Qualitative Mode Assignments in Crystalline, Amorphous and SERS Acetaminophen

Crystalline Frequency (cm^{-1})	Amorphous Frequency (cm^{-1})	SERS Frequency (cm^{-1})	Qualitative Assignments
326	324	321	Out-of-plane ring deformation
388	382	382	
462	-	-	Out-of-plane ring deformation
501	502	499	Out-of-plane ring deformation
649	643	643	In-plane ring deformation
796	794	794	phenyl ring stretch [74]
856	859	859	C-H out-of-plane bend
1169	1167	1166	C-H in-plane bend
1237	1231	1230	C-N stretch
1278	1273	1273	O-H and C-O combination, (ar) C-N stretch
1324	1321	1320	C-H bend
1371	1372	1369	$-CH_3$ umbrella mode
1562	-	-	-H-N-C=O stretch [74]
1616	1614	1611	-N-H deformation [74]
1650	1660	-	C=O stretch [74]

5.7 Conclusions

The results presented here using SERS substrates comprised of arrays of inverted pyramidal pits for three types of energetic and pharmaceutically active organic molecular crystals show that the SERS detection sensitivity or enhancement factor is the lowest for the non-aromatic nitramine compounds RDX and HMX and nitro-substituted aromatic TNT, where the enhancement factor approaches 10^6. Increase of enhancement factors by another 2 orders of magnitude is achieved for purely aromatic pharmaceutical molecules

griseofulvin and APAP, and also for the dye molecule Rhodamine 6G. The enhancement factors achieved are however many orders of magnitude lower than single molecule detection levels near 10^{14} achieved for dye molecules on "hot spot" sharp nanoscale tips or between nanometer-spaced nanoparticles. On the other hand since the plasmons are localized within cavities in the SERS substrates used, the plasmon field distributions are matched to reach deep inside the mid-sized molecules probed here to provide, unlike for "hot spot" nanostructures, a high degree of reproducibility of the spectral signals obtained.

CHAPTER 6

SUMMARY, CONCLUSIONS AND SUGGESTED FUTURE WORK

The work discussed in this thesis is focused on themes related to the application of Raman spectroscopy as a sensing and non-destructive characterization tool for use primarily in the pharmaceutical industry. Although the complementary tool of near infrared spectroscopy is more widely used in this industry, Raman techniques involving fiber optics are slowly emerging as a methodology to provide not just sensing but also molecular and crystal phase science that are of critical importance for quality-controlled drug manufacture.

In Chapter 1, an introduction and a brief overview of the quality requirements involving PAT (Process Analytical Technology) initiative, was presented with an emphasis on real time quality control and better understanding of novel materials down to the nanoscale level. The analysis of manufactured products requires some of the most effective and information-rich tools of solid-state science. Raman spectroscopy, as a highly advanced, molecule-specific method, was presented in its theoretical aspects and shown to be an excellent method for this task, particularly for the challenges of understanding molecular interactions in complex solids. Complementary methods used in this work were also briefly discussed.

Structural disorder induced by cryogenic milling and by heating to the amorphous phase in the active pharmaceutical ingredient, griseofulvin primarily studied by Raman spectroscopy with contributions from small (using Synchrotron techniques) and wide angle X-ray powder diffraction (XRPD), fluorescence spectroscopy and differential

scanning calorimetry (DSC) are presented in Chapter 2. A broad, novel frequency-independent scattering background superimposed on the Raman spectra observed together with changes in intensities and splittings of some of the Raman lines due to lattice (inter-molecular) and molecular modes are interpreted and discussed in detail. In the cryomilled samples this strong background can be deconvoluted into two components: one due to lattice disorder induced by cryomilling and the other due to Mie scattering from nanosized crystallites. Related but more intense background scattering for thermally produced amorphous griseofulvin can be fitted to a single Lorentzian function and attributed to lattice disorder. Comparison of Raman and fluorescence data showed no relation of the Raman background intensity to impurity- or molecular defect- induced fluorescence as fluorescence measurements showed an intrinsic fluorescence signal in as-received griseofulvin that does not correspond to the inelastic background in the Raman spectra, and moreover decreases in intensity on cryomilling. Broad two-component background scattering for cryomilled griseofulvin was also observed by wide-angle XRPD measurements and attributed to lattice disorder but at much longer correlation lengths than in Raman scattering. Disorder at two correlation lengths indicated by the XRPD data was consistent with the background scattering components in the Raman data associated with lattice disorder and Mie scattering. Persistence of this disorder to even longer lengths is evident in small-angle Synchrotron XRPD data on micronized griseofulvin taken as a function of temperature from the crystalline to the amorphous phase. Effective identification of process induced structural disorder is likely to be an important aspect of pharmaceutical formulation manufacturing. Disordered domains formed can progressively transform during processing into long range disorder and result

in polymorphs or amorphous phase formation that would impact the quality of the dosage form produced.

Different aspects of polymorphism of the widely used model drug acetaminophen (APAP) are considered in Chapter 3. Also in this chapter and in the related Appendix A, the molecular and lattice vibrations observed in APAP in its various forms and type I APAP in single crystal form, respectively, were measured and interpreted. Oriented single crystal Raman data and its temperature dependence were measured for the first time to the best of our knowledge in order to understand milling behavior. APAP exists in three different crystalline arrangements and a disordered amorphous form. The type II polymorph is of potential pharmceutical interest due to its better tabletting characteristics relative to the stable type I polymorph – however, as normally prepared, it is not stable enough for long term use as a pharmaceutical product. In this research new interfaces were successfully created in type I APAP by micronization and by dry-coating with nanosized silica to significantly extend the stability of type II obtained from this modified type I phase. Raman spectroscopy, and XRPD, SEM and dissolution techniques were employed to monitor and characterize the stabilized phase. One interesting result obtained was that with increasing time a diffuse scattering background appeared in the Raman spectra which varied with time. This scattering is similar to what was seen in cryomilled griseofulvin and was qualitatively attributed to the slow growth and annealing of nanosized nuclei of the stable type I polymorph in the matrix of the stabilized type II APAP phase at ambient conditions. Intrinsic dissolution data were also measured and showed an improvement in mass release for type II APAP obtained from micronized and nanocoated type I APAP.

Raman sensing and imaging of pharmaceutical dosage and manufacturing forms, involving the model API griseofulvin, are the topics discussed in Chapter 4. Monitoring of thin gel griseofulvin films fabricated from micronized powders and nanosuspensions provided analytical process understanding of molecular interactions at the micro- and nano-scale. Findings and scientific understanding, such as those described in Chapters 2 and 3, were used to help interpret off-line Raman mapping of these novel dosage forms. Raman mapping complemented by near infrared chemical imaging (NIR-CI), was used to investigate solid-state morphology and agglomerates of the embedded particles in the polymeric matrix of the gel. NIR-CI provides scrutiny at comparatively larger scales than Raman imaging, to show the absence of large clusters and various degrees of drug dispersion and aggregation throughout the film area covered with the drug. Raman imaging evaluated dispersion at sub-micron levels and confirmed crystallinity of the embedded drug for films fabricated with micronized and nanosized griseofulvin suspensions based on the presence of characteristic Raman lines for crystalline griseofulvin in the 500 to 850 cm^{-1} spectral range. The use of fiber-optic Raman spectroscopy for particle size characterization was developed for in-line monitoring of griseofulvin nano-suspensions with 300 nm sized particles obtained by media milling. The crystallinity of the suspensions and size prediction based on Raman signal intensity showed the capability of this technique for on-line quality control during pharmaceutical manufacturing.

Chapter 5 discusses the use of Raman spectroscopy for sensing down to trace levels of organic pharmaceutical and energetic solids. Photonic crystals in the form of periodic arrays of gold-coated, inverted square pyramidal cavities etched on a silicon

wafer were used to induce surface-enhanced Raman scattering (SERS) to detect trace concentrations of purely aromatic pharmaceutical compounds griseofulvin and APAP; non-aromatic nitramine compounds 1,3,5-trinitroperhydro-1,3,5-triazine (RDX) and 1,3,5,7-tetranitro-1,3,5,7-tetrazocane (HMX) and nitro-substituted aromatic 2,4,6 trinitrotoluene (TNT). For griseofulvin and APAP, amorphous-like Raman spectra were observed at trace levels (enhancement factor of 10^8-10^9) whereas the energetic compounds with much lower enhancement factors showed Raman spectra corresponding to their crystalline phases with correlated molecules. This suggests that the amorphous phase in organics corresponds to uncorrelated molecules in a matrix, although the experimental conditions here are well below the single molecule detection limit of about 10^{14}. It was also shown that since SERS is induced on these substrates by the strong interaction of trapped surface plasmons within the micron-scale void architecture of the cavities a high degree of reproducibility of the detected signals is obtained unlike for so-called “hot spot” conditions for single molecule level detection.

FUTURE WORK:

The following are some topics for future work related to this thesis:

- Quantitative understanding of the broad inelastic scattering in defected organic solids by modeling and simulations

- Thermal measurements, such as differential thermal calorimetry to determine molar heat capacity and understanding the driving force for stabilization of the type II polymorph of APAP

- Fabrication of tablets by compaction of stabilized type II APAP and use of Raman spectroscopy and imaging techniques to evaluate long-term stability

- Further analysis of images obtained for films fabricated from API (e.g. griseofulvin) nanosuspensions would test for precision and accuracy of the predictions of component concentrations in thin films and extend it to excipient tablets with deposited API. It would also be of interest to develop in-line sensing, other than chemical imaging used till now, to characterize film quality during production and further optimization of already developed in-line monitoring of particle size of API in nanosuspensions by Raman spectroscopy to effectively predict the particle size during milling.

APPENDIX A

APAP SINGLE CRYSTAL STUDY

Using Raman spectroscopy, as discussed in this thesis, lattice and molecular vibrational data can be obtained. Although it is not typically done, it would be particularly useful if this data can be collected from individual crystals as a function of temperature, pressure and crystal orientation. During pharmaceutical processing of organic powders consisting of millions of crystallites, mechanical milling is often used to decrease the average particle size of weakly water-soluble particles in order to provide solubility. Thermal and pressure changes that occur during the milling process can induce structural transformations in the milled powders. A temperature and pressure study of a single crystal simulates these changes for an individual pharmaceutical crystallite in a powder to provide insights into the intra- and inter-atomic forces within the crystal structure. This is part of a larger study within the NSF-ERC which includes single crystal X-ray diffraction as a function of uniaxial stress at the University of Hawaii coupled with modeling at Rutgers University. In this work single crystals of acetaminophen (APAP) grown at the University of Hawaii (K. Morris *et al*) have been studied as a function of temperature up to near the melting point and crystal orientation using confocal Raman spectroscopy to better understand the effect of milling on structural stability and the possibility of inducing polymorph formation. In addition, Raman spectra recorded as a function of crystal orientation (determined by the Hawaii group) and structural data in the literature on the molecular architecture in the stable type I polymorph allowed more explicit assignments to modes of the molecular and lattice vibrations.

Figure A.1 (a), (b), and (c) shows confocal micro-Raman spectra at ambient conditions from the main three faces of a rod-like monoclinic single crystal with 4 molecules per unit cell and $P2_1/a$ space group symmetry [65] compared with the corresponding Raman spectrum of powders of type I APAP. Each face will correspond to a unique set of orientations of the APAP molecule in the type I polymorphic structure. Figure A.2 (a), (b), and (c) show spectra qualitatively attributed each to one of the main faces with Miller indices of (001), (020), and $(20\bar{1})$ determined by X-ray diffraction. The intensity of a Raman line depends on the interaction of the electric vector of the incoming radiation with the vibrational eigenvector. The most intense vibration would be one where the two vectors are in the same plane.

Figure A.1 (a) shows Raman spectra from single crystal APAP with the laser beam backscattered from the crystal face labelled face 1 and from APAP powder. The Raman spectrum of the powder represents the average Raman scattering from crystallites of various orientations. Strong Raman intensity values indicate that the inter- and intra-molecular vibrations in acetaminophen, particularly the arrowed lines associated with the stretching of the aromatic ring, aromatic C-H stretching and C=O vibrations show high intensity because they are in the plane of the electric vector of the incident exciting laser beam. This is consistent with the molecules being oriented in the (020) plane as shown in the insets to Figure A.1 (a). Figures A.1 (b) and (c) show the Raman spectra for faces 2 and 3 of the single crystal. The Raman intensity distribution for face 2 is substantially reduced relative to that of the powder spectrum. This face can be assigned to the $(20\bar{1})$ plane because the aromatic rings in this plane, as shown in the inset, are aligned approximately edge-on to the incident beam and therefore only the weaker deformation

vibrations interact with the electric vector of the incident beam. Face 3 can be assigned to the (001) plane because the Raman intensity distribution from this face is similar to that of the powder due to the fact that the APAP molecules have an intermediate alignment and the electric vector of the incident laser beam interacts with both stretching and deformation vibrations.

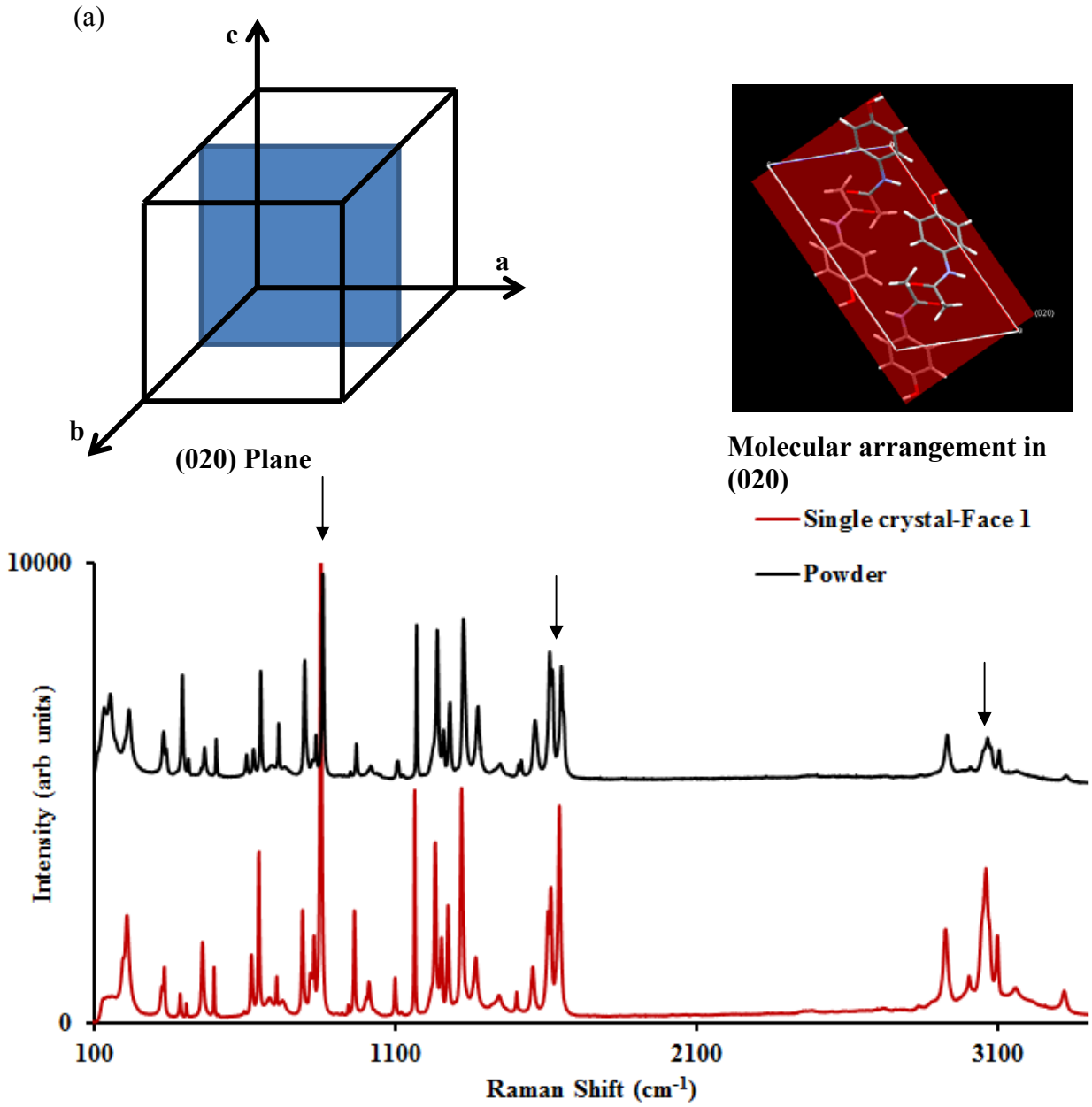

(b)

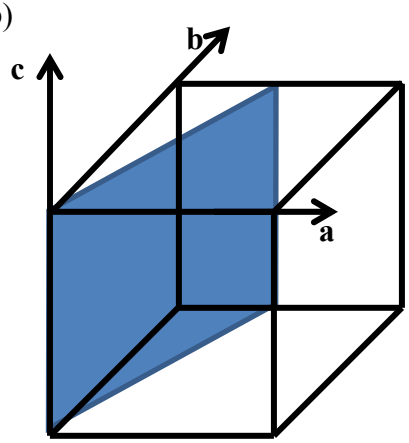

$(20\bar{1})$ **Plane**

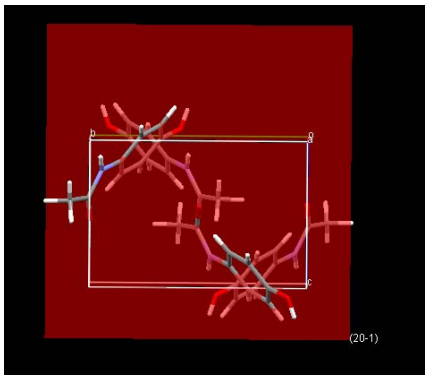

Molecular arrangement in $(20\bar{1})$

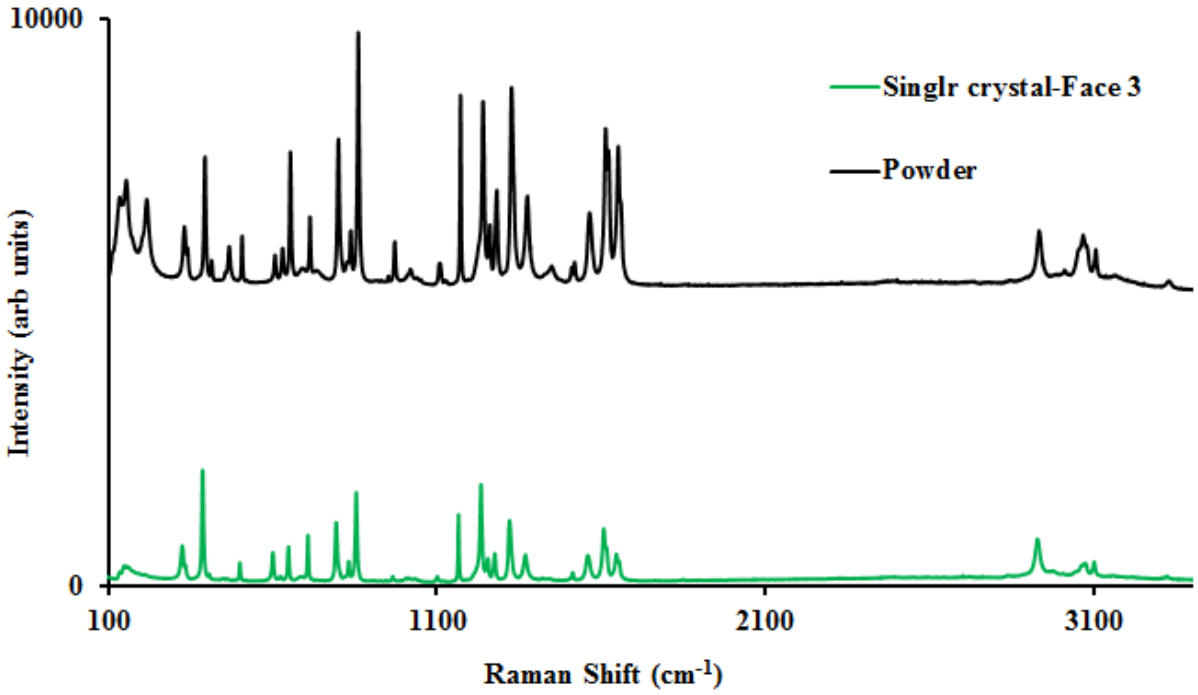

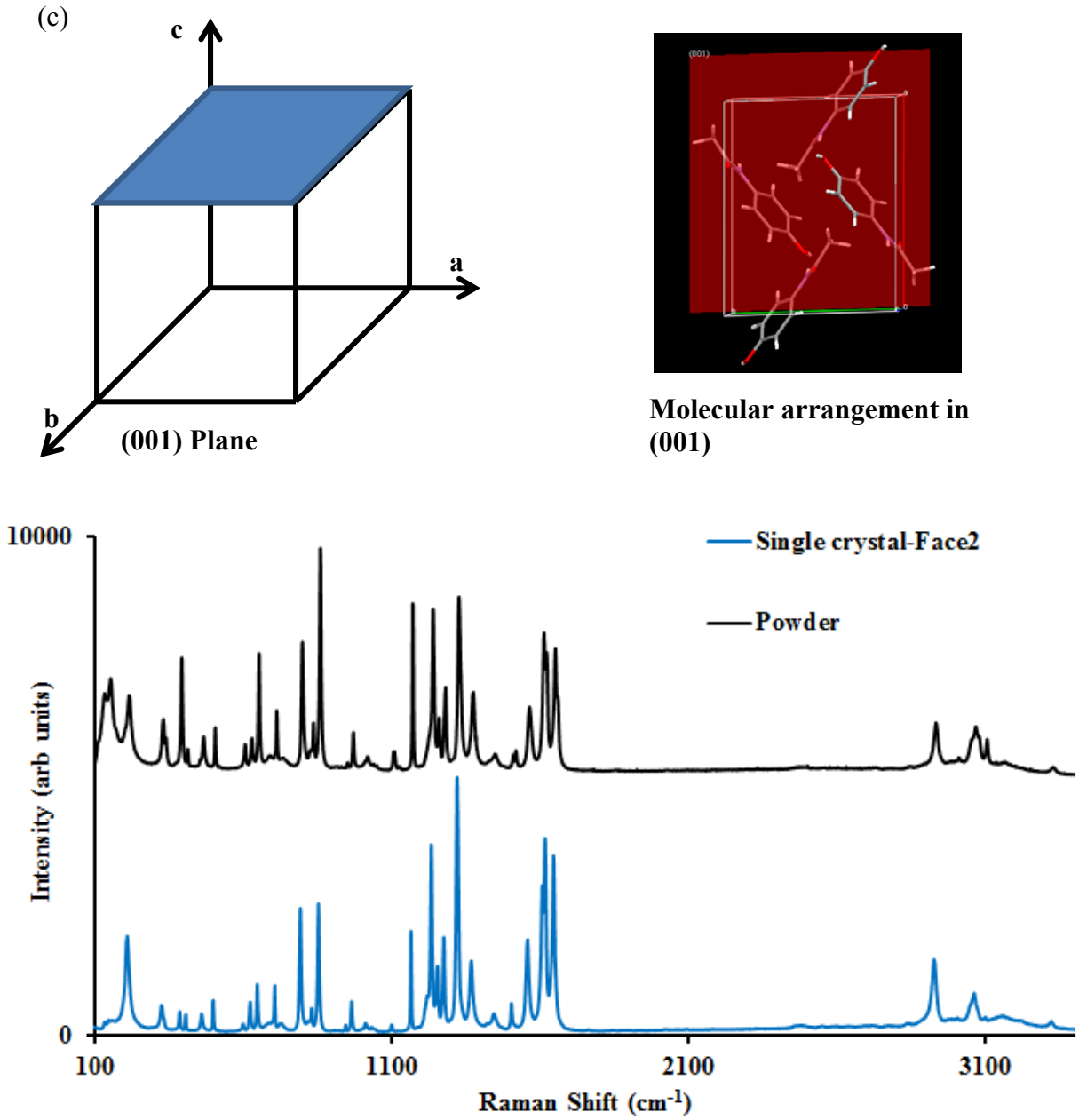

Figure A.1 Raman spectra of three faces of an APAP single crystal at room temperature: (a) Face 1, assigned to the (020) plane, shown in inset with corresponding arrangement of the APAP molecules, (b) Face 2 assigned to the $(20\bar{1})$ plane with corresponding plane of molecules in inset, and (c) Face 3 assigned to (001) with corresponding plane of molecules in inset. Plane of each face is represented by red sheet. The "ball and stick" convention of plane of atoms is used for acetaminophen molecule where grey, red, white, and blue labels represent carbon, oxygen, hydrogen, and nitrogen respectively.

Study of Single Crystal APAP as a Function of Temperature

The spectra were recorded with a confocal Raman system (for details see Chapter 2) as a function of temperature using Linkam TS1500 heating and cooling stage at each of following temperatures T = 25, 72, 101, 130, 154, and 175°C, Figure A.2 (a). The line frequencies, particularly those associated with translational modes at low frequency broaden and decrease in frequency with softening of the lattice as the temperature rises from 25°C to near melting at 175°C, as shown in Figure A.2 (b). Shift in frequency is also noticed for the C=O stretch at 1649 cm^{-1} which is associated with the intermolecular type B hydrogen bonding discussed in section 3.4 and shown in Figure A.2 (c). As the temperature rises, the line experiences some broadening with upshift in the peak position of 2 cm^{-1}, as shown in Figure A. 3 (a) and A. 4, respectively. Interestingly, even at temperature values close to melting, (T = 175°C), the linewidths remain relatively narrow indicating the presence of ordered intermolecular interactions. Slight change in the peak position is most likely due to small local reorientations of the molecules upon heating, resulting in the decrease of type B hydrogen bonding and increase in force constant for the C=O stretching mode. Larger shifts in the frequency value can indicate transition to the type III or amorphous phase as shown in Table 3.1. However, recorded changes in peak position and associated peak broadening at close to the melting temperature, show no significant amorphous behavior since the heating causes significantly smaller shift, less than 9 cm^{-1}, observed for the amorphous phase. Figure A.2 (c) and (d); and Figure A.3 (b) and (c), show changes in peak positions and line broadening due to onset of disorder, Figures A. 4, for lines at 3083 cm^{-1} and 3326 cm^{-1} associated with C-H and N-H stretching modes respectively, show the largest changes with temperature. As indicated in

Table 3.1, the C-H vibration of the phenyl ring increases in frequency in the type III polymorph of APAP and also in the amorphous phase. Upon heating, however, a downshift by 3 cm^{-1} is observed indicating changes in local inter-molecular potential. By contrast, at 175°C, the NH-stretching line at 3326 cm^{-1} upshifts by a surprisingly large value of 12 cm^{-1} and broadens significantly. The influence of type A hydrogen bonding on the N-H stretching vibration is therefore significant and shows large local changes in symmetry around this bond indicating a strong driving force for polymorph formation. It would therefore be interesting to study the spectra also as a function of stress in different directions in order to see if polymorph formation is induced.

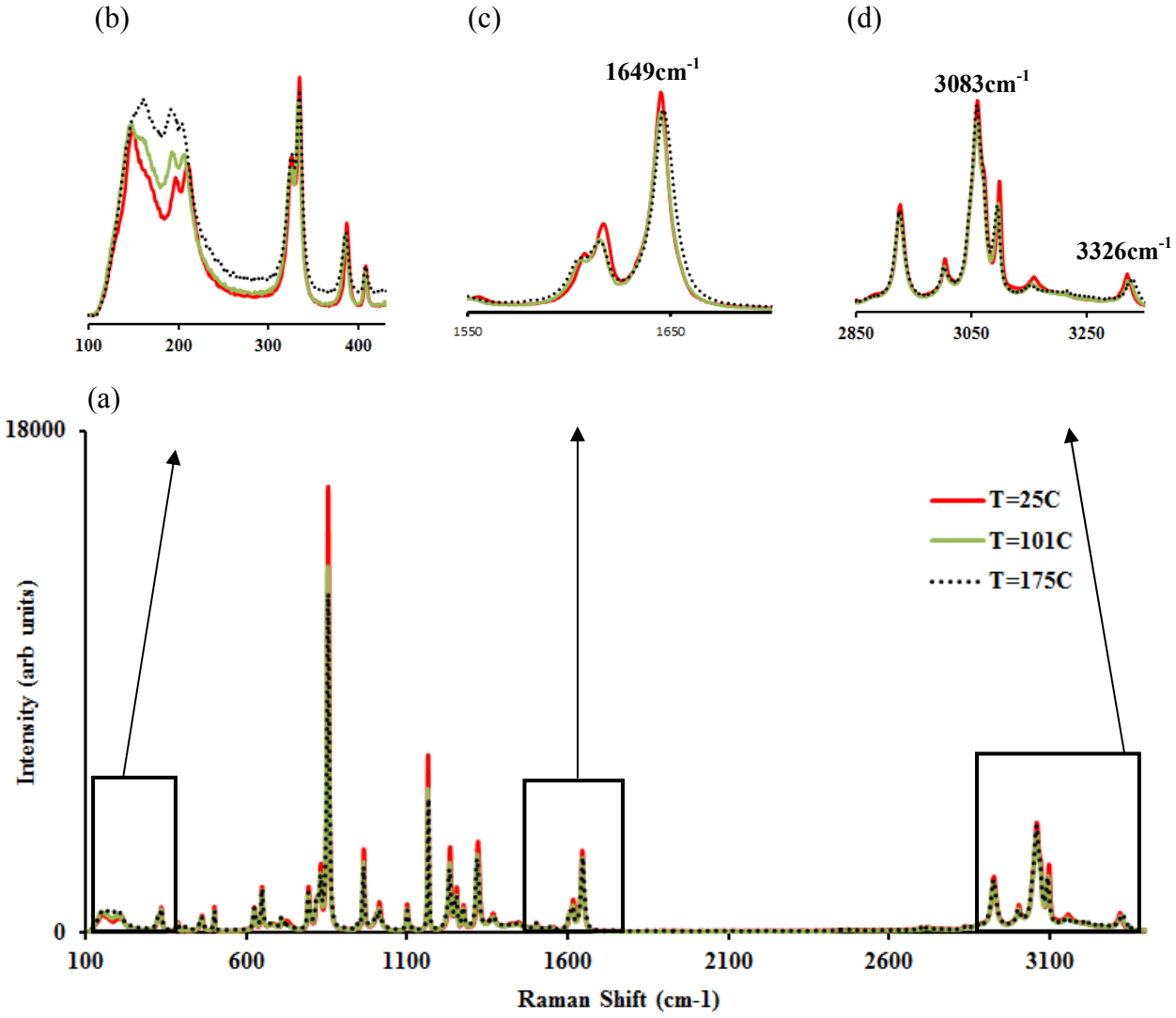

Figure A.2 (a) Raman spectra of APAP single crystal, face 1, taken as a function of temperature at 25°C, 101°C, and 175°C show expansion of boxed regions: (b) 100 to 450 cm^{-1}, (c) 1550 to 1750 cm^{-1}, (d) 2850 to 3300 cm^{-1}.

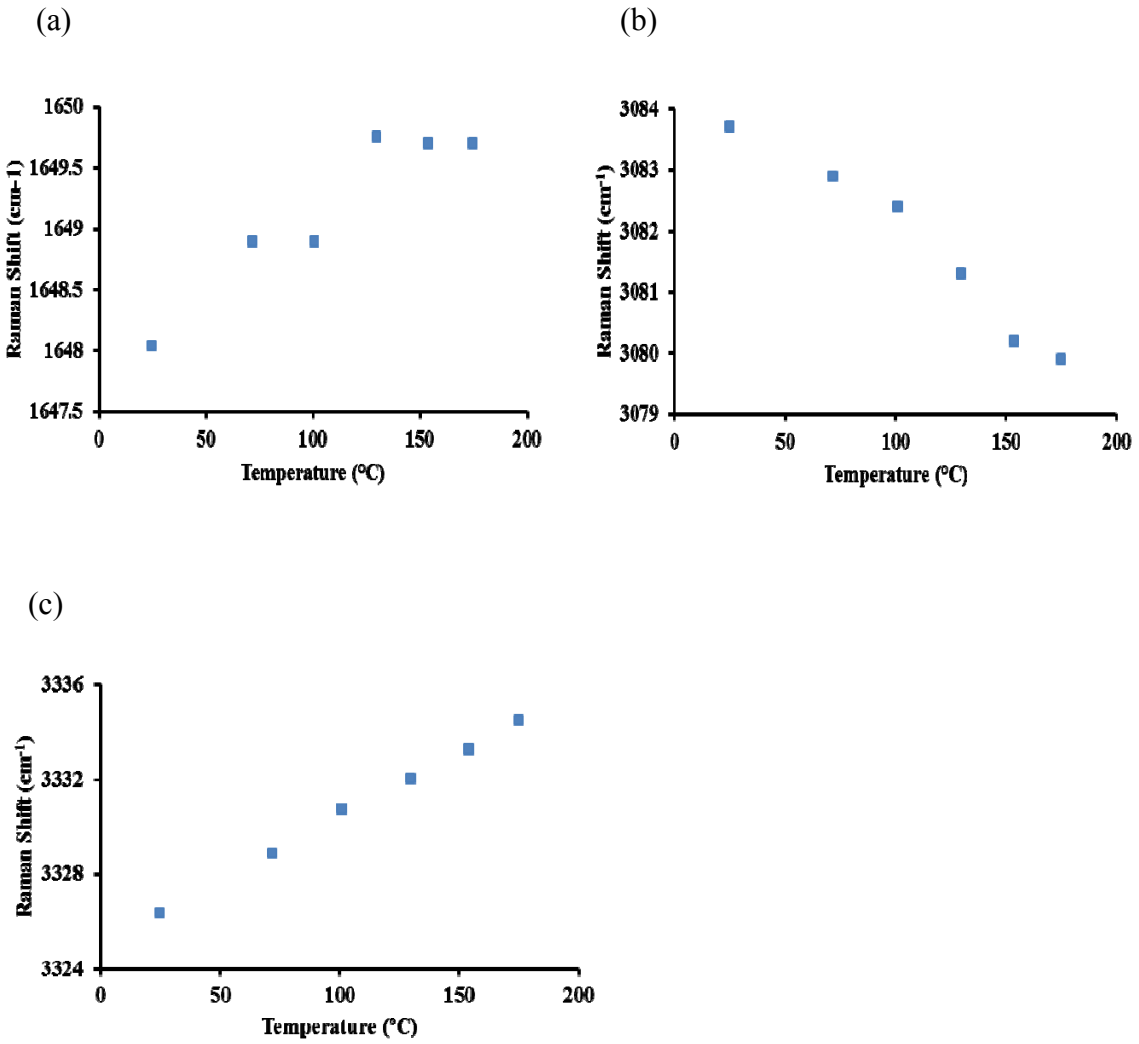

Figure A. 3 Evolution of peak frequencies in APAP single crystal with temperature for: (a) 1648 cm^{-1} C=O stretching line, (b) 3083 cm^{-1} aromatic C-H asymmetric stretching line, and (c) 3326 cm^{-1} N-H stretching line.

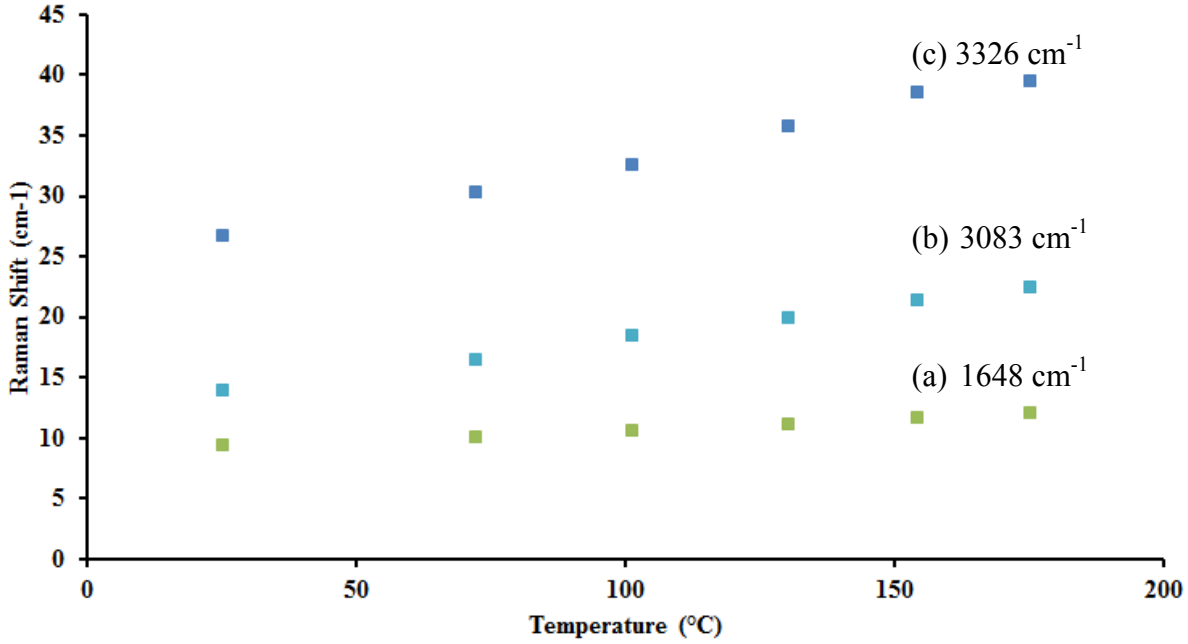

Figure A. 4 Evolution of peak broadening with temperature for: (a) 1648 cm^{-1} C=O stretching line, (b) 3083 cm^{-1} aromatic C-H asymmetric stretching line, and (c) 3326 cm^{-1} N-H stretching line.

REFERENCES

1. *Guidance for Industry, PAT - A Framework for Innovative Pharmaceutical Development, Manufacturing, and Quality Assurance*, F.D.A. U.S. Department of Health and Human Services, Editor. 2004.

2. Berntsson, O., *Characterization and application of near Infrared reflection spectroscopy for quantitative process analysis of powder mixtures*, in *Chemistry* 2001, Kungl Tekniska Högskolan, Royal Institute of Technology: Stockholm.

3. Wartewig, S. and R.H.H. Neubert, *Pharmaceutical applications of mid-IR and Raman spectroscopy.* Advanced Drug Delivery Reviews, 2005. **57**: p. 1144-1170.

4. Folestad, S. and J. Johansson, *Raman spectroscopy: A technique for the process analytical technology toolbox.* American Pharmaceutical Review, 2004. **7**: p. 82-87.

5. Raman, C.V. and K.S. Krishnan, *A new type of secondary radiation.* Nature, 1928. **121**: p. 501-502.

6. Ferraro, J.R., K. Namakoto, and C.W. Brown, *Introductory Raman Spectroscopy*. 2003: Elsevier.

7. Smekal, A., *The quantum theory of dispersion.* Naturwissenschaften, 1923. **11**: p. 873.

8. Sasic, S., *Raman mapping of low-content API pharmaceutical formulations. I. Mapping of alprazolam in alprazolam/xanax tablets.* Pharmaceutical Research, 2007. **24**: p. 58-65.

9. Conti, C., et al., *Micro-Raman depth profiling on polished cross-sections: the mapping of oxalates used in protective treatment of carbonatic substrate.* Journal of Raman Spectroscopy, 2008. **39**: p. 1307-1308.

10. Zuk, J., J. Romanek, and W. Skorupa, *Micro-Raman depth profile investigations of beveled Al+-ion implanted 6H-SiO samples.* Nuclear Instruments and Methods in Physics Research B, 2009. **267**: p. 1251-1254.

11. Brus, L., *Noble metal nanocrystals: plasmon electron transfer photochemistry and single-molecule Raman spectroscopy.* Accounts of Chemical Research, 2008. **41**: p. 1742-1749.

12. Kleinert, H., *Stresses and defects*, in *Gauge fields in condensed matter*. 1989, World Scientific: Singapore.

13. Wang, H.L., C.K. Mann, and T.J. Vickers, *Effect of powder properties on the intensity of Raman scattering by crystalline solids.* Applied Spectroscopy, 2002. **56**: p. 1538-1544.

14. Ramirez, J.M.H., P. Colomban, and A. Bunsell, *Micro-Raman study of the fatigue fracture and tensile behaviour of polyamide (PA 66) fibers.* Journal of Raman Spectroscopy, 2004. **35**: p. 1063-1072.

15. Gouadec, G. and P. Colomban, *Raman Spectroscopy of Nanomaterials: How Spectra Relate to Disorder, Particle Size and Mechanical Properties.* Progress in Crystal Growth and Characterization of Materials, 2007. **53**: p. 1-56.

16. Colomban, P., G. Sagon, and X. Faurel, *Differentiation of antique ceramics from the Raman spectra of their coloured glazes and paintings.* Journal of Raman Spectroscopy, 2001. **32**: p. 351-360.

17. Colomban, P., *Nano/microstructure and property control of single and multiphase materials*, in *Chemical processing of ceramics*, B.I. Lee and S. Komarneni, Editors. 2005, CRC Press: Boca Raton. p. 303-339.

18. Veprek, S., Z. Iqbal, and F.A. Sarott, *A thermodynamic criterion of the crystalline-to-amorphous transition in silicon.* Philosophical Magazine B, 1982. **45**: p. 137-145.

19. Grant, D.J.W., *Theory and origin of polymorphism*. Polymorphism in pharmaceutical solids, ed. H.G. Brittain. 1999, New York: Marcel Dekker Inc.

20. Parker, J.H., D.W. Feldman, and M. Ashkin, *Raman scattering by silicon and germanium.* Physical Review 1967. **155**: p. 712-714.

21. Valeur, B., *Molecular fluorescence: principles and applications*. 2002, New York: Wiley.

22. Myerson, A.S., *Handbook of industrial capacity*. 2002, Woburn: Butterworth-Heinemann.

23. Żarów, A., et al., *Spectroscopic and X-ray diffraction study of structural disorder in cryomilled and amorphous Griseofulvin* Applied Spectroscopy, 2011. **65**: p. 135-143.

24. Jerez, J.I., et al., *Complementary Near-Infrared and Raman chemical imaging of pharmaceutical gel strips films.* Journal of Pharmaceutical Sciences, under review.

25. Żarów, A., F.J. Owens, and Z. Iqbal, *Surface-enhanced Raman spectroscopic detection of energetic compounds on periodic arrays of gold-coated cavities.* Applied Spectroscopy, under review.

26. Chikhalia, V., et al., *The effect of crystal morphology and mill type on milling induced crystal disorder* European Journal of Pharmaceutical Sciences, 2006. **27**: p. 19-26.

27. Elamin, A.A., et al., *Increased metastable solubility of milled griseofulvin, depending on the formation of a disordered surface structure.* International Journal of Pharmaceutics, 1994. **111**: p. 159-170.

28. Maeda, T., S.I. S, and T. Kobayashi, *Epitaxial growth and defect structures of quaterrylene studied using high resolution electron microscopy.* Physica Status Solidi A, 2002. **2**: p. 489-498.

29. Wildfong, P.L.D., et al., *Towards an understanding of the structurally based potential for mechanically activated disordering of small molecular organic crystals.* Journal of Pharmaceutical Sciences, 2006. **95**: p. 2645-2656.

30. Bolton, B.A. and P.N. Prasad, *Laser Raman investigation of pharmaceutical solids: griseofulvin and its solvates.* Journal of Pharmaceutical Sciences, 1981. **70**: p. 789-793.

31. Bellows, J.C., F.P. Chen, and P.N. Prasad, *Determination of drug polymorphs by laser Raman spectroscopy. I. Ampicillin and griseofulvin.* Drug development and Industrial Pharmacy, 1977. **3**: p. 451-458.

32. Winefordner, J.D., *Raman spectroscopy for chemical analysis*. Instrumentation overview and spectrometer performance, ed. R.L. McCreery. 2000, New York: John Wiley & Sons, Inc.

33. Ito, M., *Raman spectra of cyclohexane crystal I and crystal II* Spectrochimica Acta, 1965. **21**: p. 2063-2076.

34. Feng, T., R. Pinal, and M.T. Carvajal, *Process induced disorder in crystalline materials: differentiating defective crystals from the amorphous form of griseofulvin.* Journal of Pharmaceutical Sciences, 2007. **97**: p. 3207-3221.

35. Feng, T., S. Bates, and T.M. Carvajal, *Toward understanding the evolution of griseofulvin crystal structure to a mesophase after cryogenic milling.* International Journal of Pharmaceutics, 2009. **367**: p. 16-19.

36. Chamarthy, S.P. and R. Pinal, *The nature of crystal disorder in milled pharmaceutical materials.* Colloids and Surfaces A, 2008. **331**: p. 68-75.

37. Bates, S., et al., *Assessment of defects and amorphous structure produced in raffinose pentahydrate upon dehydration.* Journal of Pharmaceutical Sciences, 2007. **96**: p. 1418-1432.

38. Yamamura, S., R. Takahire, and Y. Momose, *Crystallization kinetics of amorphous griseofulvin by pattern fitting procedure using X-ray diffraction data.* Pharmaceutical Research, 2007. **24**: p. 880-887.

39. Żarów, A., et al. *Raman spectroscopy of defected griseofulvin in powders and films.* in *Advances in material Design for regenerative medicine, drug delivery, and targeting/imaging.* 2009. Boston: Material Research Society Symposium Proceedings.

40. Gioannis, B.D., P. Jestin, and P. Subra, *Morphology and growth control of griseofulvin recrystallized by compressed carbon dioxide as antisolvent.* Journal of Crystal Growth, 2004. **262**: p. 519.

41. Docoslis, A., et al., *Characterization of the Distribution, Polymorphism, and Stability of Nimodipine in Its Solid Dispersions in Polyethylene Glycol by Micro-Raman Spectroscopy and Powder X-Ray Diffraction.* American Association of Pharmaceutical Scientists Journal 2007. **9**: p. E361.

42. Wang, S.L., S.Y. Lin, and Y.S. Wei, *Transformation of metastable forms of acetaminophen studied by thermal Fourier Transform infrared (FT-IR) microspectroscopy.* Chemical and Pharmaceutical Bulletin, 2002. **50**: p. 153-156.

43. Iqbal, Z., *Vibrational Spectroscopy of Phase Transitions* in *Basic Concepts and Recent Developments in the Study of Structural Phase Transitions*, Z. Iqbal and F.J. Owens, Editors. 1984, Academic Press: San Diego.

44. Colomban, P., A. Tournie, and L. Bellot-Gurlet, *Raman Identification of glassy silicates used in ceramic, glass and jewellry : a tentative differentiation guide.* Journal of Raman Spectroscopy, 2006. **37**: p. 841-852.

45. Kiefer, W., *Micro-Raman spectroscopy of particle in the Mie-size range: A short review.* Croatica Chemica Acta, 1988. **61**: p. 473-486.

46. Elliott, G.R. and Z. Iqbal, *The Raman spectrum and phase transition in sym-triazine.* Journal of Chemical Physics, 1975. **63**: p. 1914.

47. Socrates, G., *Infrared and Raman Characteristic Group Frequencies* 3rd ed. 2000, England: John Wiley & Sons, Ltd.

48. Iqbal, Z. and E. Weidekamm, *Pre-resonant Raman spectra and conformations of nystatin in powder, solution and phospholipid-cholesterol multilayers.* Biochimica et Biophysica Acta, 1978. **555**: p. 426-435.

49. Puttaraja, K.A.N., D. S. Sakegowda, W. L. Duax, *Crystal structure of griseofulvin.* Journal of Crystal Growth, 1982. **12**: p. 415-423.

50. Ahmed, H., G. Buckton, and D.A. Rawlins, *Crystallisation of partially amorphous griseofulvin: determination of kinetic parameters using isothermal heat conduction microcalorimetry.* International Journal of Pharmaceutics, 1998. **167**: p. 139-145.

51. Foti, G., et al., *Structure of crystallized layers by annealing of <100> and <111> self-implanted silicon samples.* Applied Physics, 1978. **15**: p. 365-369.

52. Zeng, Y.P., et al., *Raman spectroscopy investigation on excimer laser annealing and thickness determination of nanoscale amorphous silicon.* Nanotechnology, 2004. **15**: p. 658-662.

53. Peng, Y.C., et al., *Crystallization of amorphous Si films by pulsed laser annealing and their structural characteristics.* Semiconductor Science and Technology, 2004. **19**: p. 759-763.

54. Kubota, K., T. Kato, and C. Adachi, *Control of the molecular orientation of a 2,2'-bithiophene-9,9-dioctylfluorene copolymer by laser annealing and subsequent enhancement of the field effect transistor characteristics.* Applied Physics Letters, 2009. **95**: p. 073303.

55. Nakayama, K., et al., *Alignment control of organic thin films by recrystalization under laser heating.* Transactions of the Material Research Society of Japan, 2005. **30**: p. 127-130.

56. Mitrofanov, O., et al. *Defects in organic molecular crystals: spectroscopy and effects on electronic and optical properties*. in *45th Annual IEEE Reliability Physics Symposium Proceedings* 2007. Phoenix, AZ.

57. Mitrofanov, O., et al. *Defects in organic molecular crystals: spectroscopy and effects on electronic and optical properties.* in *IEEE 45th Annual Reliability Phys Symp*. 2007. Phoenix, AZ.

58. Miyazaki, T., et al., *Ability of polyvinylpyrrolidone and polyacrylic acid to inhibit the crystallization of amorphous acetaminphen.* Journal of Pharmaceutical Sciences, 2004. **93**: p. 2710-2717.

59. Capes, J.S. and R.E. Cameron, *Effect of polymer addition on the contact line crystallisation of paracetamol.* Crystal Engineering Communications, 2007. **9**: p. 84-90.

60. Sacchetti, M., *Thermodynamic analysis of DSC data for acetaminophen polymorphs.* Journal of Thermal Analysis and Calorimetry, 2001. **63**: p. 345-350.

61. Perlovich, G.L., T.V. Volkova, and A. Bauer-Brandl, *Polymorphism of paracetamol: relative stability of the monoclinic and orhtorhombic phase revisited by sublimation and solution calotimetry.* Journal of Thermal Analysis and Calorimetry, 2007. **89**: p. 767-774.

62. Beyer, T., G.M. Day, and S.L. Price, *The prediction, morphology, and mechanical properties of the polymorphs of paracetamol.* Journal of American Chemical Society, 2001. **123**: p. 5086-5094.

63. Haisa, M., S. Kashin, and H. Maeda, *The orthorhombic form of p-hydroxyacetanilide.* Acta Crystallographica Section B, 1974. **30**: p. 2510-2512.

64. Haisa, M., et al., *Topochemical studies. IX. The crystal and molecular structure of p-aminoacetophenone.* Acta Crystallographica Section B, 1976. **32**: p. 1326-1328.

65. Nichols, G. and C.S. Frampton, *Physicochemical Characterization of the Orthorhombic Polymorph of Paracetamol Crystallized from Solution.* Journal of Pharmaceutical Sciences, 1998. **87**(6): p. 684-693.

66. Żarów, A., et al., *Stabilization of polymorphs in processed and unprocessed acetaminophen.* Journal of Pharmaceutical Sciences, to be published.

67. Martino, P.D., et al., *A new pure paracetamol for direct compression: the orthorhombic form.* International Journal of Pharmaceutics, 1996. **128**: p. 1-8.

68. Beyer, T., G.M. Day, and S.L. Price, *The prediction, morphology, and mechanical properties of the polymorphs of paracetamol.* Journal of the American Chemical Society, 2001. **123**(21): p. 5086-5094.

69. Fachaux, J.-M., et al., *Pure Paracetamol for direct compression Part I. Development of sintered-like crystals of Paracetamol.* Powder Technology, 1995. **82**(2): p. 123-128.

70. Yang, J., et al., *Dry Particle Coating for Improving the Flowability of Cohesive Powders.* Powder Technology, 2005. **158**: p. 21-33.

71. Kumar, V. and D. Tewari, *Dissolution*, in *Remington: The science and practice of pharmacy*, D.B. Troy, Editor. 2005, Lippincott Williams & Wilkins: Philadelphia. p. 672.

72. Szelagiewicz, M., et al., *In situ characterization of polymorphic forms: the potential of Raman spectroscopy.* Journal of Thermal Analysis and Calorimetry, 1999. **57**: p. 23-43.

73. Kauffman, J.F., L.M. Batykefer, and D.D. Tuschel, *Raman detected differential scanning calorimetry of polymorphic transformations in acetaminophen.* Journal of Pharmaceutical and Biomedical Analysis, 2008. **48**: p. 1310-1315.

74. Pastaner, J.P., et al., *Characterization of Acetaminpohen: Molecular microanalysis with Raman microprobe spectroscopy.* Journal of Forensic Sciences, 1996. **41**: p. 1060-1063.

75. Welton, J.M. and G.J. McCarthy, *X-ray powder data for acetaminophen.* Powder Diffraction, 1988. **3**: p. 102-103.

76. Chan, H.-K. and D.J. Grant, *Influence of compaction on the intrinsic dissolution rate of modified acetaminophen and adipic acid crystals.* International Journal of Pharmaceutics, 1989. **57**: p. 117-124.

77. Gowen, A.A., et al., *Recent applications of Chemical Imaging to pharmaceutical process monitoring and quality control.* European Journal of Pharmaceutics and Biopharmaceutics, 2007. **69**: p. 10-22.

78. Mosharraf, M. and C. Nystrom, *The effect of particle size and shape on the surface specific dissolution rate of microsized practically insoluble drugs.* International Journal of Pharmaceutics, 1995. **122**: p. 35-47.

79. Yamamoto, K., et al., *Dissolution Rate and Bioavailability of Griseofulvin from a Ground Mixture with Microcrystalline Cellulose.* Journal of Pharmacokinetics and Biopharmaceutics, 1974. **2**: p. 487-43-93.

80. Patel, T., et al., *Studies in Formulation Development of Low Dose Content Drug Using Fluid Bed Granulation Technique.* Journal of Pharmaceutical Sciences and Research, 2010. **2**: p. 264-271.

81. Yalkowsky, S.H. and S. Bolton, *Particle size and content uniformity.* Pharmaceutical Research, 1990. **7**: p. 962-966.

82. Zhang, Y. and K. Johnson, *Effect of drug particle size on content uniformity of low-dose solid dosage forms.* International Journal of Pharmaceutics, 1997. **154**: p. 179-183.

83. Al-Zoubi, N., J.E. Koundourellis, and S. Malamatris, *FT-IR and Raman spectroscopic methods for identification and quantitation of orthorhombic amd monoclinic paracetamol in powder mixes.* Journal of Pharmaceutical and Biomedical Analysis, 2002. **29**: p. 459-467.

84. Kachrimanis, K., D.E. Braun, and U.J. Griesser, *Quantitative analysis of paracetamol polymorphs in powder mixtures by FT-Raman spectroscopy and PLS*

regression. Journal of Pharmaceutical and Biomedical Analysis, 2007. **43**: p. 407-412.

85. Pinzaru, S.C., et al., *Identification and characterization of pharmaceuticals using Raman and surface-enhanced Raman scattering.* Journal of Raman Spectroscopy, 2004. **35**: p. 338-346.

86. Romero-Torres, S., J. Huang, and P.E. Hernandez-Abad, *Practical consideration on PAT analyzer selection - Raman vs. NIR spectroscopy* American Pharmaceutical Review, 2009 (December): p. 12-19.

87. Robert, P., et al., *Identification of chemical constituents by multivariate near-infrared spectral imaging.* Analytical Chemistry, 1992. **64**: p. 664-667.

88. Dowrey, A.E., G.M. Story, and C. Marcott, *Industrial applications on Near-IR imaging*, in *Spectrochemical analysis using infrared multichannel detectors*, R. Bhargava and I. Levin, Editors. 2005, Blackwell Publishing Ames. p. 175-188.

89. Henson, M.J. and L. Zhang, *Drug characterization in low dosage pharmaceutical tablets using Raman microscopic mapping.* Applied Spectroscopy, 2006. **60**: p. 1247-1255.

90. Sasic, S. and D.A. Clark, *Defining a strategy for chemical imaging of industrial pharmaceutical samples on Raman line-mapping and global illumination instruments.* Applied Spectroscopy, 2006. **60**: p. 494-502.

91. Clark, D., et al., *Pharmaceutical Applications of Chemical Mapping and Imaging*, in *Applications of Vibrational Spectroscopy in Pharmaceutical Research and Development*, D.E. Pivonka, J. Chalmers, and P. Griffiths, Editors. 2007, John Wiley & Sons, Ltd.

92. Sasic, S., et al., *Raman line mapping as a fast method for analyzing pharmaceutical bead formulations.* The Analyst, 2005. **130**: p. 1530-1536.

93. Wold, S., K. Esbensen, and P. Geladi, *Principle component analysis.* Chemometrics and Intelligent Laboratory System, 1987. **2**: p. 37-52.

94. Geladi, P. and B.R. Kowalski, *Partial least square regresion: A tutorial.* Analytical Chinica Acta, 1986. **35**: p. 1-17.

95. Gendrin, C., Y. Roggo, and C. Collet, *Pharmaceutical applications of vibrational chemical imaging and chemometrics: A review.* Journal of Pharmaceutical and Biomedical Analysis, 2008. **48**: p. 533-553.

96. Griffiths, P.R., *Infrared and Raman instrumentation for mapping and imaging*, in *Infrared and Raman Spectroscopic Imaging*, R. Salzer and H.W. Siesler, Editors. 2007, Wiley-VCH: Weinheim. p. 5-35.

97. Garsuch, V. and J. Breitkreutz, *Novel analytical methods for the characterization of oral wafers.* European Journal of Pharmaceutical Sciences, 2009. **73**: p. 195-201.

98. Sasic, S., *An in-depth analysis of Raman and near-Infrared chemical images of common pharmaceutical tablets.* Applied Spectroscopy, 2007. **61**: p. 239-250.

99. Iqbal, Z., et al., *Raman scattering from small particle size polycrystalline silicon.* Solid State Communications, 1981. **37**: p. 993-996.

100. Veprek, S., F.A. Sarott, and Z. Iqbal, *Effect of grain boundaries on the Raman spectra, optical absorption, and elastic scattering in nanometer-sized crystalline silicon.* Physical Review B, 1987. **36**: p. 3344-3350.

101. Esenturk, E.N. and A.R.H. Walker, *Surface-enhanced Raman scattering spectroscopy via gold nanostars.* Journal of Raman Spectroscopy, 2008. **40**: p. 86-91.

102. Corrigan, D.K., et al., *Application of surface-enhanced Raman spectroscopy (SERS) for cleaning verification in pharmaceutical manufacture.* PDA Journal of Pharmaceutical Science and Technology, 2009. **63**: p. 568-574.

103. Cardini, C., V. Quercia, and A. Calò, *Systematic application of gas chromatography to the analysis of pharmaceutical preparations.* Journal of Chromatography A, 1968. **37**: p. 190-193.

104. Nikolin, B., et al., *High perfomance liquid chromatography in pharmaceutical analyses.* Bosnian Journal of Basic Medical Sciences, 2004. **4**: p. 5-9.

105. Xu, H., et al., *Spectroscopy of Single Hemoglobin Molecules by Surface Enhanced Raman Scattering.* Physical Review Letters, 1999. **83**: p. 4357-4360.

106. Maruyama, Y., M. Ishikawa, and M. Futamata, *Single molecule detection with SERS.* Analytical Sciences, 2001. **17**: p. i1181.

107. Fleischmann, M., P. Hendra, and A. McMillan, *Raman spectra of pyridine adsorbed at a silver electrode.* Chemical Physics Letters, 1974. **26**: p. 163-166.

108. Jeanmarie, D.L. and R.P.V. Duyne, *Surface Raman spectroelectrochemistry part I. Heterocyclic, aromatic, and aliphatic amines adsorbed on the anodized silver electrode.* Journal of Electroanalytical Chemistry, 1977. **84**: p. 1.

109. Albrecht, M. and J.A. Creighton, *Anomalously intense Raman spectra of pyridine at a silver electrode.* Journal of the American Chemical Society, 1977. **99**: p. 5215-5219.

110. Mahajan, S., et al., *Relating SERS intensity to specific plasmon modes on sphere segment void surfaces.* Journal of Physical Chemistry, 2009. **113**: p. 9284-9289.

111. Perney, N.M.B., et al., *Tuning localized plasmons in nanostructured substrates for surface-enhanced Raman scattering.* Optics Express, 2006. **14**: p. 847.

112. Kneipp, K., et al., *Single molecule detection using surface-enhanced Raman scattering (SERS).* Physical Review Letters, 1997. **78**: p. 1667.

113. Nie, S.M. and S.R. Emery, *Probing single molecules and single nanoparticles by surface-enhanced Raman scattering.* Science, 1997. **275**: p. 1102.

114. Kneipp, K., et al., *Approach to Single-Molecule Detection Using Surface-Enhanced Resonance Raman-Scattering (Serrs) - a Study Using Rhodamine 6g on Colloidal Silver.* Applied Spectroscopy, 1995. **49**: p. 780.

115. Rodger, C., et al., *Surface-enhanced resonance-Raman scattering: An informative probe of surfaces.* Journal of the Chemical Society-Dalton Transitions, 1996. **5**: p. 791-799.

116. Iqbal, Z., *Surface enhancement by sample and substrate preparation techniques in Raman and Infrared spectroscopy*. Sample preparation techniques in analytical chemistry, ed. S. Mitra. 2003, Hoboken: John Wiley & Sons, Inc.

117. Moskovits, M., *Surface-enhanced spectroscopy.* Reviews of Modern Physics, 1985. **57**: p. 783-826.

118. Fleischmann, M., P.J. Hendra, and A.J. McQuillan, *Raman spectra from electrode surfaces.* Journal of the Chemical Society-Chemical Communications, 1973. **3**: p. 80-81.

119. Maher, R.C., et al., *Stokes/anti-Stokes anomalies under surface enhanced Raman scattering conditions.* Journal of Chemical Physics, 2004. **120**: p. 11746.

120. Kneipp, K., et al., *Population Pumping of Excited Vibrational States by Spontaneous Surface-Enhanced Raman Scattering.* Physical Review Letters, 1996. **76**: p. 2444.

121. Michaels, M., J. Jiang, and L. Brus, *Ag nanocrystal junctions as the site for surface-enhanced Raman scattering of single Rhodamine 6G molecules.* Journal of Physical Chemistry B, 2000. **104**: p. 11965.

122. Baker, G.A. and D.S. Moore, *Progress in plasmonic engineering of surface-enhanced Raman-scattering substrates toward ultra-trace analysis.* Analytical and Bioanalytical Chemistry, 2005. **382**: p. 1751-1770.

123. Hulteen, J.C. and R.P.V. Duyne, *Nanosphere lithography: A materials general fabrication process for periodic particle array surfaces.* Journal of Vacuum Science & Technology A, 1995. **13**: p. 1553.

124. Jensen, T.R., G.C. Schatz, and R.P.V. Duyne, *Nanosphere Lithography: Surface plasmon resonance spectrum of a periodic array of silver nanoparticles by UV-vis extinction spectroscopy and electrodynamic modeling.* Journal of Physical Chemistry B, 1999. **103**: p. 2394.

125. Haynes, C.L. and R.P.V. Duyne. *Plasmon scanned surface-enhanced Raman scattering excitation profiles* in *Materials Research Society Symposium Proceedings* 2002.

126. Saikin, S.K., et al., *Separation of electromagnetic and chemical contributions to surface-enhanced Raman spectra on nanoengineered plasmonic substrates.* Journal of Physical Chemistry Letters, 2010. **1**(2740-2746).

127. Carron, K.T. and L.G. Hurley, *Axial and azimuthal angle determination with surface-enhanced Raman spectroscopy: Thiophenol on copper, silver, and gold metal surfaces.* Journal of Physical Chemistry, 1991. **95**: p. 9979-9984.

128. Xue, G., J. Dong, and J. Zhang, *Surface-enhanced Raman scattering study of polymer on metal. Molecular chain orientation of polybenzimidazole and poly(L-histidine) and its transition.* Macromolecules, 1991. **24**: p. 4195-4198.

129. Lindstorm, C.D. and X.Y. Zhu, *Photo-induced electron transfer at metal-molecule interfaces.* Chemical Review, 2006. **106**: p. 4281-4300.

130. Lewis, I.R., N.W.D. Jr, and P.R. Griffiths, *The interpretation of Raman spectra of nitro-containing explosive materials. Part II. The implementation of neural, fuzzy and statistical models for unsupervised patter recognition.* Applied Spectroscopy, 1997. **51**: p. 1854.

131. Prasad, R.L., et al., *Photoacoustic spactra and modes of vibration of TNT and RDX at CO_2 laser wavelenght.* Spectrochimica Acta Part A: Molecular and Biomolecular Spectroscopy, 2002. **58**: p. 3093.

132. Ciezak, J. and S.F. Trevino, *Inleastic neutron scattering spectrum of cyclotrimethylenetrinitamine: A comparison with solid-state electronic structure calculations.* Journal of Physical Chemistry A, 2006. **110**: p. 5149.

133. Iqbal, Z., S**.** Bulusu, and J.R. Autera, *Vibrational spectra of beta-cyclotetramethylene tetranitramine and some of its isotopic isomers.* Journal of Chemical Physics, 1974. **60**: p. 221.